Characterization of Residual Stresses in Modern Welded Girders

by

Daniel Unsworth

A thesis submitted in partial fulfillment of the requirements for the degree of

Master of Science

in

Structural Engineering

Department of Civil and Environmental Engineering
University of Alberta

ABSTRACT

Residual stresses can have a significant impact on the stability of structural members. In the case of I-section beam elements, such stresses can impact lateral–torsional buckling (LTB) capacity, particularly in the inelastic range. I-sections are typically fabricated by either rolling as a single shape or welding three plates together; residual stress distributions can differ considerably between the two section types. It is therefore possible for a built-up welded girder to have a lower LTB capacity than that of a rolled one of identical cross-section. Concerns have been raised that such a difference may render Canadian steel design standards unconservative for welded girders. Because of the lack of recent physical LTB tests on welded girders, finite element modelling has been done to attempt to assess the design standard. Assumed residual stress distributions were based on data from 1970 to 1980 that may not be representative of modern fabrication processes. A paucity of residual stress data for current welded girders, however, prevents assessment of these assumed distributions. In this study, residual stress measurements are carried out on a series of four reduced-scale welded steel test girders. Testing consists of destructive sectioning tests and non-destructive ultrasonic measurements. A predictive residual stress model for modern welded girders is proposed, and the feasibility of the ultrasonic method for residual stress measurements addressed.

ACKNOWLEDGEMENTS

This project would not have been possible without a number of people. First and foremost thanks are due my supervisors, Dr. Robert Driver and Dr. Leijun Li. Their support and guidance was crucial throughout this project; I consider it a privilege to have had the opportunity to work with both of them.

I am also very grateful for the many outstanding researchers and friends I have had the chance to get to know over the course of my time at the University of Alberta. Several individuals deserve special mention: Dimple Ji, the researcher for the related study, whose patience and thoughtfulness helped to make work on this collaborative project an enjoyable experience, and Abdullah Al-Jaaidi, who was the source of many interesting discussions and helped make our office space pleasant to work in. I would also like to acknowledge the members of the Steel Centre and Li research groups for the many helpful discussions.

Additionally, the Morrison Structures Lab technicians, Greg Miller and Cameron West, helped to solve many issues during lab testing and were essential in ensuring the success of the experimental program.

Lastly, I would like to express gratitude to my parents for their continued support and encouragement during this time; I would not be where I am today were it not for them.

This research is funded by the Natural Sciences and Engineering Research Council of Canada and the CISC Centre for Steel Structures Education and Research at the University of Alberta. Steel donation by SSAB and fabrication and design assistance of the test specimens by Supreme Group is gratefully acknowledged.

Contents

List of Tables

List of Figures

List of symbols

a	=	fillet weld nominal leg size
a_1	=	fillet weld flange leg
a_2	=	fillet weld web leg
A	=	cross-sectional area of sectioned strip
A_w	=	fillet weld cross-sectional area
B	=	empirical coefficient for flange HSG reduction factor
b	=	flange width
C_w	=	warping constant
D_t	=	largest transverse dimension of girder
E	=	Young's modulus
G	=	shear modulus
h	=	web height
I	=	welding current
I_y	=	weak-axis moment of inertia
J	=	St. Venant torsion constant
L_g	=	nominal gauge length
L_{gi}	=	measured initial gauge length
L_{gf}	=	measured final gauge length
L_u	=	unbraced length
L_{11}	=	acoustoelastic constant for longitudinal waves propagating in the longitudinal direction

$L_{specimen}$	=	minimum sectioning specimen length
$L_{testpiece}$	=	minimum sectioning test piece length
l, m, n	=	Murnaghan's third-order elastic constants
$(M_0)_{icr}$	=	inelastic lateral–torsional buckling capacity
m_T	=	time-of-flight–temperature curve slope
Q	=	weld heat input
q	=	Z score threshold for removing outliers in ultrasonic data
S	=	strip width
T_m	=	maximum temperature of a longitudinal fibre
T_{surf}	=	surface temperature of specimen during ultrasonic measurement
T_y	=	temperature required to cause yielding of a fully restrained longitudinal fibre
TOF	=	time-of-flight of ultrasonic pulse
TOF_{meas}	=	uncorrected measured time-of-flight of ultrasonic pulse
TOF_{OL}	=	mean TOF in region overlapped by ultrasonic probe on left side
TOF_{OR}	=	mean TOF in region overlapped by ultrasonic probe on right side
TOF_0	=	zero-stress time-of-flight of ultrasonic pulse
t	=	plate thickness
t_f	=	flange thickness
V	=	welding voltage
V_{ij}	=	velocity of wave propagation in the i direction with particle motion in the j direction
v	=	welding speed

W	=	width of area measured with ultrasonic probe
w	=	web thickness
X_L, X_R	=	overlap of ultrasonic probe into adjacent left and right strips
x_r	=	set of locations across plate corresponding to measured stresses σ_r
z	=	perpendicular distance from weld centre-line
α	=	coefficient of linear thermal expansion
δ	=	change in offset of sectioning strip due to cutting
δ_i	=	offset of sectioning strip prior to cutting
δ_f	=	offset of sectioning strip after cutting
ϵ	=	uniaxial strain magnitude
ϵ_{corr}	=	curvature corrected strain released by sectioning
$\epsilon_1, \epsilon_2, \epsilon_3$	=	principle triaxial strains
ϵ_{11}	=	longitudinal strain
ϵ_{22}	=	transverse strain
ϵ_{33}	=	through-thickness strain
ϵ_r	=	measured strain released by sectioning
η_f	=	parametric high-stress-gradient region width in the flanges
η_{fe}	=	width of the edge regions in the flanges
η_w	=	parametric high-stress-gradient region width on one edge of the web
η_{Tf}	=	width of the tensile region in the flanges
η_{Tw}	=	width of the tensile region in the web
θ_c	=	critical angle of refraction for longitudinal waves

λ	=	Lamé's first parameter
μ	=	Lamé's second parameter
ν	=	Poisson's ratio
ρ_0	=	initial material density
σ_{Pcf}	=	parametric compressive stress in the flanges
σ_{Pcw}	=	parametric compressive stress in the web
σ_r	=	set of measured residual stress values across a plate
σ_{rel}	=	stress released due to cutting
σ_{yf}	=	base metal yield stress for the flanges
σ_{ym}	=	area-weighted average section yield stress
σ_{yw}	=	base metal yield stress for the web

Chapter 1

Introduction

1.1 Background

Residual stresses are an inherent feature of structural steel members. These are stresses internal to a member that are generated through various mechanisms during the production and fabrication processes. Owing to the wide variety of fabrication methods for steel members, residual stress distributions can vary substantially among members—even among those geometrically similar to one another. Such a difference is known to exist between rolled and welded steel beams, particularly in the longitudinal residual stress distribution over the cross-section. Such stresses can significantly impact lateral–torsional buckling (LTB) behaviour, particularly in the inelastic region. Because of the complexities associated with inelastic buckling behaviour, many design standards take into account the effect of residual stresses through use of empirical equations based on experimental buckling test capacities. Certain standards differentiate between rolled and welded sections through the use of separate design equations, owing to the significantly different residual stress distributions typical of the two section types.

The Canadian steel design standard, CSA S16-14 (2014), does not distinguish between rolled and welded sections when calculating LTB capacity. Recent statistical studies of existing LTB test data have raised concerns that such an approach may result in unconservative designs for welded beams (MacPhedran and Grondin 2011). Data examined consisted primarily of tests carried out from 1970 to 1980 in Asia and Europe; it is not clear if such tests are representative of beams and girders used in North America today. Finite element modelling has been done to attempt to resolve this issue; however, the residual stress model distributions assumed were also based on residual stress data from 1970 to 1980. Residual stress distributions in welded girders are expected to have changed significantly since this time, due to improvements in fabrication procedures. It is currently not possible to confirm this hypothesis, however, due to a lack of residual stress data for welded beams and girders fabricated in North America today. Residual stress data from such specimens are therefore needed to assess the accuracy of the residual stress distribution models.

1.2 Objectives and Scope

Residual stress measurements are carried out on a series of modern welded I-sections fabricated in Edmonton, Alberta by Supreme Group. Measured distributions are then used to assess existing residual stress models and, if necessary, propose a new model that is representative of the findings.

Because welded I-sections typically see use in larger flexural members (such as bridge girders), the testing program focuses on larger cross-sections. Detailed, destructive residual stress measurements are carried out on a set of test girders. An additional set of measurements on the test girders is taken using a non-destructive ultrasonic measurement system, in order to facilitate future measurements on full-scale bridge girders (for which destructive testing is not possible). Stress measurements on larger

cross-sections help to ensure broad applicability of a proposed residual stress model to a wide range of geometries.

Investigations are limited to thermally-induced residual stresses in the longitudinal direction, as these account for the main differences in stress distribution between rolled and welded sections, and tend to have the largest impact on LTB capacity.

1.3 Thesis Structure

This report consists of six chapters. An overview of previous relevant studies from the literature is presented in Chapter 2. Formation mechanisms for residual stresses and existing predictive models for welded I-sections are summarized. Past work assessing the impact of residual stresses on LTB is also presented. Finally, existing methods for residual stress measurement are summarized and selected existing stress data from welded I-sections reviewed.

Experimental methods for the residual stress measurement program are detailed in Chapter 3. Procedures for carrying out destructive sectioning tests and non-destructive ultrasonic tests are described. Results from both programs are presented in Chapter 4, including a comparison of results from non-destructive testing with those from the destructive program.

Chapter 5 deals with assessment of existing residual stress models using data from the destructive testing program. A predictive model for residual stresses in modern welded girders is proposed. Conclusions from the study and recommendations for future research are given in Chapter 6.

Test girder dimensions and weld sequences are given in Appendix A. Appendix B shows comparisons of predictive residual stress models with measured distributions.

Additional test data from the ultrasonic measurement program is included in Appendix C.

Chapter 2

Literature Review

2.1 Formation of Thermal Residual Stresses

Longitudinal thermal residual stresses are present in both rolled and welded steel beams. In rolled steel beams, stresses are formed due to differential cooling rates over the beam cross-section. In the case of I-shapes, the more exposed flange edges and web centre cool more quickly than the flange-web junctions. As these more exposed areas cool and contract, while gaining strength and stiffness, the slower-cooling area around the flange-web junction (with greater mass per unit of surface area) is subjected to shortening. The yield stress of steel is reduced at high temperatures; the slower-cooling regions thus undergoes compressive plastic deformation. Once the entire section has cooled, further contraction of the plastically deformed regions is restrained by the more exposed areas (which have regained yield stress capacity). The flange-web junctions thus go into tension and the more exposed areas go into compression to maintain equilibrium (Ballio 1983).

While the same physical principles are present in welded shapes, the stress-formation mechanism is slightly different. The increase in temperature of the filler metal and nearby base metal causes thermal expansion of the material around the weld. Lengthening of longitudinal fibres in this region is, however, partially restrained by the adjacent, cooler, fibres. Temperatures experienced during welding are high enough that thermal strain of the heated region will exceed the yield strain of the material. As temperature increases beyond this point, longitudinal expansion continues to be partially restrained by the adjacent fibres and compressive plastic strains are generated as a result. Following welding, as the fibres around the weld cool and contract, full contraction is prevented by the adjacent fibres (which have not undergone plastic deformation). Tensile longitudinal residual stresses thus arise in the weld fibres and those immediately adjacent in the base metal, while the remainder of the specimen goes into compression to maintain equilibrium (Masubuchi 1980).

2.2 Residual Stress Models

A number of predictive models for longitudinal thermal residual stresses in welded I-shapes have been proposed in the literature. Several such models are selected for examination in this study, based on past use in stability finite element modelling and potential for broad applicability to a range of cross-section geometries.

2.2.1 Chernenko and Kennedy

As part of a finite element study on column stability, the Chernenko and Kennedy (1991) model was proposed based on data from residual stress measurements on welded sections at Lehigh University. Two models were proposed for different plate cutting methods: one for milled plates and one for flame-cut plates. Stress magnitudes

are all constant fractions of base material yield stress and region widths constant fractions of plate width. Both models were derived for a relatively small range of cross-sectional geometries; it is not clear if the models are accurate for a wider range of cross-sections. Exact values are not reported for the Chernenko and Kennedy distributions. Approximate values are therefore used based on schematic graphs and reported upper-bound stress values—the distribution for sections comprising flame-cut plates is shown in Figure 2.1.

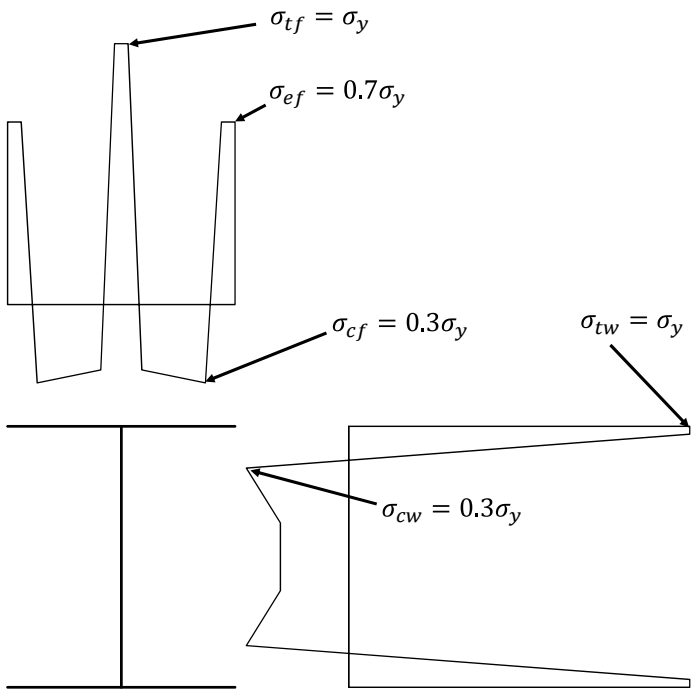

Figure 2.1: Chernenko and Kennedy (1991) residual stress model

2.2.2 Best-fit Prawel

The Best-fit Prawel model was proposed by Kim (2010) based on measured distributions from Prawel et al. (1974) and is shown Figure 2.2 ($F_y = \sigma_y$). Stress magnitudes

are all constant fractions of yield stress and zone widths constant fractions of plate width. The data upon which the model is based come from specimens comprising milled plates, hence the absence of a tensile region at the flange edges. For slender webs, it was found that the fixed value for compressive stress of $0.176\sigma_y$ exceeds the web buckling stress. In such cases, compressive stress is set at the web buckling stress and the web tensile stress scaled to preserve equilibrium of the web. As with the Chernenko and Kennedy models, the Best-fit Prawel model was derived based on a relatively limited range of cross-sectional geometries. The wider applicability of the model has not been examined.

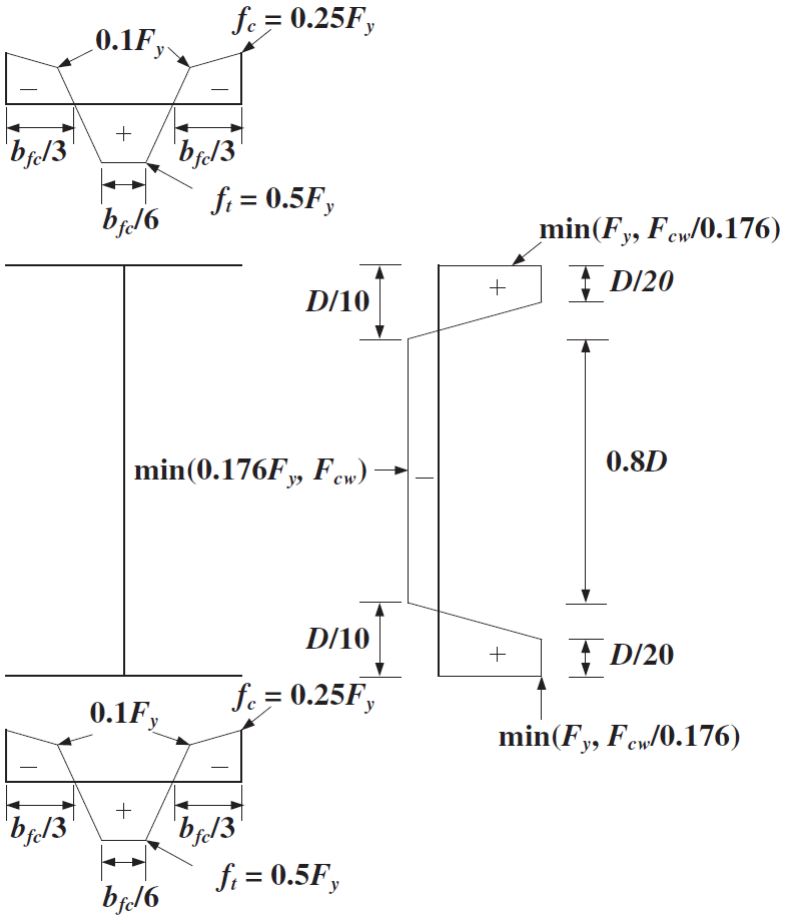

Figure 2.2: Best-fit Prawel residual stress model (Subramanian and White (2017))

2.2.3 BSK

The BSK model is included in the Swedish steel design standard (BSK 99 2003) and is shown in Figure 2.3. Tensile stress magnitudes around the weld region (σ_{ft} and σ_{wt}, respectively) are set at the base material yield stress and the width of the trapezoidal tension region calculated based on plate thickness (t_f and w for the flanges and web, respectively). Compressive stress for the flanges and web (σ_{fc} and σ_{wc}, respectively) are then calculated assuming each individual plate is in equilibrium.

Parameter	Value
σ_{ft}, σ_{wt}	σ_y
σ_{fc}, σ_{wc}	From equilibrium
a	$0.75t_f$
b	$1.5t_f$
c	$1.5w$
d	$1.5w$

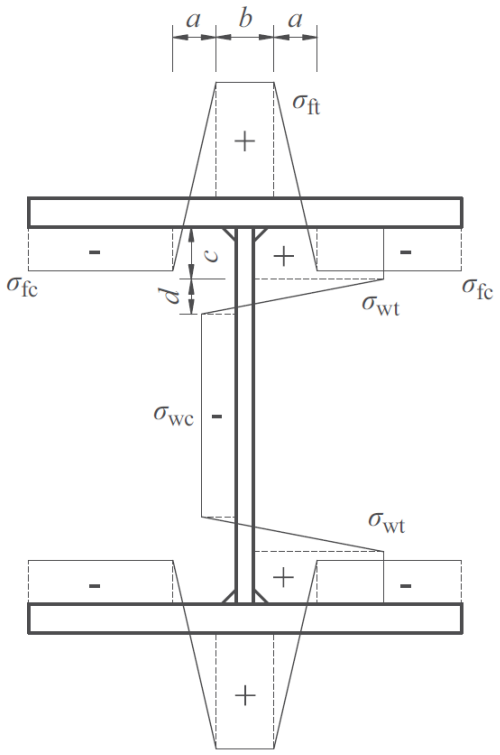

Figure 2.3: BSK residual stress model (modified from Yuan et al. (2014))

2.2.4 Dwight and Moxham

Dwight and Moxham (1969) proposed a model for welded sections based on a thermo-mechanical model of a weld bead on a metal plate. The maximum temperature increase experienced by a longitudinal fibre located at a distance z perpendicular to the weld centre-line, T_m (°C), was approximated by Equation 2.1.

$$T_m = \frac{128Q}{vzt} \tag{2.1}$$

where:

Q = weld heat input (J/mm)

v = welding speed (mm/s)

z = perpendicular distance from weld centre-line (mm)

t = plate thickness (mm)

Additionally, the temperature increase required to cause yielding of a fully-restrained fibre, T_y, was defined as:

$$T_y = \frac{\sigma_y}{E\alpha} \tag{2.2}$$

where:

σ_y = base metal yield stress

E = base metal Young's modulus

α = coefficient of linear thermal expansion

For a fully restrained fibre, if T_m exceeds T_y, plastic deformation will occur, having a magnitude of $\alpha T_m - \sigma_y/E$. When the fibre cools, full contraction is restrained,

resulting in tensile residual stresses of magnitude $E\alpha T_m - \sigma_y$, not exceeding the yield stress, σ_y. If T_m exceeds $2T_y$, residual stress will be equal to the tensile yield stress.

By setting T_m equal to T_y and $2T_y$, the locations of the fibres furthest from the weld for which T_m reaches T_y and $2T_y$, respectively, can be calculated (z_2 and z_1, respectively, in Figure 2.4). Stresses will transition linearly from σ_c to σ_y between these two points. In order to simplify the model, the average of these two distances (ηt) is calculated (Equation 2.3) and tensile stress set at σ_y inside this region.

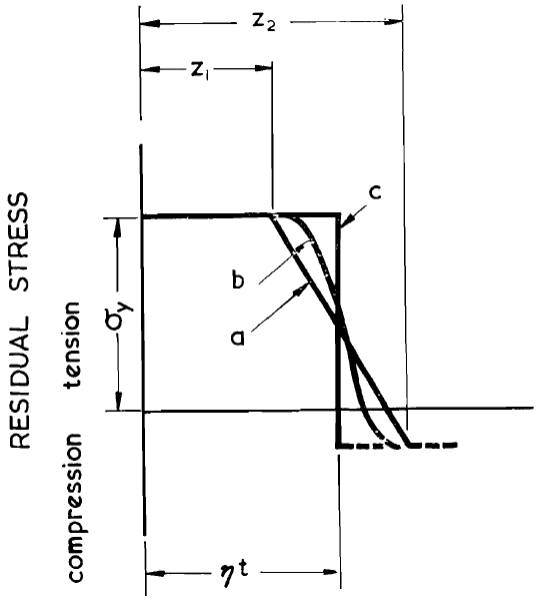

Figure 2.4: Residual stress distribution around the tension zone, (a) predicted by simplified theory, (b) measured (typ.), and (c) idealized (from Dwight and Moxham (1969))

$$\eta t = \frac{96VIE\alpha}{v\sigma_y t} \tag{2.3}$$

where:

V = welding voltage (V)

I = welding current (A)

v = welding speed (mm/s)

E = base metal Young's modulus (MPa)

α = coefficient of thermal expansion ($^{\circ}C^{-1}$)

σ_y = base metal yield stress (MPa)

t = plate thickness (mm)

Equation 2.3 is of limited use, however, in design situations, as welding parameters are not always known. Furthermore, actual heat input depends on process efficiency, which can vary significantly. It was found, however, that the amount of energy required to meld a unit volume of electrode is relatively constant over a range of welding voltages, currents, speeds and processes. Hence, it is possible to estimate heat input from weld size (for which data are much more readily available). Using electrode burn-off energy as 60 J/mm^3, Equation 2.4 was derived.

$$\eta t = \frac{CA_w}{\sigma_y t} \tag{2.4}$$

where A_w is the cross-sectional area of a single weld and C is defined as

$$C = \frac{96E\alpha}{16 \times 10^{-3}} \tag{2.5}$$

where E and α are expressed in units of MPa and $^{\circ}C^{-1}$, respectively.

Though originally proposed for a single plate, the model can be used for sections comprising multiple plates. In such cases, t is taken as the sum of the thicknesses of all plates joined at the weld ($(t_f + w)$ for a flange web join).

$$\eta t = \frac{CA_w}{\sigma_y \Sigma t} \tag{2.6}$$

Tensile stresses are assumed to be at the base metal yield stress over the entire width of the tensile region. Compressive stresses are then calculated using equilibrium for each individual plate. Figure 2.5 outlines the predicted distribution for an I-section.

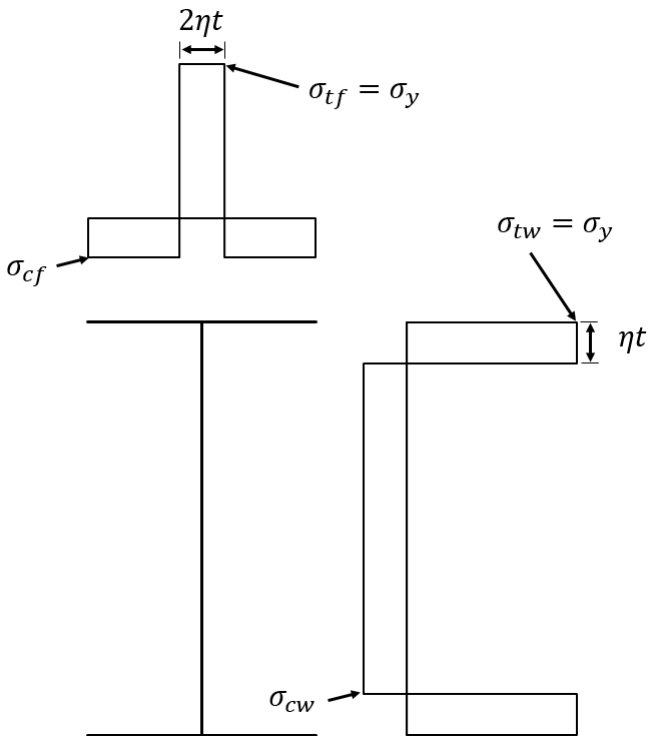

Figure 2.5: Dwight and Moxham (1969) residual stress model

2.3 Effect of Residual Stress on Lateral–torsional Buckling

It is widely believed that the difference in LTB capacity between rolled and welded sections is caused primarily by differences in the longitudinal residual stress distributions over the cross-section. Stress distributions in welded sections tend to result in a less favourable plastification sequence for beams loaded under strong-axis bending. Typically, larger portions of the flanges are subjected to compression in welded

sections, such that yielding of the compression flange occurs more rapidly than in a rolled section. If two girders of identical cross-section—one rolled, one welded—are subjected to strong-axis bending, the welded girder would typically be expected to have a lower inelastic LTB capacity, as partial yielding of the cross-section will result in a lower effective weak-axis moment of inertia than for the rolled section (provided that the onset of LTB occurs after initial yielding of the cross-section). Equation 2.7 represents the inelastic buckling capacity of a section based on first principles.

$$(M_0)_{icr} = \frac{\pi}{L_u}\sqrt{(EI_y)_e(GJ)_e + \left(\frac{\pi E}{L_u}\right)^2 (I_y C_w)_e} \tag{2.7}$$

where:

L_u = unbraced length

$(EI_y)_e$ = product of Young's modulus and effective weak-axis moment of inertia

$(GJ)_e$ = product of shear modulus and effective St. Venant torsion constant

$(I_y C_w)_e$ = product of effective weak-axis moment of inertia and effective warping constant

Yielding of the cross-section reduces $(EI_y)_e$, $(GJ)_e$ and $(I_y C_w)_e$, which results in a reduction in inelastic LTB capacity.

2.3.1 MacPhedran and Grondin (2011)

MacPhedran and Grondin examined a compilation of experimental LTB test data by Greiner and Kaim (2001) (from testing done in 1970-80) and compared capacities to those predicted by CSA-S16-09 (CSA 2009). The reliability index, defined as the mean value of the safety margin (i.e., capacity minus demand) divided by its standard deviation, was examined as a means of assessing the design standard. It was observed

that the standard results in a reliability index of 1.6 for welded sections, as opposed to 3.0 for rolled sections (MacPhedran and Grondin 2011).

2.3.2 Nethercot (1974)

Numerical tests by Nethercot in 1974 used both measured residual stress distributions and simplified residual stress models to compute buckling curves for a number of different sections. Stress data from rolled sections were used, both from British beam and column sections (Young 1971)(Rez-Gala 1962) and tests done at Lehigh University in the United States (Galambos 1963). It was found that tensile residual stresses around the flange-web junction cause a decrease in LTB capacity, even in the nominally elastic region, as the tensile residual stress magnitudes are equal to the base material yield stress and yielding thus occurs almost immediately in the tension flange-web junction. The capacity reduction, however, only amounted to a few percentage points. The presence of compressive stresses in the flanges were found to cause a much larger decrease in strength, though reductions only began to occur at onset of yielding of the compression flange (Nethercot 1974).

2.3.3 Fukumoto and Itoh (1981)

Measurements on a series of 34 welded beams of nominally identical cross-section were completed as part of a larger study on LTB (Fukumoto and Itoh 1981). The mean distribution (shown in Figure 2.6) was reported along with the standard deviation among the beams considered. A comparison was done with an earlier, similar testing program on rolled beams (Fukumoto et al. 1980): mean ultimate capacity was found to be lower in the welded beams compared to that of the rolled beams. It was also

observed that variation in both residual stresses and ultimate strength among beams was greater in the welded specimens.

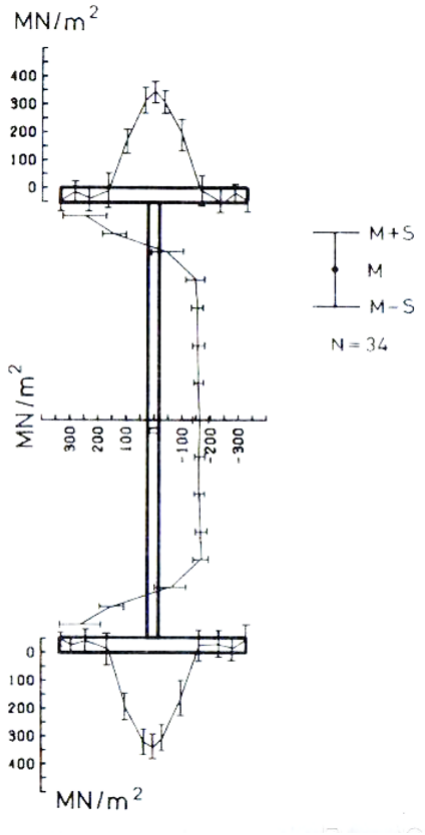

Figure 2.6: Mean residual stress distribution for welded sections measured by Fukumoto and Itoh (1981)

2.3.4 Kim (2010)

Kim (2010) modelled several I-shaped beams using three different residual stress models as part of a study on the stability of non-prismatic members.A residual stress model derived from measurements taken on welded sections by Prawel et al. (1974), called the Best-fit Prawel model was used alongside residual stress models proposed by Essa and Kennedy (2000) and Galambos and Ketter (1959) for rolled sections. Buckling capacities were compared to experimental capacities from several studies in

the literature. A comparison with tests conducted by Dux and Kitipornchai (1983) and Wong-Chung and Kitipornchai (1987) (which include measured residual stress distributions) was done: modelling done using the measured distributions was found to give capacities close to experimental capacities. Both the Galambos and Ketter and Best-fit Prawel models, however, resulted in capacities up to 20% below experimental. Furthermore, despite the fact that the Galambos and Ketter model is based on rolled shapes, while the Best-fit Prawel is derived from welded shapes, LTB capacities were similar between the two. This would indicate that it is difficult to broadly assess whether welded section residual stress distributions result in less favourable LTB performance in all cases.

2.3.5 Subramanian and White (2017)

Subramanian and White (2017) used the Galambos and Ketter and Best-fit Prawel models as part of a finite element study on LTB. Results were compared with experimental test results by Dux and Kitipornchai (1983), Wong-Chung and Kitipornchai (1987) and Richter (1998). It was found that the two stress distributions used tend to result in overly conservative results and that a more accurate prediction of LTB capacity can be achieved by using residual stress distributions of half the originally specified magnitude.

2.3.6 Kabir and Bhowmick (2018)

Kabir and Bhowmick (2018) used four residual stress distributions in a finite element study of LTB. Models proposed by Chernenko and Kennedy for both milled and flame-cut plates were used alongside measured distributions from a hot-rolled section (Dux and Kitipornchai 1983) and a welded section (Fukumoto and Itoh 1981). It

was observed that while the Chernenko and Kennedy model for flame-cut plates and Fukumoto distribution result in LTB capacities up to 35% and 29% lower, respectively, than those predicted by CSA-S16-14, capacities when using the Dux and Kitipornchai distribution from a hot-rolled section were up to 24% lower than those predicted by the standard.

2.4 Residual Stress Measurement

Numerous methods exist for measuring residual stresses in metals. An overview of the most widely-used methods is presented in this section.

2.4.1 Destructive methods

Destructive techniques for measuring residual stress rely on mechanical release of stress through the removal of material to create stress-free boundary conditions (Rossini et al. 2012). Though the specimen is destroyed in the process, a higher degree of accuracy is generally achievable when compared with non-destructive methods.

2.4.1.1 Sectioning

The specimen is cut into a series of longitudinal strips to release internal longitudinal stresses. Changes in the length of each fibre are recorded and used to calculate the stress released from cutting, which is assumed to be equal to the residual stress (Tebedge et al. 1973). The sectioning method has seen widespread use, particularly in I-sections, where bulk longitudinal stresses are of primary concern.

2.4.1.2 Contour

A flat cut is made through the entire specimen. By measuring the contours of the cut surfaces, a map of released strains and corresponding stresses over the cross-section (normal to the cut surface) can be generated (Prime and Gonzales 2000). While very high-resolution stress maps are achievable, a high degree of precision is required during cutting to ensure the cut surface is flat such that accurate results are obtained.

2.4.1.3 Hole-drilling (Semi-destructive)

A small hole is drilled in the specimen in order to release strains immediately around the hole, with strain changes measured by a strain gauge rosette mounted adjacent to the hole. A specialized drill is required in order to achieve sufficient precision in the drilling process. All three stress components on the surface of the material can be measured; stresses are typically only measured at the surface of the specimen. Variations of the method to create depth-profiles of stress are available (Rossini et al. 2012).

2.4.2 Non-destructive Methods

Non-destructive techniques make use of various material behavioural properties in order to deduce stresses without mechanically altering the material. Accuracy tends to be lower than that of destructive methods.

2.4.2.1 X-ray Diffraction (XRD)

When x-rays are incident on a crystalline material, the presence of parallel lattice planes causes diffraction patterns to develop (Rossini et al. 2012). By measuring

several diffraction peaks (angles at which maximum constructive interference occurs) the lattice spacing can be determined. This is compared to stress-free lattice spacing for a given material in order to determine internal strain. The sampled volume is very small: typical devices measure a 1 mm diameter spot to a depth of 5 – 50 μm (depending on the energy level of the incident x-rays)(Fitzpatrick et al. 2006). Use of neutron diffraction (a method that relies on the same principle as XRD) can result in much higher penetration depths (up to 25 mm in steel), however such tests must be carried out in a specialized facility where sufficient radiation protection is in place.

2.4.2.2 Ultrasonic (UT)

Equations derived by Hughes and Kelly (1953) predict a linear relationship between elastic wave velocity and strain in an elastic solid. By performing time-of-flight (TOF) measurements on a specimen, the average stress over the wave path can be calculated. Prior calibration on a stress-free specimen of the desired material is required, as significant variation in velocity–stress curves can exist between otherwise similar materials (Crecraft 1967).

2.4.2.3 Magnetic Methods

When an external magnetic field is applied to a ferromagnetic material, magnetization will increase by small jumps due to domain wall movements within the specimen. These magnetization changes can be detected by placing an induction coil near the specimen—each change in magnetization will induce an electric pulse in the coil. The resulting electrical signal from all detected pulses will vary in amplitude with stress; a higher amplitude indicates tension. Because microstructure also has an effect on the signal, calibration must be done for each type of material tested. Calibration on

a stress-free specimen is required to determine absolute stress magnitudes (Rossini et al. 2012).

2.5 Measured Residual Stresses in Welded I-shapes

Though numerous studies have been done to measure residual stresses in welded I-shapes, the majority of these were done at Lehigh University from 1948 - 1973 and are not necessarily representative of modern girders. Several modern studies of residual stresses in welded I-shapes are presented. It should be noted, however, that specimens were produced outside of North America and are not necessarily representative of modern, North-American specimens.

2.5.1 Ban et al. (2013)

Ban et al. (2013) took measurements on a series of eight welded I-sections made from high-strength steel ($\sigma_y = 460$ MPa). Section depths ranged from 110 to 360 mm, with flange widths of 130 to 348 mm and plate thicknesses of 10 to 14 mm. Fillet welds were used for all but one specimen (for which a type of full-penetration weld was used). It was found that compressive residual stress magnitude is primarily related to geometry, while no influencing factors were found for tensile stress. No interaction between the flanges and web was observed: each individual plate was found to be in equilibrium.

2.5.2 Yang et al. (2016)

Measurements on eight high-strength welded steel I-sections (Grade Q460GJ) were made by Yang et al. (2016): five doubly symmetric and three singly symmetric. Section depths ranged from 270 to 450 mm, with flange widths of 180 to 250 mm and plate thicknesses of 8 to 16 mm. The Chernenko and Kennedy model, among others, was examined and found to over-predict stresses in the flanges (measured stresses around the weld were $0.5\sigma_y$ on average), but give reasonable values for the web. Despite the use of flame-cut plates in all specimens, stresses were still compressive at the flange edges. Interaction between the flanges and web was observed. A stress model was proposed; however, the model is empirical so it is not clear whether it remains valid for sections outside the tested range.

2.5.3 Yang et al. (2018)

Yang et al. (2018) conducted a study on residual stresses in welded, thick-walled Grade Q460GJ I-sections. Sections ranged in height from 170 to 314 mm and had flanges widths from 162 to 312 mm. Plates were all flame-cut and 12 to 42 mm thick. The testing program comprised four sections with fillet welds and four with full-penetration welds. A significant through-thickness stress gradient was observed in the flanges around the weld region, with flange edges found to be consistently in tension. Compressive stress magnitudes were generally found to be lower for larger sections. Interaction between the flanges and web was observed. A stress model was proposed; however, the model is empirical and not necessarily valid for sections outside the parameter ranges of those tested.

2.6 Summary

A number of residual stress models exist for welded steel I-shapes, however, many are based on old data and may not be representative of modern welded steel girders. Finite element studies of LTB using several of these models report differences in LTB capacities of up to 20% depending on the residual stress model used, highlighting the sensitivity of LTB to residual stresses. An accurate model for modern welded girders is necessary in order to ensure accurate modelling of buckling behaviour. Modern data from welded sections does exist, however the specimens studies were produced outside of North America; it is not clear if such specimens are representative of girders fabricated in North America.

Numerous destructive and non-destructive methods exist for the measurement of residual stresses in metals—the most common are outlined. Selection of methods for this project is presented in Section 3.2.

Chapter 3

Methods

The testing program comprises a series of reduced-scale steel girders upon which longitudinal residual stress measurements are made. Destructive and non-destructive tests are carried out on the girders.

3.1 Specimen Information

Testing is done on a set of welded steel girders, each three metres long ('A' series). Each girder tested has a corresponding test girder of identical cross-section, but with a length of ten metres ('B' series). Girders in the 'B' series are subjected to large-scale buckling tests as part of a separate testing program (Ji 2019), while those in the 'A' series are used for residual stress measurement (i.e., specimens are not buckled). The 'A' series is the focus of this study. The complete testing program comprises eleven girders; four are tested in this study.

Girders are identified by both a number (e.g. SP2-1) and a full specimen ID (e.g. G6-430-32-1-p). Girder specimen ID is notated as:

G(X)-(b)-(t_f)-(CLASS)-(CUT METHOD)

where:
G(X) indicates a section depth, d, of X00 mm
(b) indicates flange width in mm
(t_f) indicates flange thickness in mm
(CLASS) indicates section class (1 or 2)
(CUT METHOD) indicates the cutting method used for the section (p (plasma) or f (flame))

The simple numbered convention is used in this study. A full list of girders with corresponding specimen IDs is given in Appendix A.

Girders are fabricated in Edmonton, Alberta in the fabrication shop of Supreme Group. Grade 350W steel plates are used for all girders; measured yield stress and Young's modulus values for each plate thickness are shown in Table 3.1.

Table 3.1: Measured steel plate yield stress values

Plate thickness (mm)	σ_y (MPa)	E (GPa)
12.7	364.2	203.7
25.4	355.1	202.4
31.8	346.7	201.3

Cross-section dimensions are shown in Table 3.2. Flange and web plates are either flame- or plasma-cut: the cutting method used for each girder is shown in Table 3.3. Plates are joined using submerged-arc welding using Lincolnweld LA-75 electrodes

with Lincolnweld 960 flux; single-pass fillet welds are deposited on both sides of the web. The interior faces of the flanges and both sides of the web are sandblasted prior to welding. Welding parameters are shown in Table 3.3, with more detailed information on welding sequence presented in Appendix A. No straightening is done on the specimens.

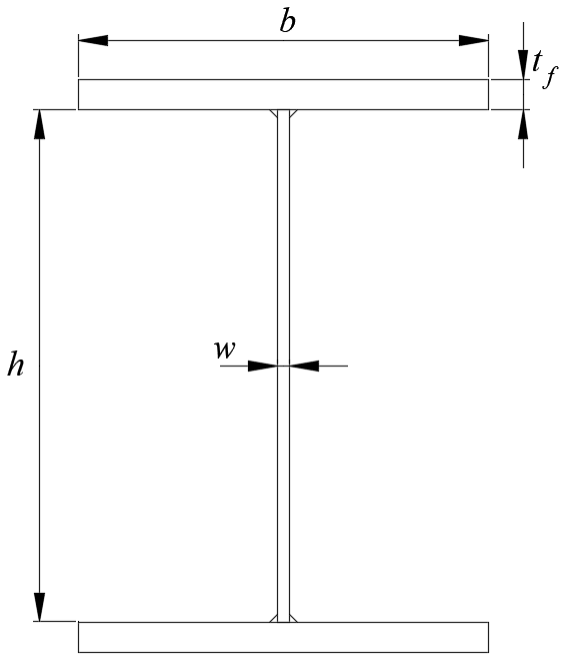

Figure 3.1: Girder cross-section dimensions

Table 3.2: Measured (nominal) girder cross-section dimensions (as defined in Figure 3.1)

Specimen ID	b (mm)	t_f (mm)	h (mm)	w (mm)
SP2-1	423 (430)	32.0 (31.8)	536 (536)	12.9 (12.7)
SP2-2	422 (430)	32.0 (31.8)	530 (536)	13.0 (12.7)
SP3	292 (300)	32.1 (31.8)	536 (536)	12.9 (12.7)
SP4	430 (430)	25.1 (25.4)	750 (749)	12.9 (12.7)

Table 3.3: Girder plate cutting methods and welding parameters

Specimen ID	Cutting method	a (mm)	V (V)	I (A)	v (mm/s)
SP2-1	Plasma	8	36	500	5.9
SP2-2	Oxy-flame	8	36	500	5.9
SP3	Plasma	8	36	500	5.9
SP4	Plasma	8	36	500	5.9

While nominal fillet weld leg sizes are all 8 mm, measured sizes are slightly larger. The length of both legs on all four welds are measured for each girder: measurements are taken on the transverse cut face following sectioning. Weld area is then calculated using:

$$A_w = \frac{1}{2} a_1 a_2 \tag{3.1}$$

where a_1 and a_2 are the length of the the legs on the flange and web, respectively. Average areas of all four welds for each girder are reported in Table 3.4.

Table 3.4: Measured weld areas for tested specimens

Specimen	Measured weld area (mm^2)
SP2-1	42.0
SP2-2	39.4
SP3	39.1
SP4	38.0

3.2 Selection of Methods

Among the destructive techniques presented in Section 2.4, the sectioning method is selected for several reasons. The method measures bulk stress, which is preferred over more localized tests (such as hole-drilling), as bulk stresses have greater impact on lateral–torsional buckling capacity. While use of the contour method produces much higher resolution stress maps compared to sectioning, the specimens in this study are too large to perform cuts of the required precision.

It is desired in the future to take measurements on a series of bridge girders during fabrication; a non-destructive method is therefore also required. Ultrasonic testing (UT) is deemed most appropriate due to it's relatively low cost, higher depth penetration compared to x-ray diffraction and magnetic methods (i.e., less sensitive to surface stresses from sandblasting) and ability to take bulk stress readings, thus reducing the chance of erroneous values due to local stress concentrations. Bulk stress measurement also allows for a direct comparison with sectioning results to be made—measured stresses from the sectioning method are used as a baseline with which the accuracy of the ultrasonic method can be assessed.

Past work using the sectioning and ultrasonic methods as it relates to this project is described in the following sections.

3.2.1 Sectioning

The sectioning method was first proposed by Kalakoutsky (1889); however, contemporary use of the method did not begin until 1948 at Lehigh University (Luxion and Johnston 1948). Extensive work was done with the method through 1948-73 with Tebedge et al. (1973) publishing a summary of the method. A technical memorandum was subsequently published by the Structural Stability Research Council that details the recommended procedure for use of the method (Pekoz et al. 1981).

3.2.2 Ultrasonic

Hughes and Kelly (1953) Sound waves were first used to measure stresses in elastic solids by Hughes and Kelly (1953). Equations relating wave velocity to internal strain were developed using a finite-deformation theory of elasticity (Murnaghan 1937) and third-order elastic strain energy terms. A homogeneous triaxial strain field is assumed. There are thus nine equations in total: three for each propagation direction, corresponding to the three different particle motions. Equations for waves propagating in the 1-direction are shown in Equations 3.2 to 3.4.

$$\rho_0 V_{11}^2 = \lambda + 2\mu + (2l + \lambda)\theta_T + (4m + 4\lambda + 10\mu)\epsilon_1 \tag{3.2}$$

$$\rho_0 V_{12}^2 = \mu + (\lambda + m)\theta_T + 4\mu\epsilon_1 + 2\mu\epsilon_2 - \frac{1}{2}n\epsilon_3 \tag{3.3}$$

$$\rho_0 V_{13}^2 = \mu + (\lambda + m)\theta_T + 4\mu\epsilon_1 + 2\mu\epsilon_3 - \frac{1}{2}n\epsilon_2 \tag{3.4}$$

where:

ρ_0 = initial material density

V_{ij} = velocity of wave propagating in the i direction with particle motion in the j direction

λ, μ = Lamé elastic constants

l, m, n = Murnaghan's third-order elastic constants

ϵ_1, ϵ_2, ϵ_3 = principle triaxial strains

$\theta_T = \epsilon_1 + \epsilon_2 + \epsilon_3$

In order to calculate stresses in a triaxial state, three of the nine wave velocities must be measured. If a state of uniaxial stress is assumed (that is when $\epsilon_1 = \epsilon$, $\epsilon_2 = \epsilon_3 = -\nu\epsilon$), the number of unknowns in the system is reduced from three to one, allowing calculation of strain from a single velocity measurement. The equation derived for longitudinal wave propagation parallel to the direction of strain is:

$$\rho_0 V_{11}^2 = \lambda + 2\mu + (4(\lambda + 2\mu) + 2(\mu + 2m) + \nu\mu(1 + 2l/\lambda))\epsilon \tag{3.5}$$

Crecraft (1967) Crecraft further investigated the technique when applied specifically to steel, aluminium and copper. Measurements were taken on a plastically deformed nickel–steel ring to assess the method's accuracy. Preferred grain orientation was found to have a significant effect on measurements; a reliable method of separating the effects of grain orientation and stress could not be found (Crecraft 1967).

Egle and Bray (1976) Egle and Bray examined the sensitivity of longitudinal and shear waves of various polarization and propagation directions in rail steel and discovered that longitudinal waves propagating parallel to the stress direction exhibit

the highest strain sensitivity and are thus most suitable for stress measurement (Egle and Bray 1976). In order to generate and receive such waves in the longitudinal direction of the specimen, transducers were connected to the specimen through Plexiglas wedges angled such that the diffracted waves are parallel to the specimen surface (approximately 28°). Such waves are referred to as longitudinal critically–refracted waves (L_{CR} waves).

Belahcene and Lu (2002) Work to quantify L_{CR} wave penetration depth was conducted by Belahcene and Lu (2002). Penetration depth was found to be equal to wavelength: depths varied from 1.0 to 2.5 mm for transducer frequencies varying from 2.25 to 6.60 MHz.

Fraga et al. (2009) An investigation by Fraga et al. (2009) examined the sensitivity of ultrasonic stress measurement to temperature. Readings were taken on an sample of API Grade 5L X70 steel for a range of temperatures between 20°C and 32°C for transducer frequencies of 2.25, 3.5 and 5.0 MHz. A linear relationship between temperature and time-of-flight (TOF) with a slope of up to 64 MPa/°C was observed. This was thought to be due to a combination of changes in the stress-free velocity of the sample with temperature and changes in length of the acrylic wedges to which the transducers were attached. Because only sample surface temperature was measured, not that of the acrylic, it was not possible to confirm which factor has a larger influence.

Javadi et al. (2012) A comparison of the L_{CR} method with hole-drilling and finite element results by Javadi et al. (2012) found ultrasonic measurements on a welded plate to be inaccurate in the heat-affected-zone (HAZ). When compared to finite element and hole drilling methods the L_{CR} method tends to over predict stresses

in the HAZ. A separate calibration test for material of similar microstructure to the HAZ was recommended (Javadi et al. 2012).

Javadi et al. (2017) A direct comparison of L_{CR} to shear wave stress measurement by Javadi et al. (2017) confirmed the greater stress sensitivity of the L_{CR} method. Tests on a post-weld heat-treated sample resulted in repeatability of ±30 MPa for the LCR method, compared to ± 90 MPa for the shear wave method.

3.3 Sectioning Method

The method of sectioning is used for one set of residual stress measurements. The Structural Stability Research Council (SSRC) technical memorandum (Pekoz et al. 1981) is used as the primary reference for sectioning procedures, with some modifications made due to laboratory capacity at the Morrison Structural Engineering Laboratory. These modifications are:

1. The full-section test piece is removed using an oxy-acetylene torch, as the specimen is too large to saw cut.

2. Length measurements are made using an extensometer with ball bearings punched into the specimen (instead of a Whittemore gauge with gauge holes drilled in the specimen).

The sectioning method relies on the release of elastic stresses: when a section of a sample containing residual stresses is removed, stresses in the removed section are released and changes in length are observed in the directions of stress release. If these changes in length are measured, separation of a member into a series of longitudinal strips can be used to determine the longitudinal residual stress distribution over the

member cross-section. A summary of the sectioning procedure for this study is shown in Figure 3.2.

When using the method for beams and columns, it is typical to remove a test piece from the mid-point of the specimen to facilitate cutting of the test piece into longitudinal strips. Gauge length measurements are made on each strip prior to removal of the test piece, as significant stresses will be released by its removal. In order to ensure residual stresses are fully developed in the test piece, each specimen is made 3 m long, in accordance the requirements set out by the SSRC (Equation 3.6).

$$L_{specimen} \geq 3D_t + L_g + 50mm \tag{3.6}$$

where D_t is the largest transverse dimension of the specimen (900 mm for this study) and L_g is the nominal gauge length to be used (100 mm for this study).

While a smaller specimen length is permissible for the shallower specimens, the minimum length for the deepest specimens is used for all specimens for ease of fabrication.

The test piece is located in the middle of the specimen. A series of 30 mm wide strips are laid out on the test piece prior to removal from the specimen and two ball bearings punched 100 mm apart at the centre of each strip. This is performed for both sides of each strip on the flanges, but only one side on the web, as through-thickness stress gradient is not expected to be significant for the web (welding is done on both sides of the plate, as opposed to the flanges where only the interior face is welded).

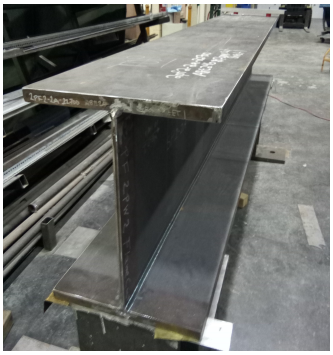

(a) Specimen prior to cutting

(b) Test piece removed

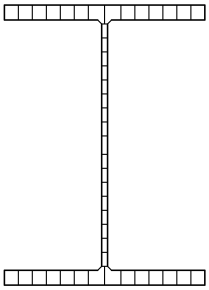

(c) Strip cut locations on test piece

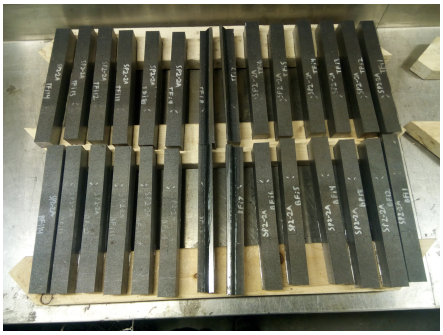

(d) Sectioned strips

Figure 3.2: Sectioning procedure

An extensometer (Figure 3.3) is then used to measure the distance between ball bearings prior to sectioning of the specimen. The device possesses a 100 mm gauge length and 1 μm resolution, allowing for a 10 με resolution (2 MPa stress resolution in steel, assuming a Young's Modulus of 200 GPa). Based on measurements taken over the course of testing, device precision is estimated as within 60 με (12 MPa)

Figure 3.3: Extensometer used for gauge length measurements

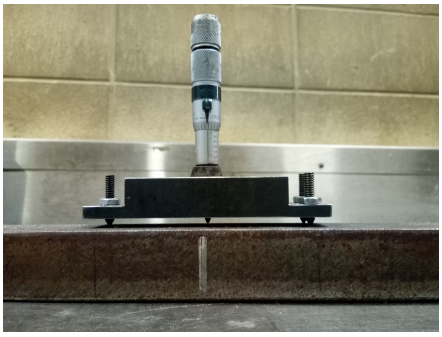

Figure 3.4: Depth-gauge used for curvature measurements

Initial strip curvature is then measured. A depth-gauge with a 1/1000 in. resolution (Figure 3.4) is used to measure the offset at the midpoint of each strip.

A 400 mm long portion of the specimen is then removed from the centre of the girder using an oxy-acetylene torch. While the minimum test piece length specified in the SSRC memorandum is 150 mm (Equation 3.7), extra distance is added to ensure heat input from flame cutting does not disturb the residual stresses within the gauge length.

$$L_{testpiece} \geq L_g + 50 \text{ mm} \tag{3.7}$$

Following flame-cutting, the test piece is cut to the minimum test piece length using a water-cooled horizontal band saw. The test piece is then sectioned into strips using the same saw. Following sectioning, final distances between each pair of ball bearings are measured using the extensometer, along with final offsets due to strip curvature in the normal direction. Strains released by sectioning are calculated using Equation 3.8.

$$\epsilon_r = \frac{L_{gi} - L_{gf}}{L_{gf}} \tag{3.8}$$

where L_{gi} and L_{gf} are the initial and final gauge lengths, respectively.

The presence of curvature in a strip will result in errors in distance measurements: chord length is measured by the extensometer, while arc length is needed for strain calculations. When curvature becomes significant ($\delta > L_g/1000$) these two values diverge. A number of equations exist to account for this difference by using an offset measurement at the midpoint of the strip. The correction proposed by Sherman (1969), which assumes a circular curve, is used in this study and is defined in Equation 3.9.

$$\epsilon_{corr} = \epsilon_r + \frac{8}{3}\left(\frac{\delta}{L_g}\right)^2 \tag{3.9}$$

where L_g is the nominal gauge length and δ is calculated using:

$$\delta = \delta_f - \delta_i \tag{3.10}$$

where δ_i and δ_f are the initial and final offsets of the strip at the mid-point, respectively.

Following strain corrections, released stress for each strip is calculated using:

$$\sigma_{rel} = E\epsilon_{corr} \tag{3.11}$$

where E is the base material Young's modulus. Positive values of σ_{rel} and ϵ_{corr} represent tensile stresses and strains, respectively, while negative values indicate compression.

During the measuring protocol, specimen temperature will not necessarily be constant. The changes in length resulting from temperature discrepancies can cause significant errors in measured strain values and must therefore be accounted for. The SSRC recommends the use of a temperature reference bar (of the same material as the specimen), which is placed on the specimen prior to testing and left until it reaches the temperature of the specimen. While the SSRC recommends leaving the reference bar overnight to reach the same temperature as the specimen, it is found that extensometer readings stabilize after approximately fifteen minutes, indicating that thermal equilibrium is achieved. It was also recommended that the measuring device (a Whittemore gauge in the SSRC guidelines) be placed on the specimen prior to measuring—allowing the device to reach the same temperature as the specimen. This

is deemed unnecessary: during a test to examine the magnitude of specimen temperature effects, a clear linear trend is observed when readings are plotted with respect to temperature (sample surface temperature was recorded using type-K thermocouples). If device temperature significantly affects readings, a deviation from linearity would be expected as the operator's hand heats up the device. Because no such trend is observed, errors due to device temperature are considered insignificant.

3.4 Ultrasonic Method

In addition to the sectioning method, a non-destructive ultrasonic technique is used to measure residual stresses in the test specimens. This is done to assess the accuracy of the UT system—to be used for future testing of real bridge girders in the fabrication shop of an industry partner. In order to be able to both generate and receive longitudinal waves in the longitudinal direction of the specimen, longitudinal critically–refracted waves (L_{CR} waves) are used. Two transducers are mounted on angle wedges such that the refracted beam generated by one transducer is parallel to the surface of the sample, and may be detected by the other transducer. The technique has seen widespread use in the literature for the measuring of bulk longitudinal stresses (see Section 3.2.2).

The complete equation relating longitudinal wave velocity with longitudinal stress (as derived by Hughes and Kelly (1953), for uniaxial stress) is shown in Equation 3.5. The effects of residual strains in the transverse and through-thickness directions induced by welding are assumed to be small, owing to the lesser constraint present in these directions compared to the longitudinal direction. This limits development of residual strains in these directions; induced stress magnitudes are therefore expected to be small compared to those in the longitudinal direction. Because the second and third order elastic constants are not measured directly (only $dV_{11}/d\epsilon$ is measured),

and because time-of-flight (TOF) is measured instead of velocity, Equation 3.5 can be simplified to Equation 3.12 (as done by Bray and Tang (2001)).

$$\sigma = \frac{E}{L_{11} TOF_0}(TOF - TOF_0) \tag{3.12}$$

where,

E = Young's modulus (MPa)

L_{11} = acoustoelastic constant for longitudinal waves propagating in the 1-direction

TOF = time-of-flight

TOF_0 = zero-stress time-of-flight

L_{11} is determined experimentally though stress calibration testing (see Section 3.4.4).

3.4.1 Measurement System

An ultrasonic probe (Figure 3.5) is designed to transmit and receive longitudinal critically–refracted waves. Two 1 in. x 2 in. narrow-band transducers with a central frequency of 1 MHz are attached to two adjustable-angle acrylic wedges, which are bonded to the specimen using an acoustic couplant. A central frequency of 1 MHz is selected in order to maximize penetration depth to avoid erroneous readings from any surface stresses generated during fabrication (e.g., sandblasting). Penetration depth has been found to be roughly equal to wavelength; Sadeghi et al. (2013) experimentally determined penetration depth to be 6.5 mm for a 1 MHz transducer. A steel housing assembly is built to maintain a constant distance between the wedges for each measurement. Because a change in distance of 1 mm can change stress readings by over 500 MPa, it is critical to ensure the wedges are fixed securely in place.

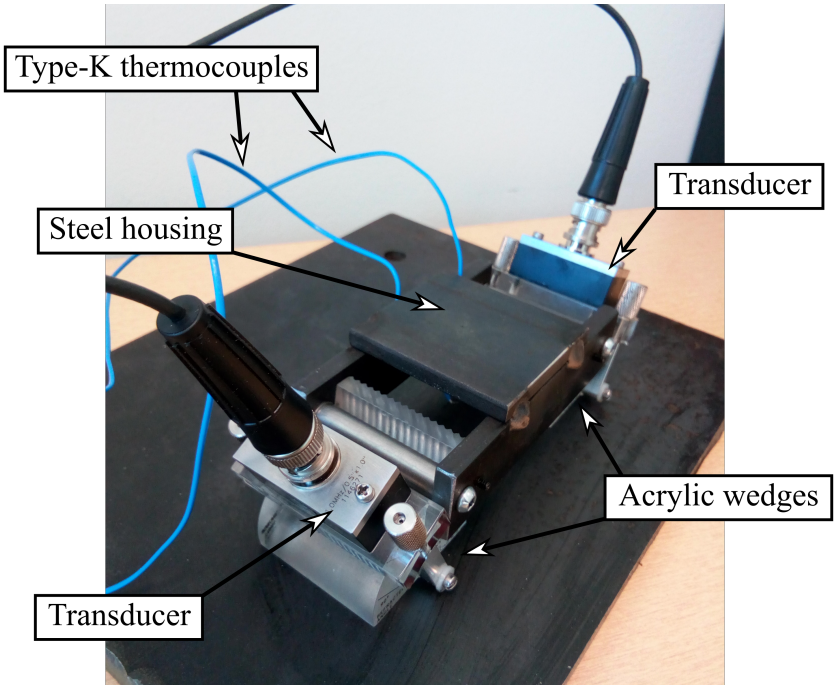

Figure 3.5: L_{CR} probe used for stress measurement

Each wedge is held in place with a pair of set screws on either side of the housing and may be removed from the housing. In order to assess the change in TOF resulting from removal of both wedges from the housing and resetting of the wedge angles, TOF readings are taken on a reference specimen before and after resetting of the probe. Readings before and after the probe reset are found to be within 10 ns of each other. Because this is less than the standard deviation observed from re-bonding of the probe to the specimen (see Section 3.4.3), this variation is deemed acceptable.

It is still possible, however, for the probe to be disturbed during the course of measurements on the girders themselves. For this reason, TOF readings are taken on a reference bar (RS1) before and after any measurements are taken with the ultrasonic system. Measured TOF values are then adjusted using the mean of the pre- and post-measurement RS1 readings.

Snell's law (Equation 3.13) is used to calculate the angle required to generate L_{CR} wave (the critical angle) for steel in this system by setting the refracted angle (θ_2) as 90° (Equation 3.14).

$$\frac{sin(\theta_1)}{v_1} = \frac{sin(\theta_2)}{v_2} \tag{3.13}$$

$$\theta_c = sin^{-1}\left(\frac{sin(90)v_{wedge}}{v_{steel}}\right) \tag{3.14}$$

where θ_c is the critical angle of refraction for longitudinal waves and v_{wedge} and v_{steel} are the longitudinal wave velocities in acrylic and steel, respectively. Wave velocity in the acrylic is reported by the manufacturer as 2720 m/s. Wave velocity in steel is taken to be 5890 m/s (reported by Olympus (2011) for Grade 1020 steel). Using these wave velocities, the critical angle is found to be 28°. It is observed, however, that the signal is still detected by the receiver even if the angle is not exactly equal to the critical angle. The angle is thus set at approximately 30°.

In order to generate the signals, a DPR300 ultrasonic pulser/receiver is used. Output from the DPR300 is then sent to a Tektronix MDO3022 oscilloscope to be digitized and sent to a computer for processing. A sample rate of 2.5 GS/s allows for a time resolution of 0.4 ns. This is required, as expected TOF sensitivity is on the order of 1 ns/MPa.

Surface and housing temperatures are measured using a thermometer connected to type-K thermocouples.

3.4.2 Signal Processing

Signal processing is done in LabVIEW. A typical A-scan is shown in Figure 3.6.

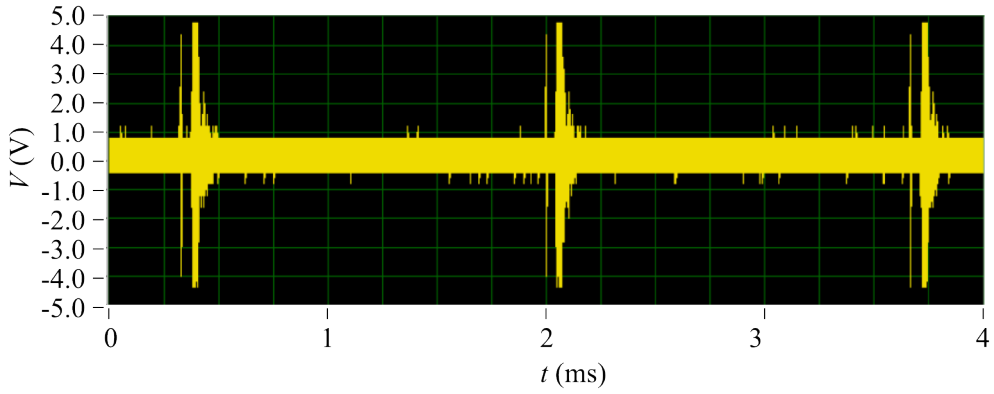

Figure 3.6: Typical A-scan

Peak Detection Transmitted and received pulses are both contained within the same waveform. In order to measure TOF, it is necessary to distinguish between transmitted and received pulses. This is done by assessing the frequency content of all pulses exceeding a user-defined voltage threshold. The transmitted pulse is output directly from the pulser-receiver, while the received pulse passes through both wedges and the specimen before being output. Higher frequency content will therefore be attenuated in the received pulse. This is used to distinguish transmitted pulses from received pulses in the recorded A-scan: it is found that transmitted pulses exhibit a 10 MHz peak, which is absent from received pulses. All pulses above an operator-defined voltage threshold are analysed using a fast-Fourier transform. Signals with a 10 MHz peak are then flagged as transmitted pulses. The received pulse is then taken as the first peak following the transmitted pulse that exceeds a separate, user-defined threshold. Detected pulse locations for a typical transmitted and received pulse pair are shown in Figure 3.7.

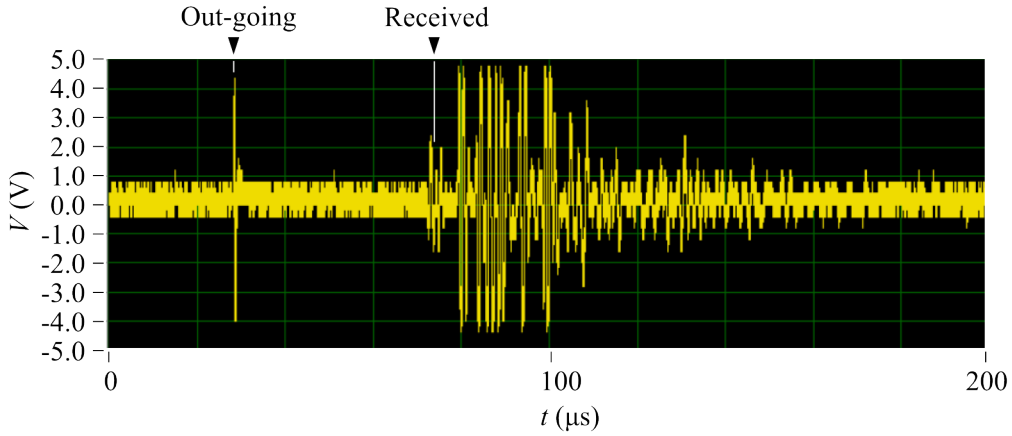

Figure 3.7: Detected pulse locations on A-scan of transmitted and received pulses

While no filters are used in detection of the transmitted pulse, a band pass filter with high pass and low pass cut-off frequencies of 0.75 MHz and 1.25 MHz, respectively, is applied to the signal for received pulse detection in order to improve pulse detection precision (Pereira et al. 2016). The location on the received pulse is taken as the first zero-crossing after the first peak that exceeds the detection threshold, following the signal processing procedure of Pereira et al. (2016)(Figure 3.8).

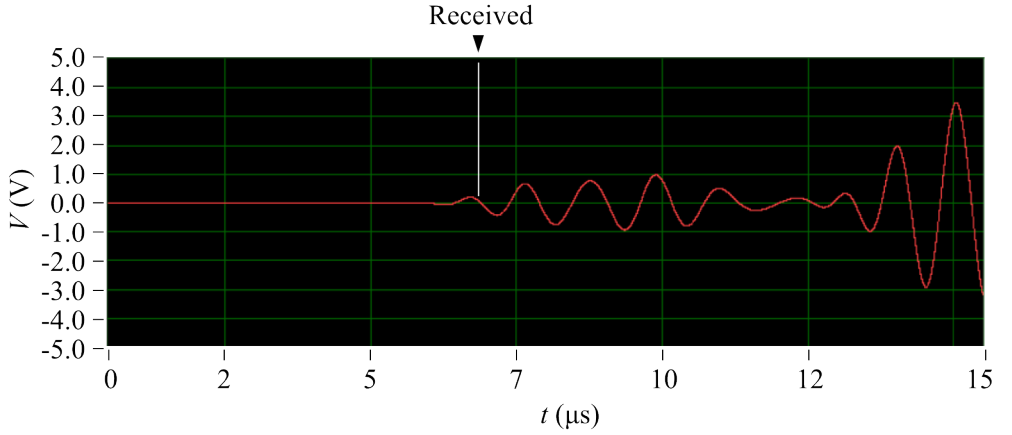

Figure 3.8: Detected pulse location on A-scan of received pulse after band pass filtering

3.4.3 Preliminary Testing

Past work on the measurement of residual stresses using L_{CR} waves has used a load cell to apply a constant pressure to the probe. This is to ensure a constant thickness of the couplant layer between the probe and specimen, as changes in the thickness of this layer can affect TOF readings (Sadeghi et al. 2013). The geometry of the specimen rendered such a configuration impractical, however, as it is desired to be able to take measurements immediately adjacent to the weld on both the flanges and web. Tests are done to examine repeatability of readings when hand pressure is applied to the probe through a spring; it is found that application of pressure for 60 s results in a standard deviation between measurements of less than 20 ns (roughly 65 MPa to 90 MPa, based on results from the stress calibration test (Section 3.4.4)). This is confirmed during measurements on the test girders themselves: readings are found to stabilize within 60 s for non-sandblasted surfaces, and within 45 s for sandblasted surfaces. It is thought that this reduction is due to the rougher surface accelerating consolidation by trapping couplant in surface troughs.

3.4.4 Stress Calibration Test

Owing to the variability of the acoustoelastic constant and the stress-free TOF, TOF_0 (see Equation 3.12), a stress calibration test is performed for each plate thickness used in the tested specimens. Tests are carried out using an MTS1000 load frame. The test setup is shown in Figure 3.9.

Four samples are tested: one for each plate thickness used in the test girders. One 500 mm long sample from each plate thickness is plasma-cut from the plate stock; dimensions of each sample are given in Table 3.5. Two tests are done for each plate thickness in the as-received condition (to examine repeatability) and one after stress-

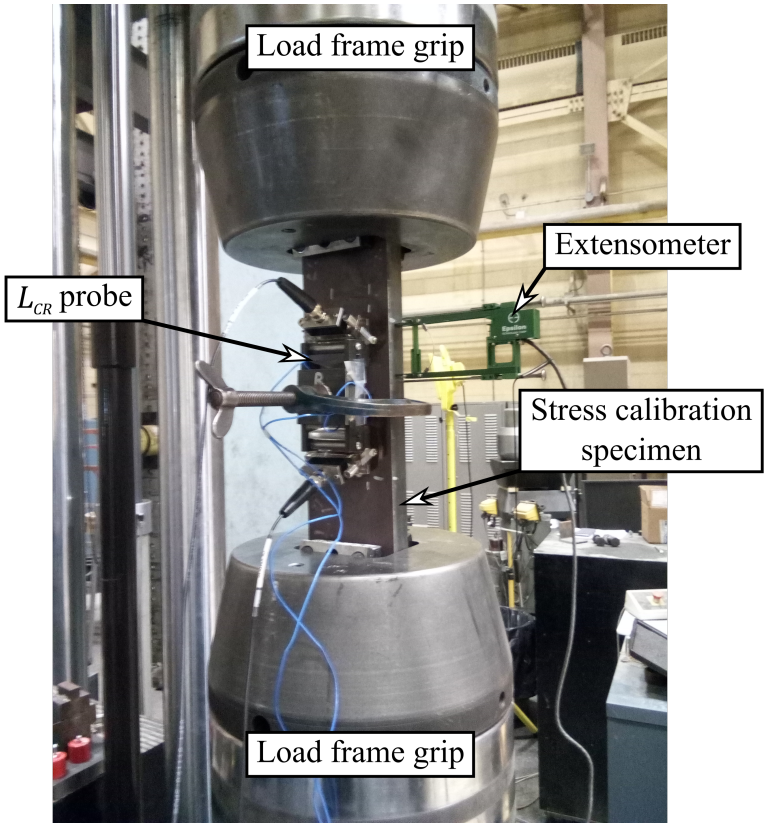

Figure 3.9: Ultrasonic stress calibration test setup

relieving heat-treatment (to examine its effects on the calibration curves). For stress-relieving, samples are held at 650 °C (1200 °F) for two hours and then furnace-cooled.

Because samples must be gripped in the vertical position, the ultrasonic probe is clamped to the sample for the duration of the test. Prior to gripping of the sample, a TOF reading is taken. The sample is then gripped and tensile force increased by increments of approximately 50 kN to 70 kN until stress reaches 80% of the nominal yield stress, with TOF and temperature readings taken at each point (though the capacity of the load frame limits maximum testable stress to only 60% and 40% of nominal yield stress for the 25 mm and 32 mm samples, respectively). Readings are taken again during unloading (at the same stress levels as loading) and after the mechanical grips are released, to ensure minimal hysteretic behaviour. Compressive

Table 3.5: Ultrasonic stress calibration sample dimensions

Sample ID	thickness (mm)	width (mm)
UTC32	32.0	102
UTC25	25.2	102
UTC13	13.0	102
UTC10	10.1	102

behaviour is not tested: the TOF–stress relationship is assumed to be identical in compression and in tension.

Total applied load is determined using a load cell built into the test frame. Stress values are then calculated using measured cross-section dimensions of the sample. An extensometer is also used to measure strains in order to confirm elastic behaviour. Some non-linearity in the stress–strain curve is observed during the loading phase, likely due to extensometer slippage. A more linear stress–strain relationship is observed for unloading; the unloading portion of the test is therefore used in calculating TOF–stress curves (Table 4.3).

3.4.5 Temperature Calibration Test

In order to quantify the effect of specimen surface temperature on TOF measurements, a temperature calibration test is carried out. A portion from the top flange of SP3 is used for this test, with measurements taken on the interior face of the sample. A water bath is prepared on top of a hot plate. The sample is then placed in a water bath with the bottom portion submerged and the ultrasonic probe clamped to the top surface. The temperature of the sample is slowly increased, with TOF readings taken roughly every 0.5 °C. Temperature is measured on the top surface of the sample at both ends and at the mid-point to ensure even heating of the sample. The test setup is shown in Figure 3.10.

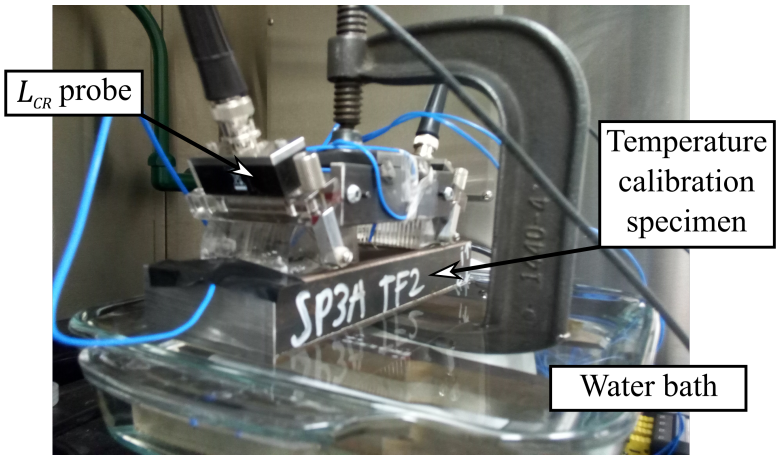

Figure 3.10: Temperature calibration test setup

3.4.6 Measurement Procedure on Test Girders

Prior to taking measurements, the girder surface is cleaned with a degreasing agent. The contact surfaces of both wedges are wiped with a damp cloth. Measurements are then taken on a reference bar (RS1) to account for any discrepancies in TOF resulting from movement of the probes within the housing. Three measurements are taken, rebonding the probe each time to capture variation due to thickness of

the couplant layer (standard deviation of roughly 20 ns). Pressure is applied for 60 s prior to each measurement to ensure consistent thickness of the couplant layer between readings. Each of these three measurements consists of nine TOF readings, the average of which is taken as the measured value. Surface and housing temperature are recorded immediately following TOF measurement.

Measurement of strips on the girder then proceeds, following the same procedure as measurements on the reference bar.

Temperature correction Temperatures of both the specimen surface underneath the probe and the probe housing are recorded at the end of each reading. Temperature corrections are applied by normalizing temperatures to 0 °C (Equation 3.15).

$$TOF = TOF_{meas} - m_T T_{surf} \tag{3.15}$$

where:

TOF_{meas} = measured TOF
m_T = TOF–temperature slope (experimentally determined, see Section 4.2.2)
T_{surf} = specimen surface temperature

While the changes in temperature of the steel housing affect the distance between the probes (and consequently the TOF reading), this change is expected to be minimal. For $\alpha = 11{\times}10^{-6}$, $L = 100$ mm and $v_{steel} = 5890$ m/s, TOF sensitivity is calculated as less than 0.2 ns/ °C. As such, corrections are not applied for housing temperature.

RS1 correction Readings are taken on the reference bar (RS1) for every 7-10 strips measured on the specimen to minimize errors due to housing slippage. Temperature

corrections are applied to the RS1 readings using the results from Section 3.4.5; temperature response is assumed to be the same in RS1 and the measured specimens. Following temperature correction, the average of the RS1 readings from before and after a given set of measurements is used to correct the set.

Strip widths Measurements are made on each strip to be cut in the sectioning process. Because the probe is 43 mm wide and the strips only 30 mm wide, a deconvolution algorithm must be used to calculate the actual stresses for the sectioning strip widths.

$$TOF_i = \frac{TOF_{i(m)} W_i - TOF_{OL} X_L - TOF_{OR} X_R}{S_i} \tag{3.16}$$

where:

TOF_i = actual mean TOF for strip i

$TOF_{i(m)}$ = measured mean TOF for measured width i

W_i = measured width

S_i = strip width (30 mm, except for strips adjecent to weld, see below)

X_L, X_R = overlap distance of probe onto $i-1$ and $i+1$ strips, respectively

TOF_{OL}, TOF_{OR} = mean TOF in overlap region of probe onto $i-1$ and $i+1$ strips, respectively, defined as:

$$TOF_{OL} = TOF_i - \frac{TOF_i - TOF_{i-1}}{S_i/2 + S_{i-1}/2}(S_i/2 + X_L/2) \tag{3.17}$$

$$TOF_{OR} = TOF_i + \frac{TOF_{i+1} - TOF_i}{S_{i+1}/2 + S_i/2}(S_i/2 + X_R/2) \tag{3.18}$$

The probe is aligned with the strip edge closest to the plate centre for the flanges and the edge closest to the top flange for the web. For strips adjacent to the weld, only a portion of the width is measurable due to the screws on either side of the acrylic wedges. The measurable width is recorded and set as S_i for these strips.

Equations 3.17 and 3.18 are substituted into 3.16 and the resulting equation rearranged for TOF_i. The resulting equation is applied to each strip measured over the plate width, resulting in an $n \times n$ system of equations, where n is the number of strips in the considered plate. This system of equations is solved to compute the deconvoluted TOF for all strips.

3.5 Summary

Methods are presented for a residual stress measurement program on a set of four welded steel test girders. The sectioning method is used a baseline by which the accuracy of an ultrasonic stress measurement technique can be examined. Past work has found the use of longitudinal critically–refracted waves to be the most appropriate ultrasonic method for measuring bulk longitudinal residual stresses. Such waves are are used for the current study.

Chapter 4

Experimental Results and Discussion

Results from both the sectioning and ultrasonic tests (UT) are presented in this chapter. The accuracy of both methods is examined and potential causes of errors discussed.

4.1 Sectioning Stress Measurement

4.1.1 Measured Residual Stress Distributions

Residual stress distributions obtained using the sectioning method are presented in Figures 4.1 through 4.4. Stresses are determined from the measured strains using measured values of Young's modulus (given in Table 3.1). For the flanges, measured values are shown for both the interior and exterior face, along with the calculated average through-thickness value. Points are only plotted for one side of the web,

as measurements are only taken on one side, but through-thickness variations are assumed to be negligible, so these distributions are taken as the average as well. For several measurements, one of the ball bearings fell out during the course of cutting. New ball bearings are hammered into the original depression location and while these readings are considered to remain accurate, it is possible that this process altered the location of the ball bearing slightly and thus introduced an error in the reading. Such points are marked in red in Figures 4.1 through 4.4.

Measured offsets due to strip curvature are within $L_g/1000$. Errors due to curvature are therefore insignificant (less than the resolution of the extensometer), such that it is not necessary to apply corrections.

Ball bearings are punched and measured on the weld bead for all specimens (with the exception of SP2-2). Despite the fact that the weld bead itself is not separated from the adjacent strip, a significantly higher released strain is measured on the weld face compared to the measurement by the weld toe. Such strains always exceed the base material yield strain (1722 με to 1787 με, from measured values for yield stress and Young's modulus, see Table 3.1). This is expected as the electrode has a nominal yield strain of 2400 με (based on reported yield stress from the supplier of 480 MPa, E assumed 200 GPa).

Weld bead readings are shown on the residual stress distribution plots of both the flanges and the web (Figures 4.1, 4.3 and 4.4). Such values are not used in the calculation of average though-thickness stress as the stress measured on the weld face does not represent a residual stress value on the plate surface (required for through-thickness average calculations).

It is noted that the measured stress magnitudes at the edges of the flanges are significantly lower than those reported in much of the literature data. This is thought

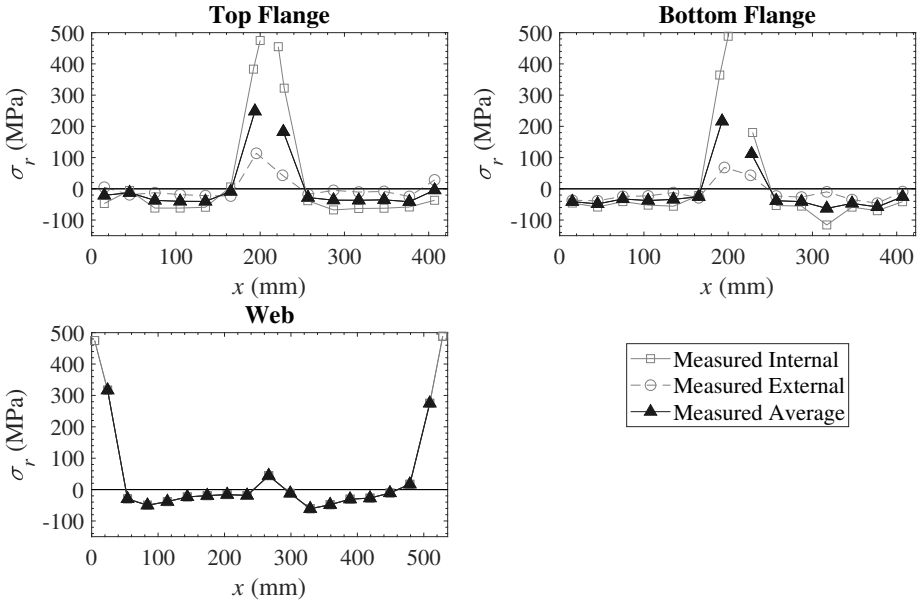

Figure 4.1: Residual stress distribution measured by sectioning (SP2-1)

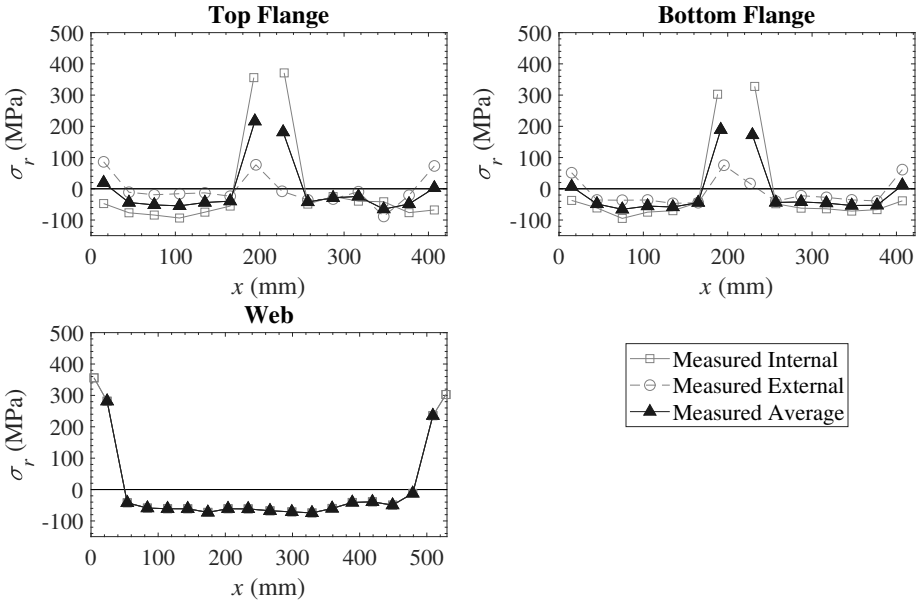

Figure 4.2: Residual stress distribution measured by sectioning (SP2-2)

be due to the use of 30 mm wide strips, which do not provide sufficient resolution to measure peak tensile stresses at the edges of the flanges.

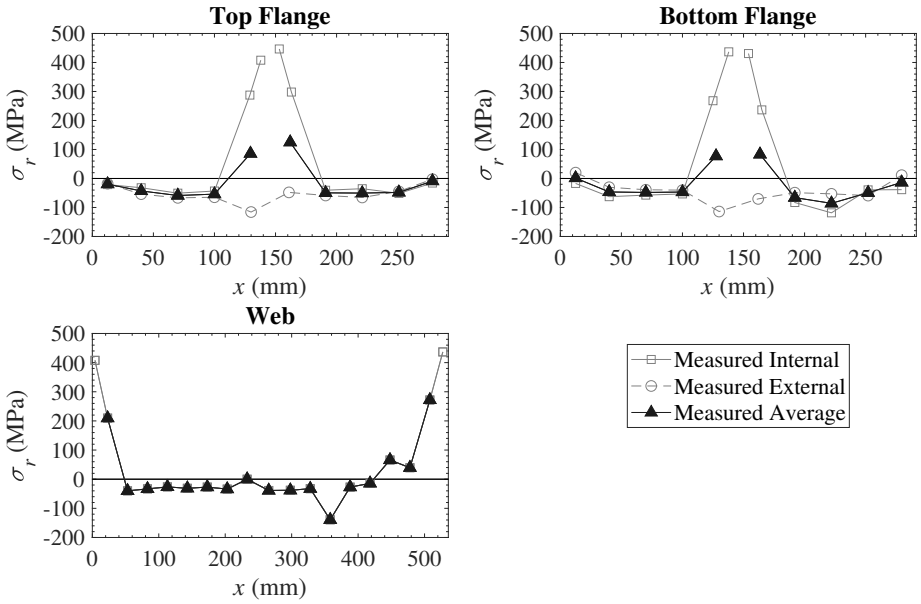

Figure 4.3: Residual stress distribution measured by sectioning (SP3)

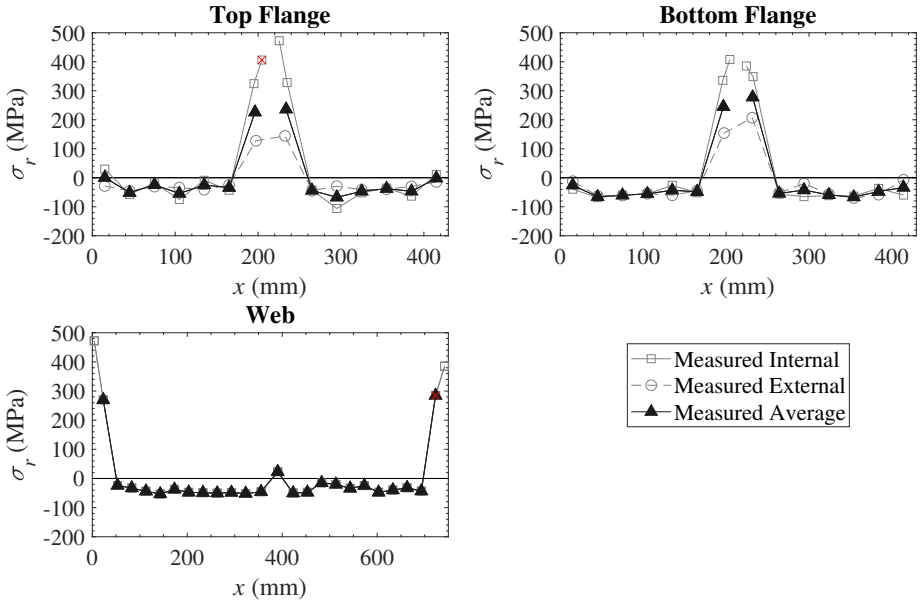

Figure 4.4: Residual stress distribution measured by sectioning (SP4)

4.1.2 Closing Forces

Because the residual stresses are self-equilibrating, the sum of the resulting internal forces should be equal to zero (Equation 4.1).

$$F_{net} = \sum_{i=1}^{n} \sigma_{ri} A_i \tag{4.1}$$

where σ_{ri} and A_i are the average stress and cross-sectional area of each sectioned strip, respectively, and n is the total number of strips over the cross-section. Internal forces based on measured residual stress values are summed as a means of verification of the accuracy of the method—net forces are presented in Table 4.1. Net force is compared to the total internal force, defined as:

$$F_{total} = \sum_{i=1}^{n} |\sigma_{ri}| A_i \tag{4.2}$$

Accuracy appears to be good: net forces represent less than 10% of the associated total internal force for all specimens. It should be noted that because measurements are not taken on the weld beads of specimen SP2-2, the force from the weld area is assumed to be equal to that for SP2-1.

Table 4.1: Closing forces of residual stress distributions measured by sectioning

Specimen	Top Flange		Bottom Flange		Web		Section		
	Total (kN)	Net (kN)	Total (kN)	Net (kN)	Total (kN)	Net (kN)	Total (kN)	Net (kN)	Net/Total %
SP2-1	795	144	818	-116	473	180	2085	207	9.9
SP2-2	879	35	892	-73	570	-75	2341	-113	-4.8
SP3	551	-69	530	-133	474	103	1554	-98	-6.3
SP4	750	104	915	15	614	-31	2279	88	3.9

4.2 Ultrasonic Stress Measurement

Results from the calibration tests for stress and temperature are presented and discussed in this section. Stress readings on the test girders are then compared with sectioning results and potential sources of error discussed.

4.2.1 Stress Calibration Test

Results for the stress calibration test described in Section 3.4.4) are presented and discussed in this section. In order to confirm repeatability of results, each sample is tested twice in the pre-heat-treated condition. Results for both tests prior to heat-treatment are shown in Table 4.2. There appears to be significant variation in both the slope ($\Delta TOF/\Delta\sigma$) and y-intercept (TOF_0). Up to 26% changes in slope are observed and changes in TOF_0 exceed the standard deviation observed due to re-bonding of the probe (20 ns; see Section 3.4.3). While the exact cause of this discrepancy is unknown, it is thought that it is caused by slippage of the housing (which can introduce errors of up to 70 ns; see Section 4.2.3). Mean values of the two pre-heat-treatment curves for $\Delta TOF/\Delta\sigma$ and TOF_0 are used in the subsequent discussion.

Table 4.2: Time-of-flight–stress curve parameters for both sets of pre-heat-treatment stress calibration tests

Sample	$\Delta TOF/\Delta\sigma$			TOF_0		
	#1 (ns/MPa)	#2 (ns/MPa)	Change %	#1 (ns)	#2 (ns)	Change (ns)
UTC32	0.377	0.279	26	45836	45881	45
UTC25	0.277	0.330	19	45905	45891	14
UTC13	0.280	0.250	11	45894	45872	22
UTC10	0.192	0.236	23	45809	45823	14

Time-of-flight–stress (TOF–stress) curves for the pre- and post-heat-treated samples are shown in Figure 4.5. A linear regression is used to fit curves to the points measured during unloading of the samples. The slope of this curve is taken as $\Delta TOF/\Delta\sigma$, while the TOF after the sample is released from the frame grips is taken as TOF_0. Fitted curves for the pre- and post-heat-treated samples are shown in Figure 4.5. Values for the acoustoelastic constant, L_{11}, are calculated for each sample by rearranging Equation 3.12:

$$L_{11} = \frac{E}{TOF_0}\frac{\Delta TOF}{\Delta\sigma} \tag{4.3}$$

where E is Young's modulus of the material. Curve parameters and calculated values of the acoustoelastic constant are shown in Table 4.3. The Young's modulus is not measured for the 10 mm plate as only specimens with 13 mm webs are tested in this study. The value for the 13 mm plate is therefore used in calculation of L_{11} for the 10 mm plate. Further information for the stress calibration tests can be found in Appendix C.

Table 4.3: Time-of-flight–stress curve parameters (pre-and post-heat-treatment)

Sample ID	$\Delta TOF/\Delta\sigma$ (ns/MPa)	TOF_0 (ns)	L_{11}
PREHT			
UTC32	0.328	45859	1.44
UTC25	0.303	45898	1.34
UTC13	0.265	45883	1.18
UTC10	0.214	45816	0.95
POSTHT			
UTC32	0.306	45917	1.34
UTC25	0.260	45946	1.14
UTC13	0.220	45829	0.98
UTC10	0.222	45760	0.99

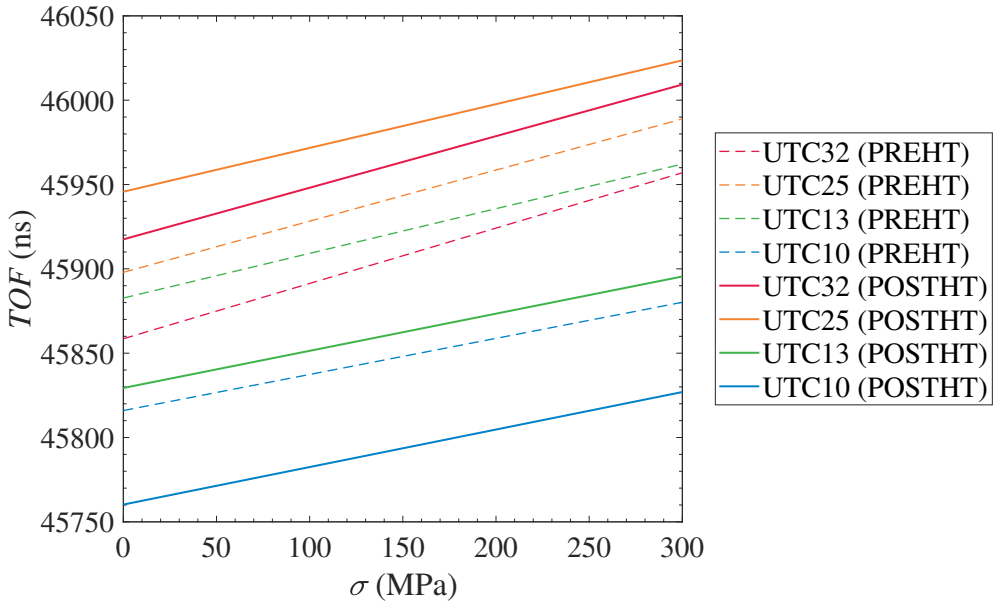

Figure 4.5: Time-of-flight–stress curves (pre- and post-heat-treatment)(stress relieving: 650°C for two hours)

No past studies of L_{CR} stress calibration tests on Grade 350W steel were found in the literature. Santos et al. (2004) conducted L_{CR} stress calibration tests on API Grade 5L X70 steel and reported L_{11} values of 1.70 and 1.52, before and after heat-treatment, respectively. These are significantly higher than those found in the current study—this is attributed to differences in material properties among the two grades.

It is also noted that, for the pre-heat-treatment curves, $\Delta TOF/\Delta\sigma$ decreases with plate thickness. It is thought that this is due to small variations in the second- and third-order elastic constants among the different thicknesses. Because only Young's modulus was directly measured, however, it is not possible to draw further conclusions regarding this effect.

4.2.1.1 Effects of Heat Treatment

Values for the TOF–stress curve parameters $\Delta TOF/\Delta\sigma$ and TOF_0 before and after heat-treatment at 650 °C for 2 hours are shown in Figures 4.6 and 4.7. Zero-stress TOF (TOF_0) is observed to increase after heat-treatment for UTC32 and UTC25, but decrease for UTC13 and UTC10.

Stress calibration samples are hand sanded following heat-treatment to remove any surface oxidation. It should be noted that this process resulted in flaking off of the mill scale for samples UTC10 and UTC13. In order to maintain a consistent surface between tests, mill scale is removed by hand from all samples prior to conducting the post-heat-treatment calibration tests. It is therefore necessary to examine the effects of mill scale removal on the TOF–stress curve. Curves reported bySantos et al. (2004) show a change in slope of 10% due to heat-treatment. Because changes in slope from pre- to post-heat-treatment curves in the current study range from 6% to 16% , the change in slope between the pre- and post-heat-treatment curves is assumed to be primarily due to the effects of heat-treatment and not removal of mill

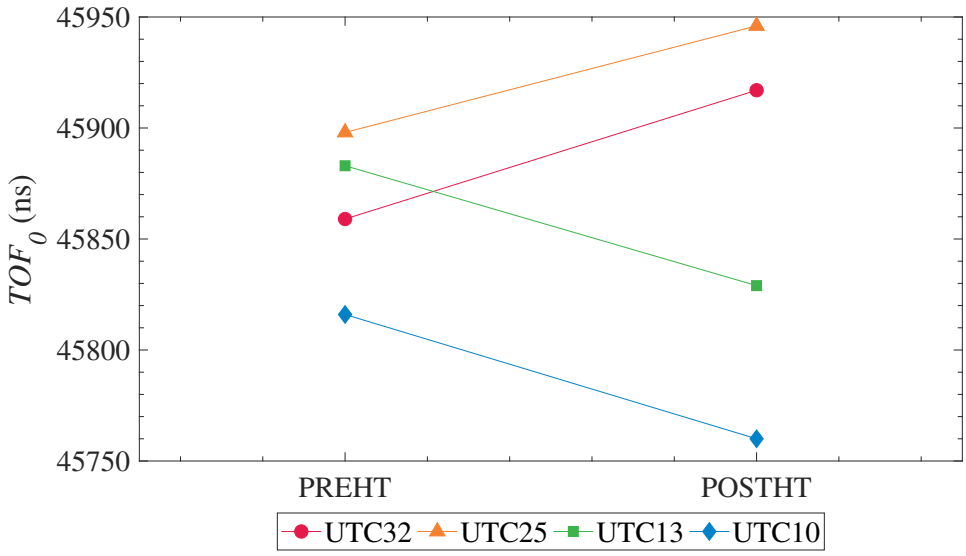

Figure 4.6: Change in TOF_0 from heat-treatment

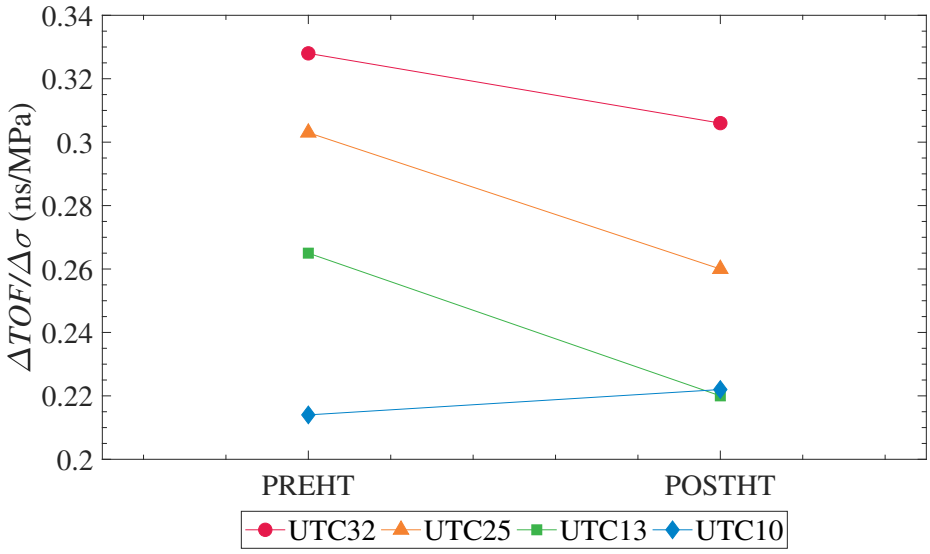

Figure 4.7: Change of $\Delta TOF/\Delta\sigma$ from heat-treatment

scale. It is therefore assumed that the presence of mill scale does not affect the slope of the TOF–stress curve, such that only the y-intercept (TOF_0) needs be checked. In order to quantify the effects of removal of mill scale on the zero-stress TOF reading, TOF measurements are taken on the opposite side of each UTC sample (to that measured during the stress calibration tests) with no external load applied. Results are compared to the zero-stress TOF readings from the associated stress calibration

test—values are shown in Table 4.4. Changes in TOF resulting from removal of mill scale exhibit a large degree of scatter: standard deviation of the change is 74 ns, well above the standard deviation inherent to rebonding (20 ns). It is therefore concluded that other factors are influencing the results (such as differences between the surfaces of the two opposite faces of the samples).

Table 4.4: Zero-stress TOF readings for stress calibration test samples with and without mill scale (post-heat-treatment)

Sample	TOF		
	With mill scale (ns)	Without mill scale (ns)	Change (ns)
UTC32	45917	45920	3
UTC25	45946	46044	98
UTC13	45829	45992	163
UTC10	45760	45918	158
		MEAN	106
		STDEV	74

4.2.1.2 Effects of Clamping Force on Probe

When conducting tests on the stress calibration samples outside of the load frame (using only a spring to apply pressure to the probe; see Section 3.4.3), it is observed that TOF readings are higher than those observed at zero-stress (i.e., when the grips are released) during the calibration test. This is attributed to the use of a clamp to attach the probe to the sample during the calibration test, which further consolidates the couplant layer, resulting in a reduction in measured TOF. Testing is done to quantify this effect: pressure is applied using a spring for 60 s and then TOF is measured. The probe is then clamped to the sample and another TOF reading taken after 60 s. The change between the two readings is consistent—changes from the spring pressure to clamped conditions are shown in Table 4.5. The mean reduction in

TOF due to clamping is found to be 57 ns. Standard deviation among the samples is 20 ns, which is equal to that observed by regular rebonding of the probe to a surface: the change in TOF due to clamping therefore appears be consistent; the TOF–stress curves are adjusted to account for this effect by adding 57 ns to the TOF_0 value.

Table 4.5: Change in TOF between spring pressure and clamped configurations

Sample	ΔTOF (ns)
UTC32	-85
UTC25	-44
UTC13	-58
UTC10	-40
MEAN	-57
STDEV	20

4.2.2 Temperature Calibration Test

Results from the temperature calibration test described in Section 3.4.5 are presented in this section. TOF readings from the unstressed temperature calibration test are plotted against temperature readings at the centre of the sample and the slope calculated (Figure 4.8). A slope of 24 ns/°C is found. This value is used for temperature corrections in all measurements taken (including those taken during stress calibration tests). It is noted that a change in temperature of 1°C produces a change in TOF equivalent to 73 to 112 MPa (based on the TOF–stress curves in Table 4.3), highlighting the importance of temperature measurement and correction during testing.

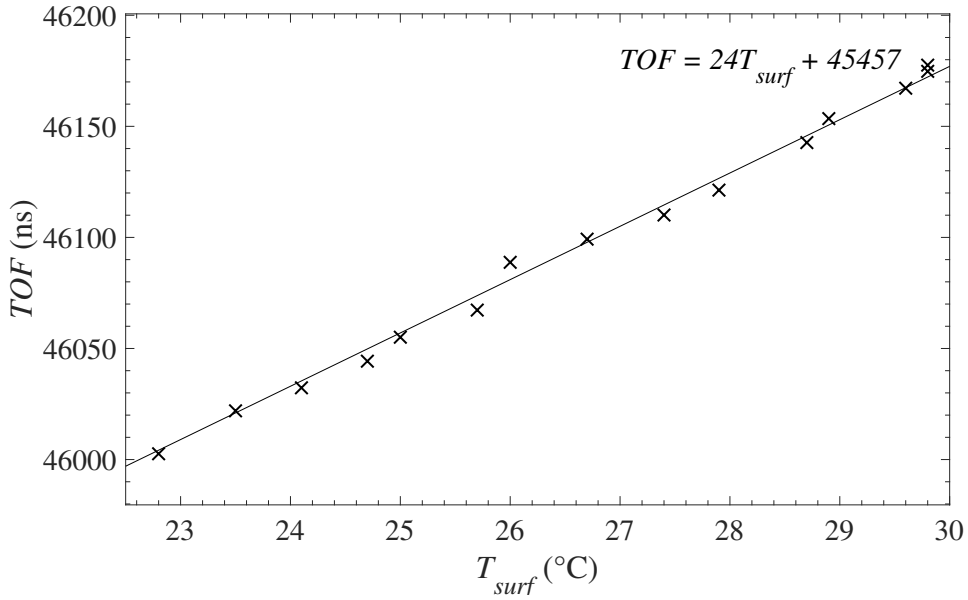

Figure 4.8: Time-of-flight vs. sample surface temperature for the temperature calibration test

4.2.3 Stress Measurements on Test Girders

Stress measurements are taken on each of the four test girders at the same locations as sectioning measurements. Results are presented in this section.

TOF–stress curve parameters used in the subsequent discussion are shown in Table 4.6. Post-heat-treatment curve parameters are used, with TOF_0 values increased by 57 ns to account for the use of a clamp during the calibration tests (see Section 4.2.1.2).

Table 4.6: TOF–stress curve parameters used in measurements on girders

Plate thickness (mm)	$\Delta TOF/\Delta\sigma$ (ns/MPa)	TOF_0 (ns)
32	0.306	45974
25	0.260	46003
13	0.220	45886
10	0.222	45817

TOF measurements are taken on each of test girders. TOF values are then corrected for temperature by normalizing to 0 °C (using measured surface temperature and the slope of the TOF–temperature curve from Section 4.2.2). Values are also corrected for housing slippage using TOF measurements on the reference sample RS1 before and after the measurements taken on the girder. A deconvolution algorithm is then applied to the measurements to account for the fact that the probe is wider than the strip width for sectioning. Details of the measurement procedure are described in Section 3.4.6.

Because the deconvolution algorithm adjusts the TOF values at all locations based on adjacent values, it is important to remove outliers from the data set prior to deconvolution to minimize propagation of random errors to adjacent locations. On each strip, three TOF measurements are taken. Each of these TOF measurements

consists of nine TOF readings. Outliers are observed among both the three TOF measurements on a single strip and nine TOF readings for a single TOF measurement. Both cases are discussed.

Time-of-flight Measurements In general, three TOF measurements are taken on a given strip. A TOF measurement, TOF_{meas} is considered an outlier if:

$$|\frac{TOF_{meas} - mean(TOF_{meas})}{std(TOF_{meas})}| > q_{strip} \tag{4.4}$$

where q_{strip} is determined based on a statistical analysis of the data. Because the sample size is small, q cannot simply be set as a constant value of 1 or 2. It is found that a q_{strip} value of 1.147 finds outliers in 32% of measurements (i.e., those more than one standard deviation away from the mean, assuming a normal distribution). This value is used in assessing outliers for TOF measurements. Such outliers are excluded from the calculation of mean TOF for a given strip.

Time-of-flight Readings Nine TOF readings are taken for each measurement and the mean value taken as the TOF measurement value. The same criterion is used for outliers as in the case of the TOF measurements. A TOF reading, TOF_{read} is considered an outlier if:

$$|\frac{TOF_{read} - mean(TOF_{read})}{std(TOF_{read})}| > q_{meas} \tag{4.5}$$

However, because sample size is larger than in the case of TOF measurements (n = 9), a different q value must be used (q = 1.147 for n = 9 will result in a larger percentage of the data classified as outliers than for n = 3). It is found that a q_{meas}

Table 4.7: Closing forces of residual stress distributions measured by ultrasound

Specimen	Top Flange		Bottom Flange		Web		Section		
	Total (kN)	Net (kN)	Total (kN)	Net (kN)	Total (kN)	Net (kN)	Total (kN)	Net (kN)	Net/Total %
SP2-1	1417	501	1360	-399	4544	4236	7321	4337	59
SP2-2	1791	1791	1947	-1947	5209	5209	8946	8946	100
SP3	1410	1022	1802	-1678	3002	3002	6215	5702	92
SP4	1587	1233	699	300	3282	3249	5568	4781	86

value of 1.936 finds outliers in 32% of strips. Outliers are excluded from calculation of the mean TOF for the measurement.

Stress readings from the ultrasonic method with outliers removed are shown with sectioning results in Figures 4.9 through 4.12, with measurements exceeding the yield stress marked as closed red circles. While there are instances in which agreement is close between the two methods, the ultrasonic measurements generally tend to exhibit a large degree of scatter and do not agree well with the sectioning values. Such scatter is thought to be due in part to differences in surface texture: interior flange faces along with the web are sandblasted, while the exterior flange faces are not. Housing slippage between measurements may also contribute to scatter, as variations in readings on the reference bar (RS1) before and after a set of girder measurements vary by up to 100 ns (325 to 455 MPa, using the post-heat-treatment TOF–stress curves).

In addition to data scatter, systematic errors appear to be present in the data. This can be clearly seen from a summation of internal forces using measured stress values (as outlined in Section 4.1.2)(Table 4.7). Accuracy is poor: forces are predominantly tensile, with girder SP2-2 showing no compressive force over the entire section.

Though random errors for single strips/measurements exist, only the systematic errors affecting larger portions of the data set are discussed in this section. Mean stress over

the entire width of a given plate is examined, along with detection of peak tensile stresses around the weld. Compressive stress magnitude is not examined due to the magnitude of scatter being larger than that of the expected values.

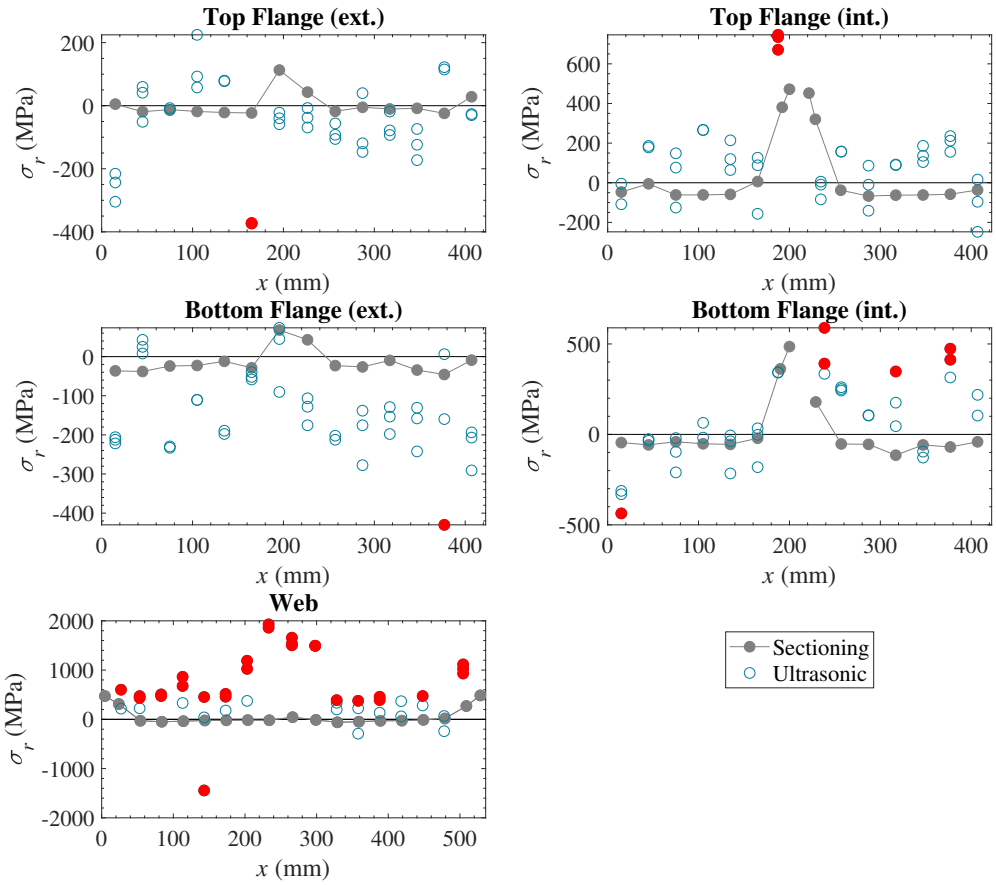

Figure 4.9: Comparison of ultrasonic and sectioning data for girder SP2-1 (using post-heat-treatment TOF–stress curves)

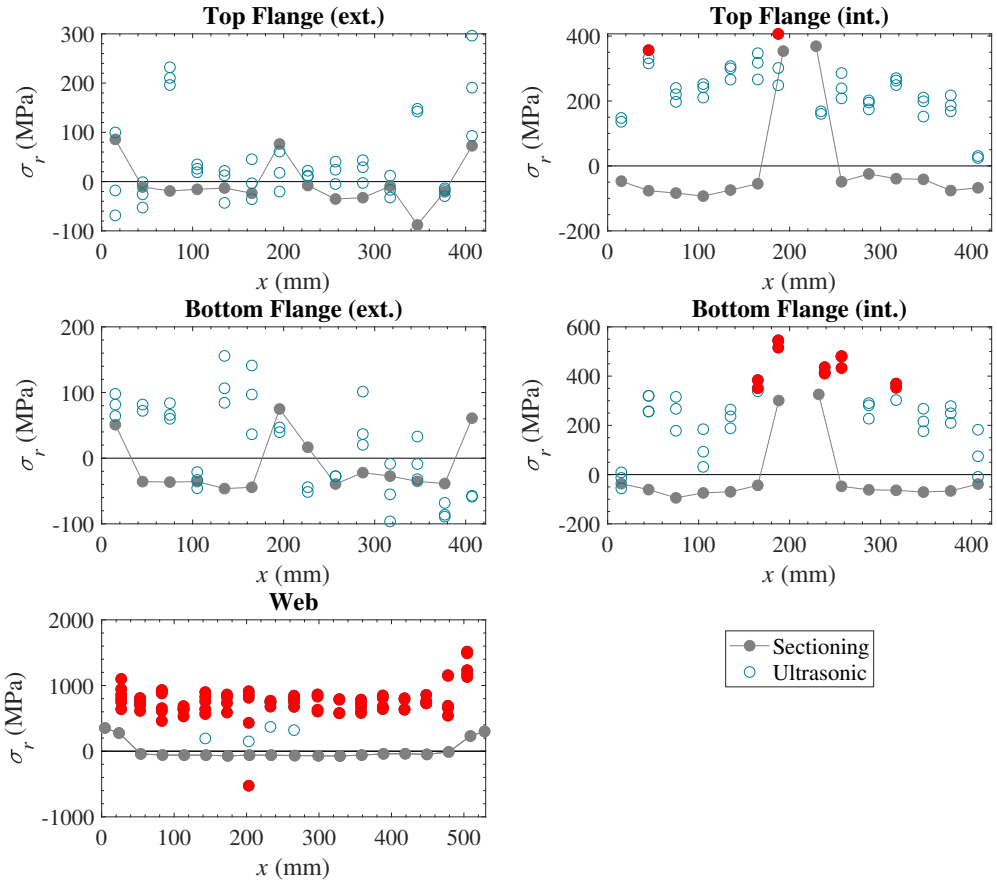

Figure 4.10: Comparison of ultrasonic and sectioning data for girder SP2-2 (using post-heat-treatment TOF–stress curves)

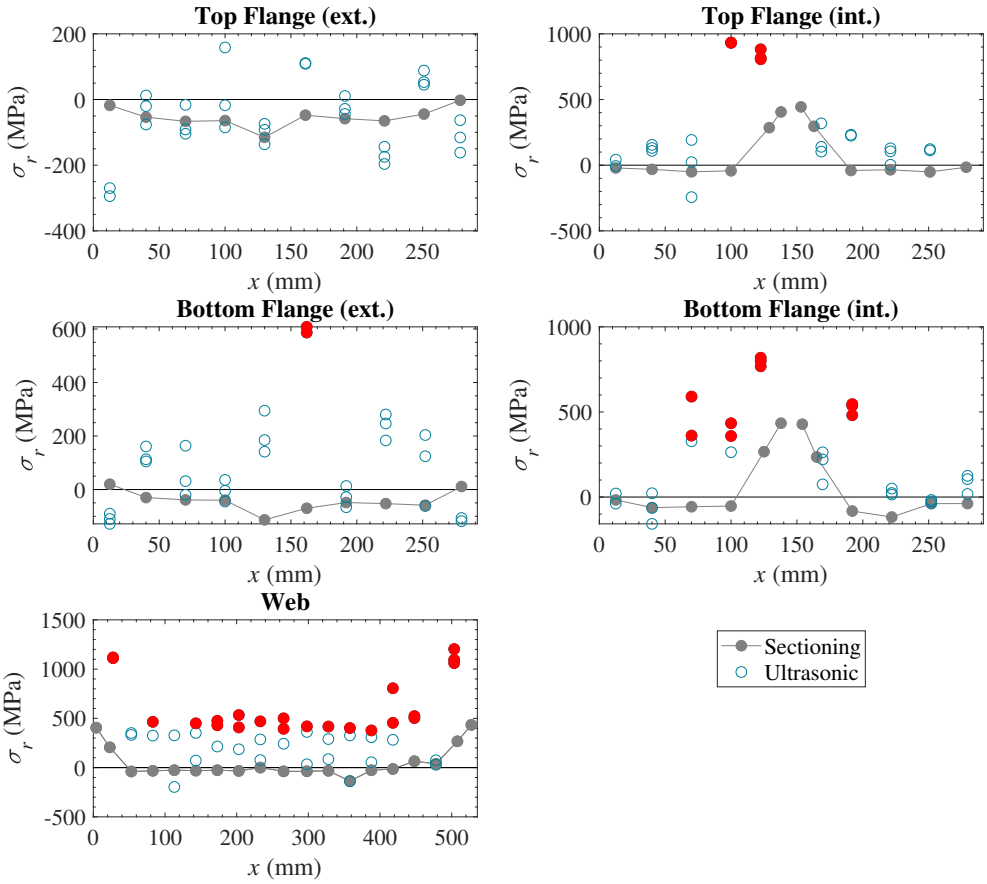

Figure 4.11: Comparison of ultrasonic and sectioning data for girder SP3 (using post-heat-treatment TOF–stress curves)

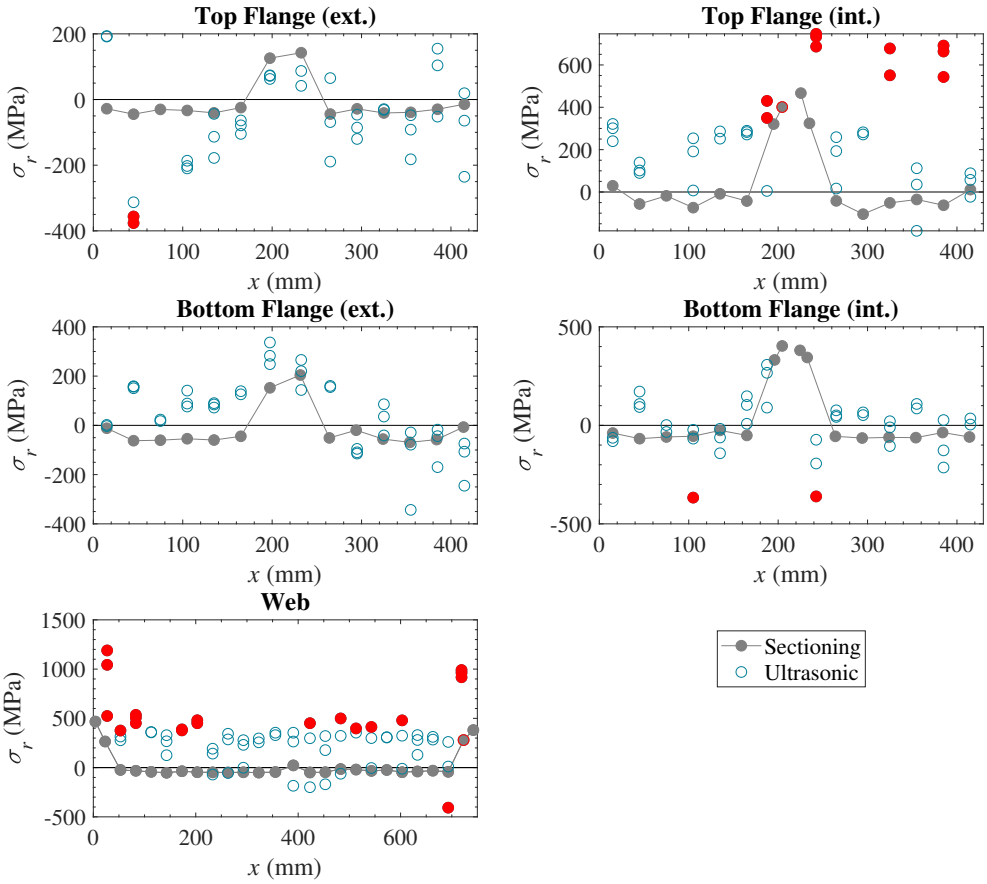

Figure 4.12: Comparison of ultrasonic and sectioning data for girder SP4 (using post-heat-treatment TOF–stress curves)

4.2.3.1 Web Measurements

Mean Stress Measured stresses in the web consistently exceed the yield stress, with the mean value for the entire plate exceeding yield stress in three of the four girders. A comparison of mean measured stress between the ultrasonic and sectioning methods is shown in Table 4.8.

Table 4.8: Mean stresses for web plates (ultrasonic (post-heat-treatment curves) and sectioning measured values)

Specimen	Mean stress	
	Ultrasonic (MPa)	Sectioning (MPa)
SP2-1	591	15
SP2-2	857	-18
SP3	399	6
SP4	316	-11

This large discrepancy may be due to the post-heat-treatment TOF–stress curve used for the web plates: the 10 and 13 mm thick calibration samples (i.e., those representing web plates) show a significant decrease in zero-stress TOF (TOF_0) following heat-treatment (see Figure 4.6). This may be be related to the removal of mill scale from the stress calibration samples prior to the post-heat-treatment tests.

While use of the post-heat-treatment curves is preferred due to lower residual stresses in the calibration samples, the lack of a consistent change in TOF from removal of mill scale (Section 4.2.1.1) and the larger variation in TOF_0 among the different thicknesses indicates that the post-heat-treatment curves are less reliable than those pre-heat-treatment. For this reason, the use of the pre-heat-treatment curve on web stress measurements is examined.

Agreement with sectioning results is improved if the pre-heat-treatment TOF–stress curves are used for the web. This is due to the higher TOF_0 value for the pre-heat-

treatment curves. The effect on the measured distribution for the web of SP3 is shown graphically in Figure 4.13 (values exceeding the base material yield stress are marked in red). Mean stress values for all girders when the pre-heat-treatment curves are used are summarized in Table 4.9.

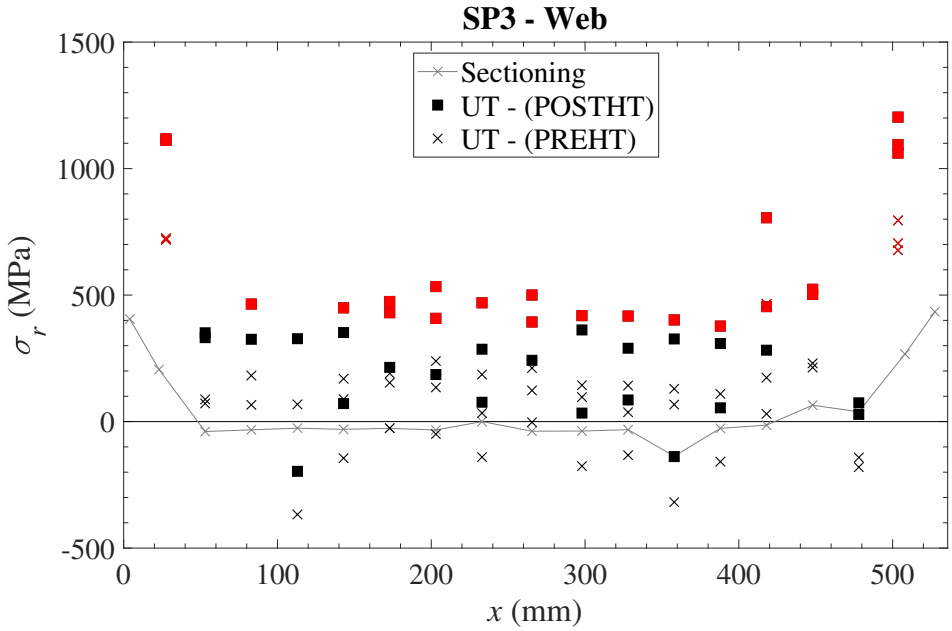

Figure 4.13: Effect of using post- vs. pre-heat-treatment curves on residual stress measurements for the web of SP3

Table 4.9: Mean stresses for web plates (ultrasonic (pre-heat-treatment curves) and sectioning measured values)

Specimen	Mean stress	
	Ultrasonic (MPa)	Sectioning (MPa)
SP2-1	287	15
SP2-2	508	-18
SP3	128	6
SP4	59	-11

Using the pre-heat-treatment curve value for $\Delta TOF/\Delta\sigma$ of 0.265 ns/MPa, the expected standard deviation of measured stresses due to rebonding of the probe is 75

MPa (using 20 ns as the TOF standard deviation; see Section 3.4.3). When the pre-heat-treatment curves are used, mean stress for SP4 is within one standard deviation of the sectioning value and SP3 within two standard deviations. SP2-1 and SP2-2 still show large errors, however. Each of these cases is examined separately.

SP2-1: Examining the distribution for the web of SP2-1, a series of large tensile readings are observed at the centre of the web. When the pre-heat-treatment curves are used, ultrasonic stress measurements appear to agree with the sectioning results (within the scatter inherent to the ultrasonic measurements) for the regions outside this area, despite the fact that the average stress for the entire plate is over-predicted. This is shown graphically in Figure 4.14. There appears to be a more localized issue with the set of measurements in the centre of the plate, rather than a systematic error affecting readings over the entire plate width.

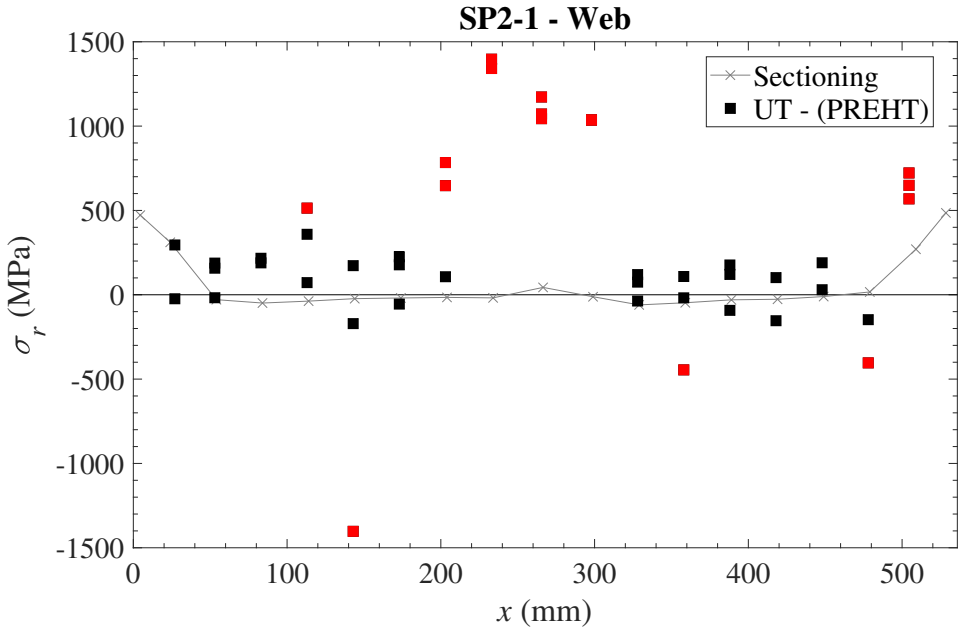

Figure 4.14: Sectioning and ultrasonic (pre-heat-treatment) stress measurements for the web of SP2-1

SP2-2: Mean measured stress still exceeds the yield stress, even when using the pre-heat-treatment TOF–stress curves. In this case, measurements taken on the reference

sample (RS1) before and after the measurements on the girder itself are examined. Values are shown in Table 4.10. It is noted that, while the mean RS1 values for the webs of SP2-1, SP3 and SP4 are all within 10 ns of one another, the mean RS1 readings for the web of SP2-2 are approximately 70 ns lower than all the other specimens. When a series of TOF measurements are corrected based on RS1 measurements at the start and end of measurement, an erroneous, low RS1 value will result in erroneous, high TOF values after corrections are applied (assuming the uncorrected TOF values are accurate). Thus, if some factor causes measurements on RS1 to decrease (without affecting the measurements on the girder), TOF values will be higher once RS1 corrections are applied and a more tensile stress reading will result. Using the post-heat-treatment $\Delta TOF/\Delta\sigma$ value for the 13 mm thick plate (0.265 ns/MPa), a 70 ns TOF change corresponds to a stress difference of 264 MPa. Decreasing the TOF readings for the web of SP2-2 by 70 ns to account for this error would improve agreement (though roughly a 250 MPa discrepancy would still exist).

Table 4.10: Mean RS1 values for measurements on webs of specimens

Specimen	Mean web RS1 reading (ns)
SP2-1	46346
SP2-2	46287
SP3	46354
SP4	46355

Peak Tensile Stress It is noted that even when using the pre-heat-treatment TOF–stress curves for the web, peak tensile stress at the edges of the web often exceeds the yield stress. This may be due to the particularly low $\Delta TOF/\Delta\sigma$ value from the stress calibration tests for the web plates (0.265 ns/MPa for the 13 mm sample, vs. 0.328 ns/MPa for the 32 mm sample). Further work should be done to assess this issue.

4.2.3.2 Flange Measurements

Mean Stress Mean stress values for a given plate surface in the flanges appear to be similar between the sectioning and ultrasonic measurements with the exception of the interior flange faces for SP2-2. Mean stresses on the exterior faces of the flanges for this girder show much better agreement with sectioning values—this seems to indicate a change in response due to surface effects (interior faces are sandblasted, while interior faces are not). Such a difference is not observed in any of the other test girders, however. Measured values on RS1 are also examined: the top flange interior (TFi) is measured during the same measurement session as the bottom flange exterior (BFe). The same is true for the bottom flange interior (BFi) and top flange exterior (TFe). RS1 values are compared for both pairs of data in Table 4.11. No significant difference is observed: RS1 readings are within 20 ns of one another in both cases. The cause of this error therefore remains unknown.

Table 4.11: Mean RS1 values for UT measurements on the flanges of SP2-2

Plate	Mean RS1 reading (ns)
BFi	46306
TFe	46324
Change	18
TFi	46303
BFe	46291
Change	-12

Discussion of the flanges up to this point has used the post-heat-treatment TOF–stress curves. While agreement in the webs is improved when pre-heat-treatment curves are used, that of the flanges is worsened, due to the lower TOF_0 value of the pre-heat-treatment curve for the 32 mm and 25 mm calibration samples. Although agreement is better for the flanges when using the post-heat-treatment curves, it is suggested

that the pre-heat-treatment curves be adopted for consistency, due to the effects of mill scale removal for the post-heat-treatment curve not being well understood.

Peak Tensile Stress Peak stress around the weld in the flanges is detected in the majority of cases; however, stress magnitudes show substantial variation and generally exceed the yield stress.

4.2.3.3 Initial Strip Measurements

In both the flanges and the web, it is observed that the first of the three measurements on any given strip is often found to be significantly different from the other two. This is shown for the web of girder SP4 in Figure 4.15. This is attributed to the lack of couplant on the surface prior to bonding of the probe for the first measurement on a given strip, resulting in different bond characteristics. To avoid this issue, it is suggested to bond and remove the probe prior to the first measurement on a strip.

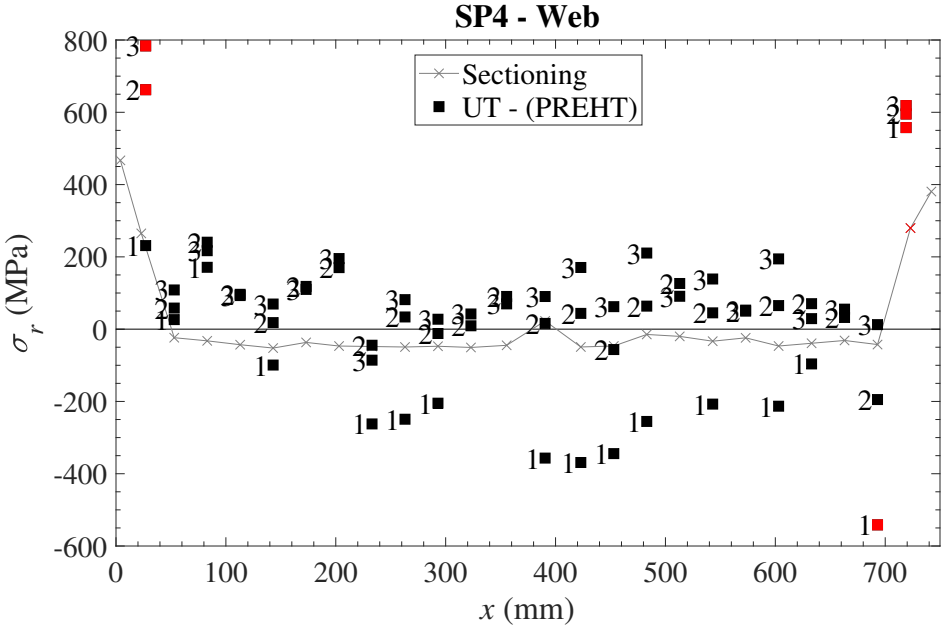

Figure 4.15: Measurement order for the web of SP4

4.3 Summary

Sectioning Residual stress measurements from the sectioning tests are presented and internal forces are summed to assess the accuracy of results. Accuracy is acceptable: the net force represents less than 10% of the associated total internal force for all girders. Measured stresses at the edges of the flanges are lower than values reported in the literature, likely due to the wider strips used in this study.

Ultrasonic Results from stress calibration tests before and after heat-treatment of calibration samples is presented. Values for the acoustoelastic constant are found to be lower than those reported by Santos et al. (2004) for API Grade 5L X70 steel. This is attributed to differences in material properties among the two grades. The acoustoelastic constant is also found to decrease with plate thickness. This is thought to be due to variation of the second- and third-order elastic constants between thicknesses; however, it is not possible draw further conclusions as only Young's modulus was directly measured.

A temperature calibration test is also carried out: a linear relationship between TOF and surface temperature with a slope of 24 ns/°C is observed. This value is used to correct measured TOF values for surface temperature.

A consistent change in TOF readings is observed between the spring pressure and clamped conditions of the probe. Because a clamp is used for stress calibration tests, while a spring is used for measurements on the girders, TOF–stress curves are adjusted to account for this change.

Systematic errors in ultrasonic stress measurements on the test girders are found to be primarily due to issues with the TOF–stress calibration curves. TOF_0 values for the post-heat-treatment curves show a large degree of scatter and are thus considered

less reliable than those of the pre-heat-treatment curves. Mean stress readings for the web often exceed the yield stress; use of the pre-heat-treatment TOF–stress curves helps to alleviate this problem, though peak stress readings at the edges of the web still exceed the yield stress. Agreement with sectioning values in the flanges is closer when the post-heat-treatment curves are used; however, such usage is perhaps not justifiable given the lack of understanding of the effects of mill scale removal. Stress peaks around the weld in the flanges and web are detected in the majority of cases, though measured stress magnitude almost always exceeds the yield stress.

Scatter in the data greater than that inherent to rebonding of the probe is thought to be due to difference in surface texture between the interior and exterior plate faces (interior are sandblasted) and slippage of the housing assembly. Additional surface preparation and a housing assembly in which acrylic wedges are securely attached together could reduce such errors.

Chapter 5

Predictive Residual Stress Models

Four prominent residual stress models are examined: predicted distributions are compared to those measured in order to assess the accuracy of each model and its potential for broad use in residual stress prediction. The most suitable model is then used as a starting point for proposing a residual stress model for modern welded girders.

5.1 Assessment of Residual Stress Models

5.1.1 Parameters for Assessment

In order to quantify model accuracy, several parameters are defined for a given measured residual stress distribution such that a direct comparison can be made between measured and model distributions. A measured residual stress distribution in a given plate (flange or web) is represented by a series of stress values, σ_r, with corresponding locations along the width of the plate, x_r. x_r is measured from the left side of the flanges and the top of the web. If stresses are measured on both faces of a plate, σ_r is

taken as the average through-thickness stress at each x_r. Tensile stresses are positive and compressive stresses negative.

Residual stress distributions in welded I-sections are characterized by two broad types of regions:

- Regions of relatively constant compressive stress away from the welds and flange edges.
- Regions of high stress gradient (HSG) around the flange-web welds and flange edges (if heat-cutting is used).

These regions are shown in Figure 5.1 for a typical measured residual stress distribution in a flange plate. In a web plate, two weld HSG regions are located at the plate edges and the compressive region covers the remaining width. Parameters are proposed in order to characterize the compressive regions and the HSG region around the weld in both flange and web plates.

Parametric Compressive Stress Compressive stress in the regions away from the welds and flange edges is chosen as the first parameter for a measured residual stress distribution. Compressive stress is chosen over tensile stress around the welds for its greater consistency: since a high stress gradient is present around the weld, measured stresses are more sensitive to measurement location and exhibit much more variation than compressive stresses. Compressive stresses also cover a larger portion of each plate than tensile stresses around the welds, allowing for a greater degree of confidence in mean values due to the larger number of measured points. Furthermore, based on the findings of Nethercot (1974), compressive residual stresses in the flanges (in particular the compression flange) have a greater impact on lateral–torsional buckling (LTB) capacity compared to tensile residual stresses around the weld. Compressive

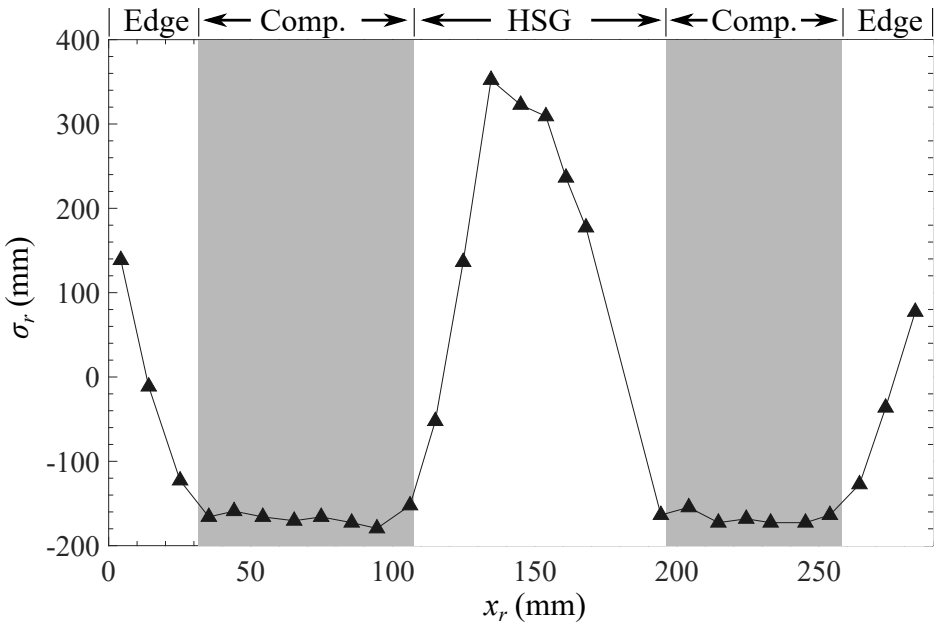

Figure 5.1: Characteristic regions in a measured flange residual stress distribution (compressive, high-stress-gradient and edge regions)

regions in the flanges are further from the minor axis and thus contribute more to the weak-axis moment of inertia than the tensile regions near the welds.

The parametric compressive stress, σ_{Pc}, for a set of measured residual stresses on a plate, σ_r, is calculated using Equation 5.1.

$$\sigma_{Pc} = mean(\sigma_{rc}) \tag{5.1}$$

where σ_{rc} is defined as:

$$\sigma_{rc} = \sigma_r \,\forall\, \sigma_r < mean(\sigma_r) - 0.25std(\sigma_r) \tag{5.2}$$

Such a condition is used instead of simply taking the mean of all negative values of σ_r in order to capture stresses only within the regions of relatively constant stress. Figure

5.2 shows in red the points σ_{rc} considered in calculating the parametric compressive stress for a measured stress distribution from the flange of a specimen in the literature. It can be seen that several points in the HSG regions represent negative stresses. Using Equation 5.1 ensures such points are not included in the calculation of σ_{Pc}.

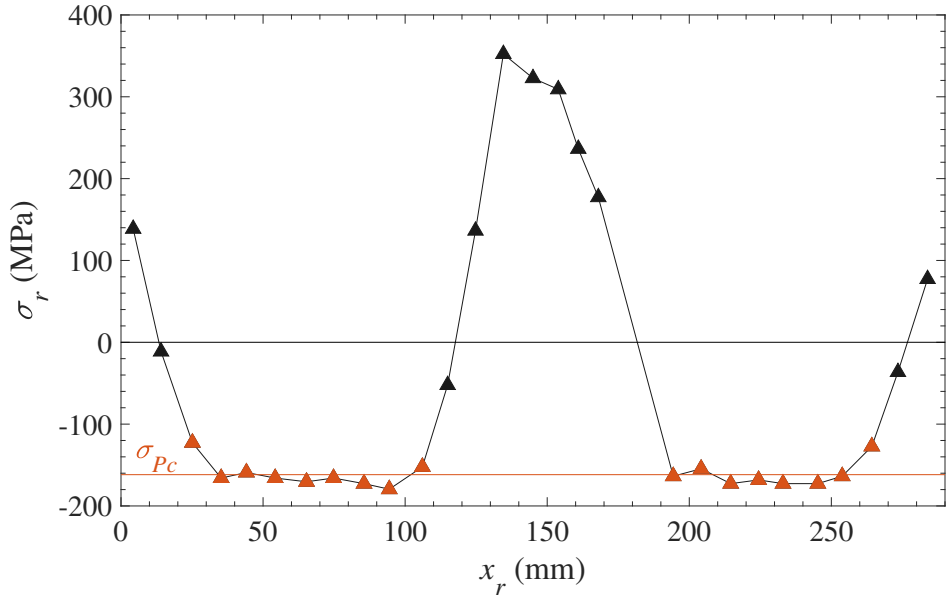

Figure 5.2: Points considered for calculation of parametric compressive stress (top flange of specimen R14-460 (Ban et al. 2013))

Parametric compressive stress for the flanges and web are defined as σ_{Pcf} and σ_{Pcw}, respectively. When calculating σ_{Pcf}, the average value of σ_{Pc} for the top and bottom flanges is used.

Parametric HSG Region Width The HSG width that defines the region immediately adjacent to the weld in which a sharp stress gradient is observed is selected as the parametric HSG width (as the stresses in the HSG regions at the edges of the flanges are highly dependent upon the method used for plate cutting and other variables, it is treated separately and discussed in Section 5.2.1.3). This HSG region differs from the tensile region around the weld in that the HSG region can include compressive regions at the edges. A comparison of the HSG region width (η_f) and

tensile region width (η_{Tf}) in the top flange of one specimen is shown in Figure 5.3. Note that η_{Tf} accounts for only 75% of η_f. Distinction is made between the two regions to facilitate assessment of measured distributions: the tensile region width does not accurately represent the width of the stress spike at the centre of the flanges induced by welding.

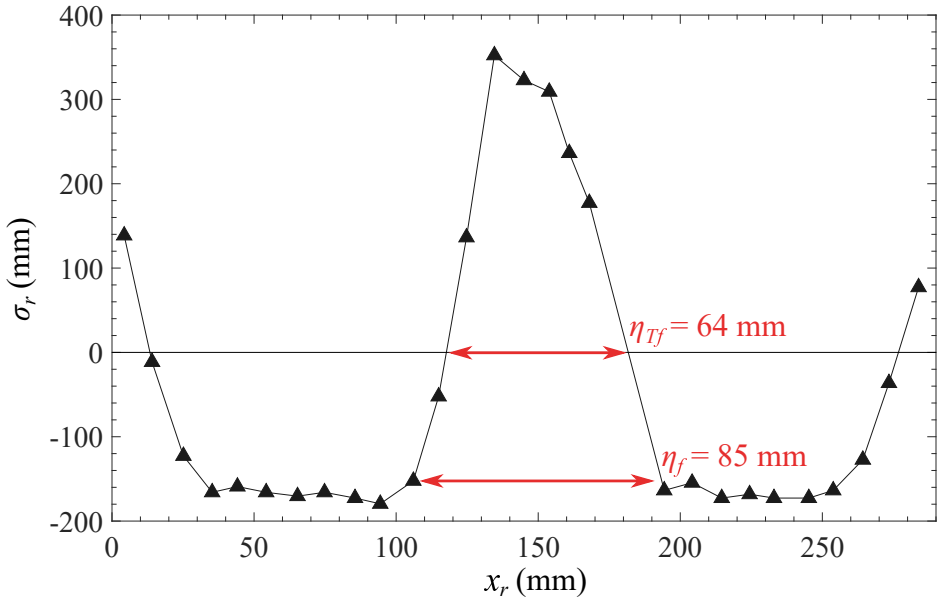

Figure 5.3: HSG region width vs. tensile region width (top flange of specimen R14-460 (Ban et al. 2013))

The parametric HSG region width for the flanges is defined as:

$$\eta_f = x_{2f} - x_{1f} \tag{5.3}$$

where x_{1f} and x_{2f} are the locations on the left and right half of the flange, respectively, that are closest to the flange centre for which σ_r is equal to $\sigma_{P\eta}$ (given by Equation 5.4).

$$\sigma_{P\eta} = mean(\sigma_{rc}) + 1.5std(\sigma_{rc}) \tag{5.4}$$

The 1.5 standard deviations of σ_{rc} is added to the mean value σ_{rc} in the calculation of $\sigma_{P\eta}$ in order to ensure x_{1f} and x_{2f} are located at the edges of the HSG region (not within the constant compressive stress region). When comparing against model predictions, the value of η_f for a given specimen is taken as the average of the values for the top and bottom flanges.

The parametric HSG region width for the web is defined as:

$$\eta_w = \frac{x_{1w} + (h - x_{2w})}{2} \tag{5.5}$$

where x_{1w} and x_{2w} are the locations on the web that are closest to the top and bottom of the web, respectively, for which σ_r is equal to $\sigma_{P\eta}$.

If there are no measured points in the stress distribution exactly equal to $\sigma_{P\eta}$, values for the bounds of the HSG region (x_{1f}, x_{2f}, x_{1w} and x_{2w}) are calculated using linear interpolation between the two measured points with stresses immediately above and below $\sigma_{P\eta}$.

Acceptable Accuracy for Parameter Prediction Because compressive stress in the flanges (and in particular in the compression flange) is a primary factor influencing LTB capacity, flange parametric compressive stress is adopted as the primary parameter by which model accuracy is assessed (HSG width is assessed as an intermediate parameter to aid in the prediction of compressive stress magnitude). Predictions of compressive stress are considered accurate if they fall within one standard deviation of σ_{rc} for a given measured distribution.

5.1.2 Model Comparisons

Values for parametric compressive stress and HSG region width for the measured distributions of all four girders are compared to those predicted by the following models:

- Chernenko and Kennedy (1991) model for flame-cut plates (abbreviated as 'C&K (FC)')
- Best-fit Prawel (Kim 2010)
- BSK model (2003)
- Dwight and Moxham (1969) model based on weld area (abbreviated as 'D&M')

It should be noted that exact values are not reported for the Chernenko and Kennedy distribution. Approximate values are therefore used based on schematic graphs and reported upper-bound stress values (Chernenko and Kennedy 1991). Comparisons of each model with the measured residual stress distributions are shown in Appendix B.

Flanges A comparison of model predictions of the parametric HSG region width in the flanges is shown in Figure 5.4. The BSK model offers the closest prediction, followed by the Dwight and Moxham and Chernenko and Kennedy models. The Best-fit Prawel model significantly over-predicts HSG width for wider flanges; prediction is better for narrower flanges (e.g., SP3).

Parametric compressive stress magnitude predictions for the flanges are compared in Figure 5.5. Mean values for the measured distributions are shown with error bars indicating one standard deviation of σ_{rc} above and below the mean. In both the Chernenko and Kennedy and Best-fit Prawel models, compressive stress is simply a

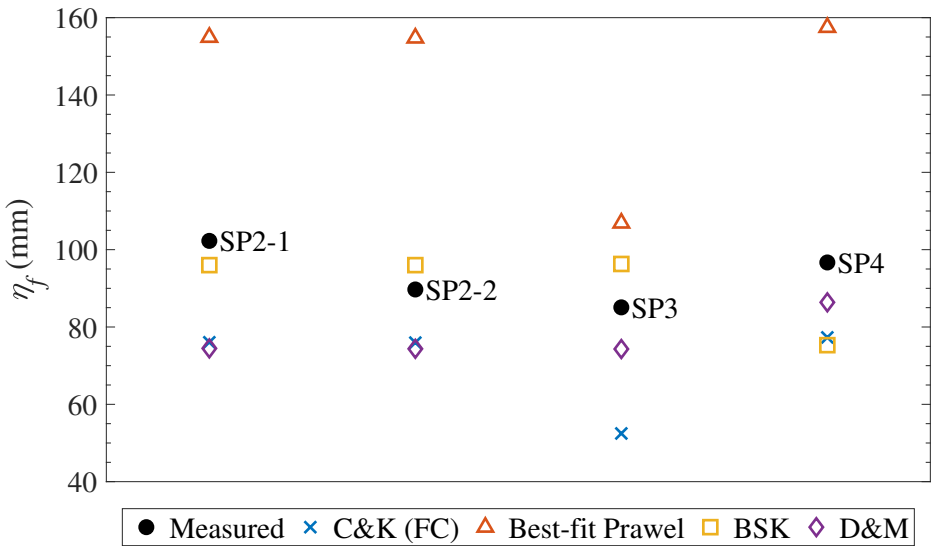

Figure 5.4: Flange parametric HSG region width of measured and model stress distributions

constant fraction of yield stress. As such, predicted compressive stress values are similar among the four specimens. Both the BSK and Dwight and Moxham models, however, show a marked increase in compressive stress magnitude for SP3 (which has a narrower flange compared to the other specimens). This is because compressive stress is calculated using equilibrium of the plate for these two models, based on the width of the HSG region. Because predicted values of η_f are similar for all specimens, predicted compressive stresses are therefore higher in SP3. The BSK and Dwight and Moxham models are thus more sensitive to section geometry and predict increasingly large compressive stress magnitudes for sections with narrower flanges, with all other parameters being held constant.

Of the two models that use a constant fraction of yield stress for compressive stress magnitude (that is, those of Chernenko and Kennedy and the Best-fit Prawel), the Best-fit Prawel model better predicts the parametric compressive stress of the measured distributions, despite significantly over-predicting the parametric HSG region width. This is attributed to the lower predicted tensile residual stress magnitude in the Best-fit Prawel model: tensile residual stress magnitude is $0.5\sigma_y$, whereas the

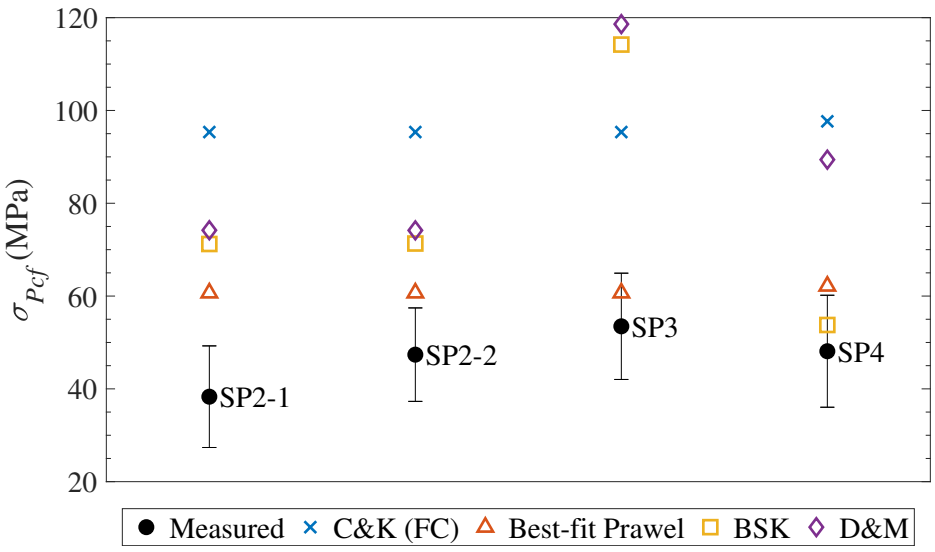

Figure 5.5: Flange parametric compressive stress of measured and model stress distributions

Chernenko and Kennedy model uses $1.0\sigma_y$. Despite the accuracy of the prediction of parametric compressive stress magnitude, however, the Best-fit Prawel model is not considered for use in the proposal of a residual stress model for two reasons related specifically to flange residual stresses (further discussion regarding web stresses follows):

1. The model is based on data from milled plates and exhibits larger compressive stresses at the edges of the flanges, not the constant compressive stress with tensile region at the edges of the flanges typical of heat-cut plate sections. This difference is expected to have a significant effect on buckling capacity due to the large contribution of the edges of the flanges to the weak-axis moment of inertia.

2. The inaccuracy of HSG region width predictions suggests that the model is potentially inaccurate for varying geometries. When residual stress data on column–type sections from a study by Yang et al. (2018) are compared to the Best-fit Prawel model,

parametric compressive stress magnitude in the flanges is under-predicted by almost 50% (roughly 75 MPa)(Figure 5.6).

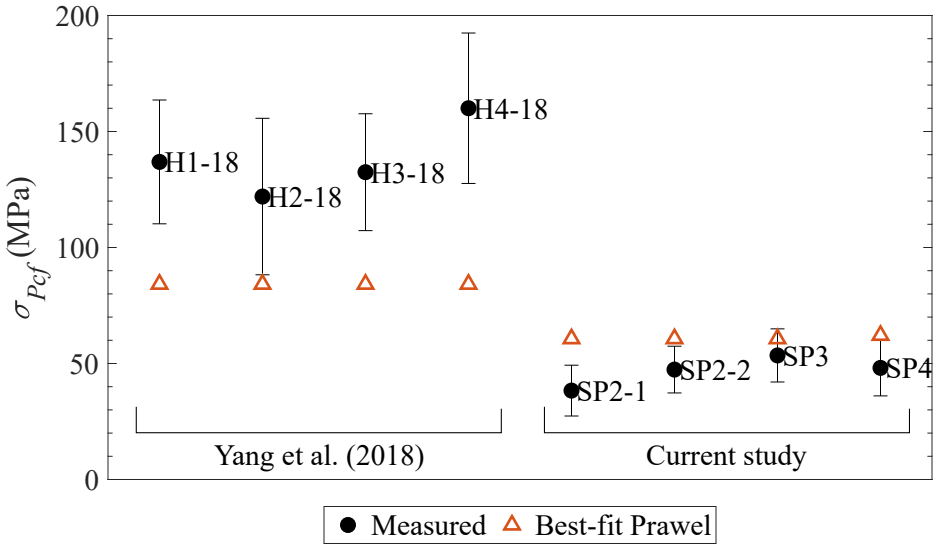

Figure 5.6: Flange parametric compressive stress prediction of Best-fit Prawel model for specimens measured in this study and those measured by Yang et al. (2018)

Web Predictions of parametric HSG region width and compressive stress magnitude in the web are shown in Figures 5.7 and 5.8, respectively. Predictions for η_w are poor for all models. The lower value for SP4 (which has a deeper web then the other three girders) is not predicted—all models predict a larger η_w for SP4. Despite this, the BSK and Dwight and Moxham models both predict σ_{Pcw} to within one standard deviation in three out of four girders and the Best-fit Prawel in two out of four. The Chernenko and Kennedy model consistently over-predicts σ_{Pcw} by a large margin.

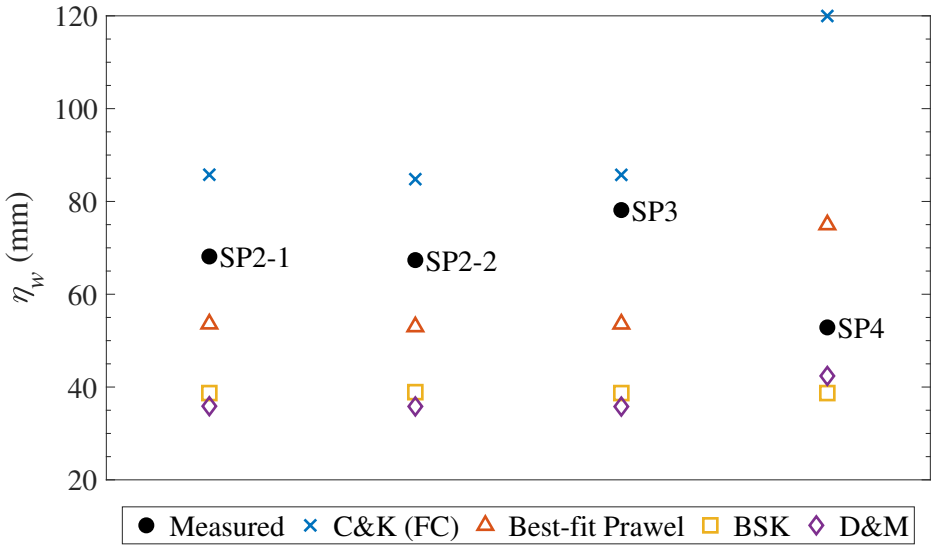

Figure 5.7: Web parametric HSG region width of measured and model distributions

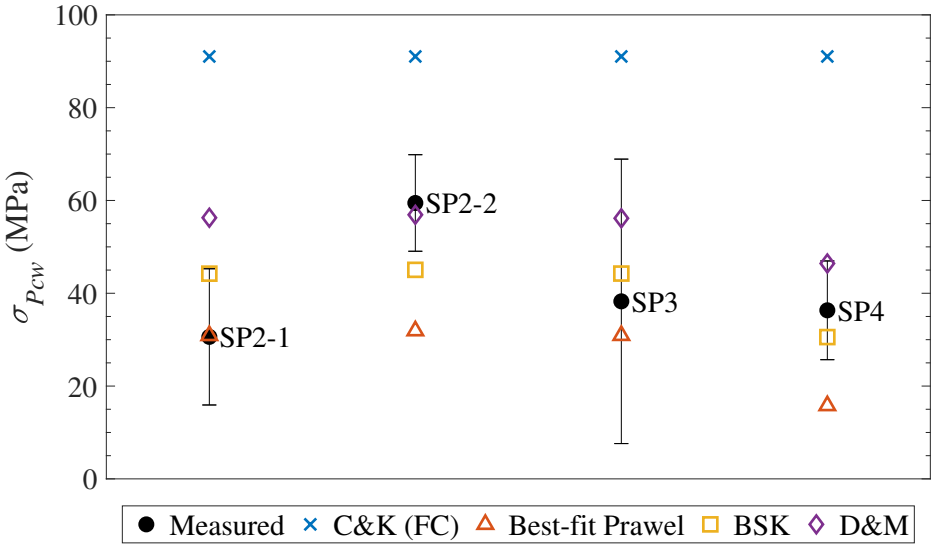

Figure 5.8: Web parametric compressive stress from measured and model distributions

5.2 Proposed Residual Stress Model

5.2.1 Model for Modern North American Girders

The Dwight and Moxham (1969) model based on weld area is used as the starting point for proposing a predictive model for residual stresses in modern welded I-sections. This model is selected for two reasons:

- The model already predicts the parametric width of the HSG region of the flanges for the measured distributions with reasonable accuracy (accuracy in the flanges is more critical for LTB predictions).
- Despite being the oldest of the four models examined, the Dwight and Moxham model is the only model with a thermo-mechanical derivation (albeit semi-empirical); all other models are purely empirical. This more rigorous basis allows for physical justifications of modifications made to the model. Several such modifications are made in order to achieve a more accurate prediction of the residual stress distribution over the cross-section.

The model proposed by Dwight and Moxham (1969) when applied to welded I-sections is summarized in Figure 5.9.

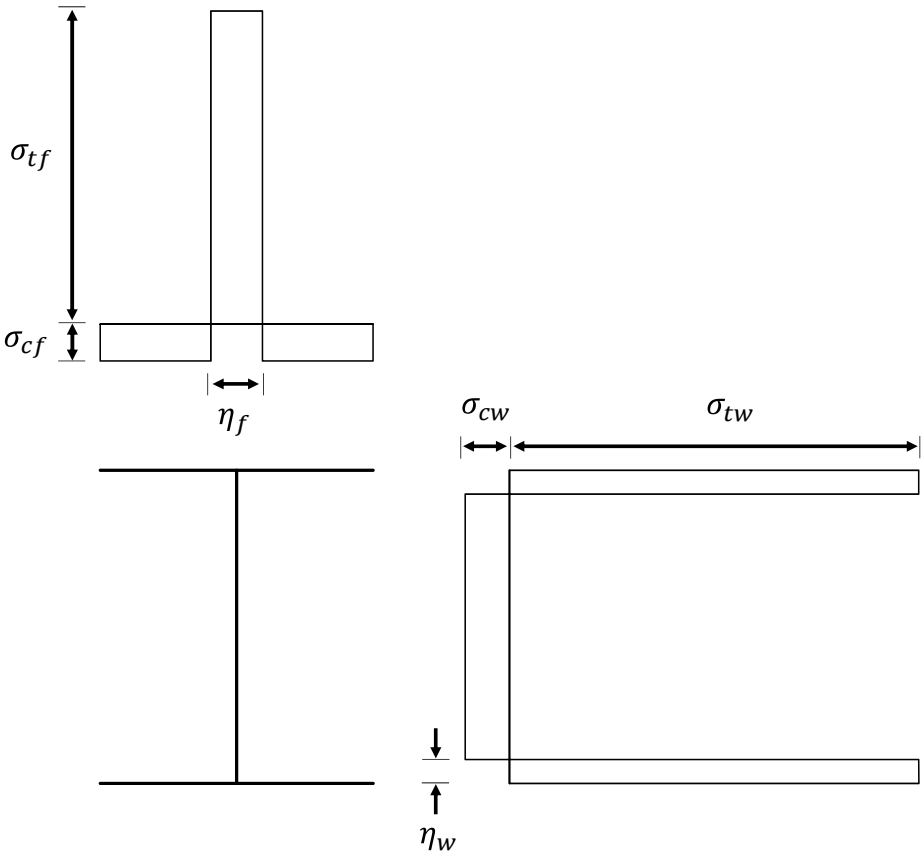

Figure 5.9: Dwight and Moxham (1969) model for welded I-sections

Model parameters are defined as:

$$\begin{aligned} \sigma_{tf} &= \sigma_{yf} \\ \sigma_{tw} &= \sigma_{yw} \\ \sigma_{cf}, \sigma_{cw} &= \text{calculated using equilibrium of each plate} \\ \eta_f &= 2\left(\frac{CA_w}{\sigma_{yf}\Sigma t}\right) + w \end{aligned} \tag{5.6}$$

$$\eta_w = \frac{CA_w}{\sigma_{yw}\Sigma t} \tag{5.7}$$

where:

A_w = cross-sectional area of a single weld (mm^2)

σ_{yf}, σ_{yw} = base metal yield stress of the flanges and web, respectively (MPa)

Σt = sum of thicknesses of web and one flange (mm)

w = web thickness (mm)

with C defined as:

$$C = \frac{96E\alpha}{16 \times 10^{-3}} \tag{5.8}$$

where:

E = Young's modulus (MPa)

α = coefficient of linear thermal expansion ($^{\circ}C^{-1}$)

The value for α is taken as 15 $\times 10^{-6}$ $^{\circ}C^{-1}$. The web thickness is included in the equation for η_f to account for the separation of the two welds on the flange by the web (based on the recommendations of Kamtekar (1974))

The following are examined in order to propose improvements to the existing model:

- HSG region shape
- Plate vs. section equilibrium
- Flange edge regions
- Effect of flange width on HSG region width
- Measured vs. nominal weld size

5.2.1.1 HSG Region Shape

While the parametric width of the HSG region in the flanges is reasonably well predicted by the Dwight and Moxham model, parametric compressive stress magnitude is significantly over-predicted. This is attributed to the over-prediction of total tensile force around the weld region: stress is set at σ_{yf} for the entire width of the HSG region. A comparison with the measured distributions shows this to be inaccurate. From the measured stress data it appears that the tensile stresses around the weld are better approximated using a triangular distribution (Figure 5.10). In order to modify the shape of the HSG region, a small modification of the region width is necessary, however.

The width of the HSG, η_f, defined by Dwight and Moxham is shown in Equation 5.6. This equation represents a simplification—the HSG region actually begins further from the weld centre-line (see Section 2.2.4). In order to produce a better representation of theoretical width, the coefficient in Equation 5.8 is modified from 96 to 128. Figure 5.10 shows the effect of these modifications for SP2-2 (with flame-cut plates). The effect on the prediction of parametric compressive stress is summarized for all four tested specimens in Figures 5.11 and 5.12, for the flanges and web, respectively.

Implementation of a triangular HSG region improves the accuracy of parametric compressive stress prediction in the flanges for all specimens, while resulting in an underprediction in the web. Because the influence of residual stresses on LTB is less in the web than the flanges, however, the modifications are adopted for the proposed model.

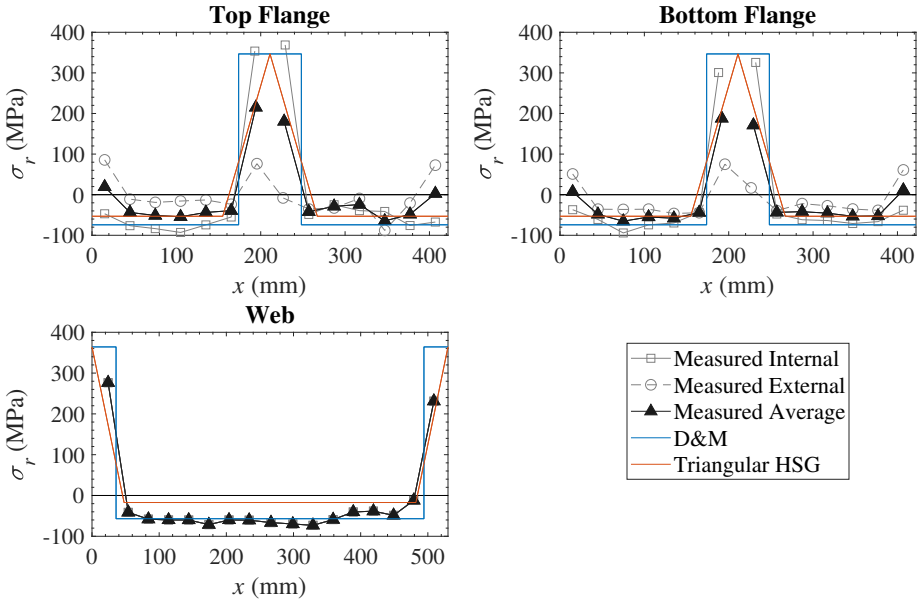

Figure 5.10: Comparison of existing Dwight and Moxham model and triangular HSG modification for girder SP2-2

It should be noted that when the tensile stress distribution is triangular, calculation of compressive stress is modified. The general equation for calculation of compressive stress magnitude is:

$$\sigma_c = \frac{F_T}{A_C} \tag{5.9}$$

where F_T is the total force on the regions with tensile stresses and A_C is the area of the plate subjected to compression. For a rectangular distribution (taking the flange parameter—equations are similar for the web), these are defined as:

$$F_{Tf} = \eta_f t_f \sigma_{yf} \tag{5.10}$$

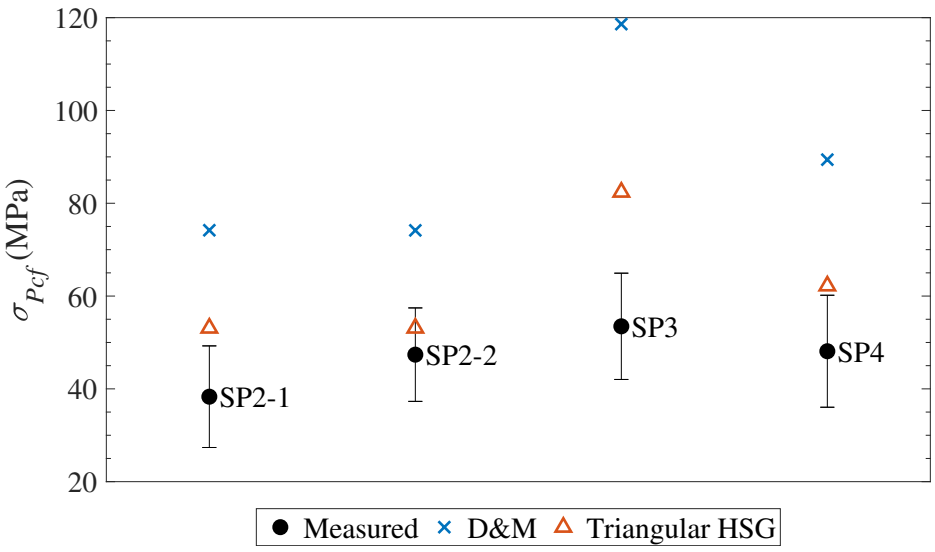

Figure 5.11: Effect of using triangular HSG region on prediction of flange parametric compressive stress

$$A_{Cf} = (b - \eta_f)t_f \tag{5.11}$$

For a triangular distribution,

$$F_{Tf} = \frac{1}{2}\eta_{Tf}t_f\sigma_{yf} \tag{5.12}$$

$$A_{Cf} = \left[b - \left(\frac{\eta_{Tf} + \eta_f}{2}\right)\right]t_f \tag{5.13}$$

where η_{Tf} is the width of the tensile region, defined as:

$$\eta_{Tf} = \frac{\sigma_{yf}}{\sigma_{yf} + \sigma_c}\eta_f \tag{5.14}$$

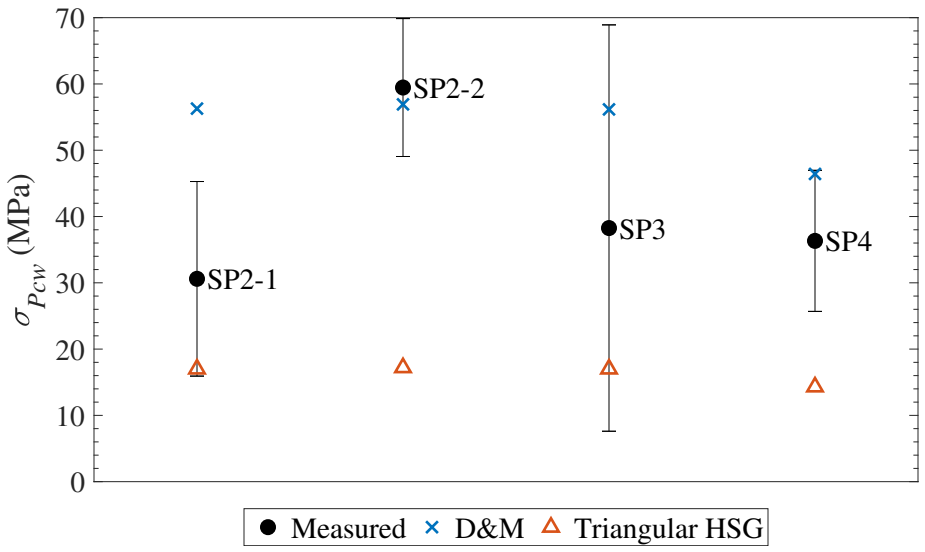

Figure 5.12: Effect of using triangular HSG region on prediction of web parametric compressive stress

Because η_{Tf} is dependent on σ_c, an implicit solution is required. While an exact solution is mathematically possible, σ_c is solved for numerically in this study for simplicity.

5.2.1.2 Plate vs. Section Equilibrium

It is observed that even with the triangular tensile region, parametric compressive stresses are still over-predicted in the flanges yet under-predicted in the web. Such a trend indicates interaction of the plates within the section: each individual plate is not necessarily in equilibrium. It is thus more appropriate to calculate compressive stresses by considering equilibrium of the entire cross-section instead of equilibrium of each individual plate. In order to use section equilibrium, however, a relationship between flange and web compressive stresses must be established. Flange and web parametric compressive stress magnitudes are plotted against one another in Figure 5.13. Compressive stresses are found to be larger in the flanges than the web for all the plasma-cut specimens (SP2-1, SP3, SP4), while stresses are larger in the web for

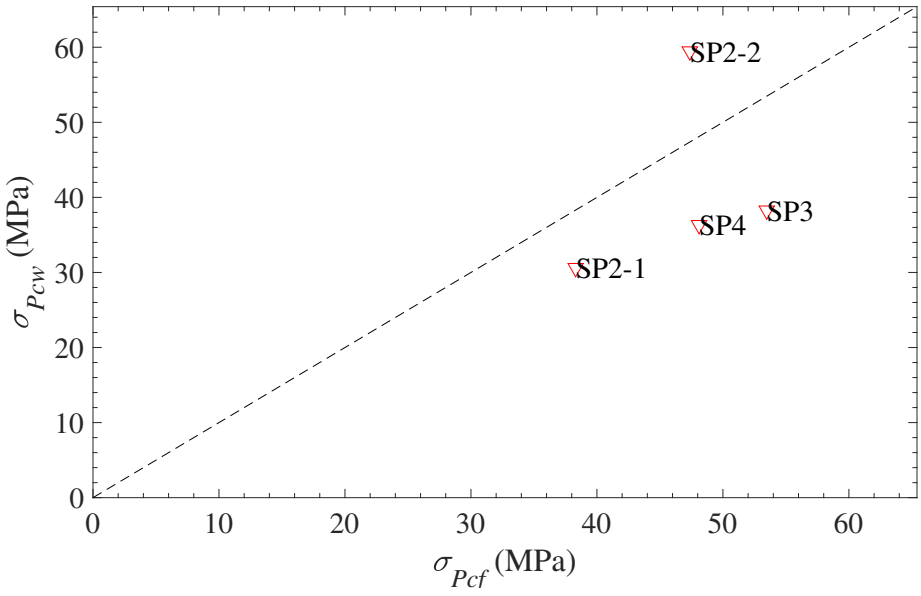

Figure 5.13: Parametric compressive stress magnitude in flanges vs. web

the flame-cut specimen (SP2-2), likely because of larger induced tensile stresses from flame-cutting the edges. For the purposes of this study, flange and web compressive stresses are assumed to be equal. As more girders are measured, the validity of this assumption and differences between the plasma- and flame-cut specimens should be investigated further.

The difference in predicted compressive stress magnitudes using plate and section equilibrium is shown in Figures 5.14 and 5.15 for the flanges and the web, respectively (note that σ_{Pcf} and σ_{Pcw} are equal when applying section equilibrium). Prediction of parametric compressive stress is improved for both the flanges and the web (and particularly so for the flanges) when section equilibrium is used. Section equilibrium is therefore adopted for the proposed model.

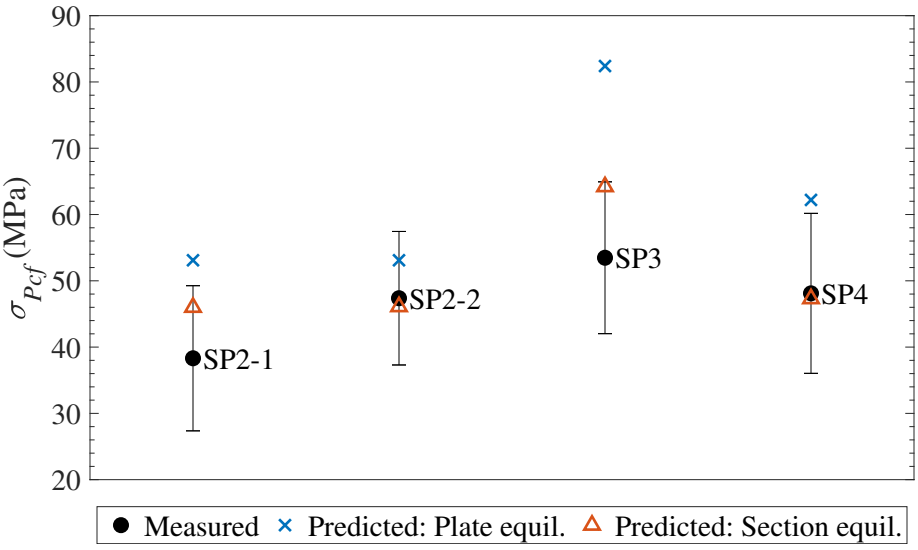

Figure 5.14: Effect of using plate vs. section equilibrium on prediction of flange parametric compressive stress (triangular HSG region)

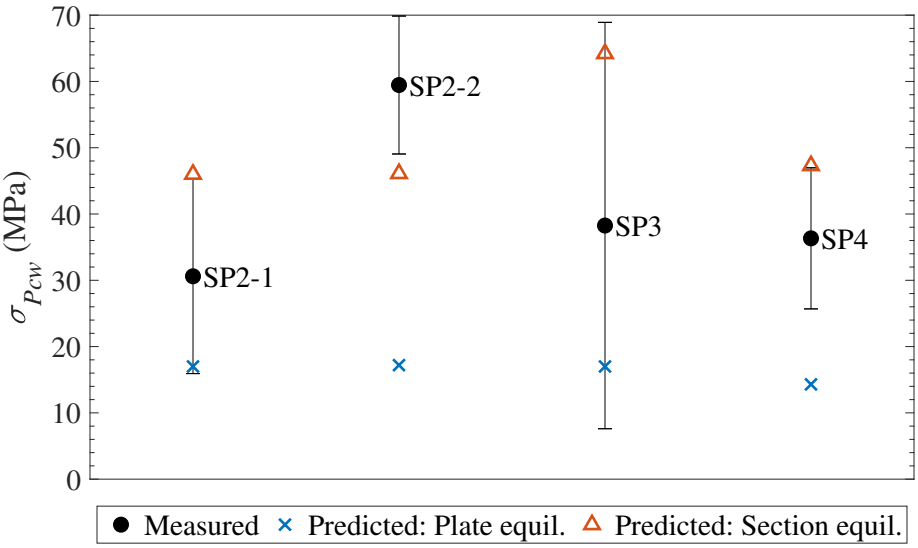

Figure 5.15: Effect of using plate vs. section equilibrium on prediction of web parametric compressive stress (triangular HSG region)

5.2.1.3 Flange Edge Regions

Dwight and Moxham's model assumes constant compressive stress outside the HSG region. This is not accurate for sections comprising flame- or plasma-cut plates: stresses in the regions near the edges of the flanges tend to be less compressive than

those further from the edge, or tensile. Because yielding of the flange edges during loading in flexure has the greatest effect on effective weak-axis moment of inertia, accurate prediction of residual stresses at the flange edges is essential to ensuring accurate LTB capacity predictions. To this end, both edge region width and stress magnitude are examined.

Edge Region Width Edge regions do not appear to extend beyond one strip width for any of the specimens in this research program. Edge region width is thus taken as $b/14$ (one strip width in the wider flange specimens), as finer resolution is not possible with the data at hand. Width is taken to be a fraction of plate width, as opposed to an absolute value, in order to avoid overlap with the HSG region for narrow flanges.

Edge Stress Magnitude Measured edge stress magnitudes for the specimens in this research are presented in Table 5.1. Average edge stress magnitude (including all four flange edge values for each section) is observed to be 16 MPa in compression for the plasma-cut specimens and 10 MPa in tension for the flame-cut specimen. While edge stresses in the flame-cut specimen do appear to be significantly more tensile than those in the plasma-cut specimens (standard deviation among the mean values for all of the plasma-cut specimens is 8 MPa), an edge stress value of zero is chosen to be implemented into the model regardless of plate cutting method for simplicity, as all edge stress magnitudes represent less than 10% of the yield stress. The edge region is assumed to have a triangular stress distribution.

In order to implement edge regions into the predictive stress model, modifications are made to the calculation of compressive stress magnitude; this is done by reducing the effective area in compression. When using section equilibrium, compressive stress is calculated by dividing total tensile force, F_T, from the tensile regions around the welds by the cross-sectional area in compression, A_C (Equation 5.15). Using section

Table 5.1: Flange edge stresses for measured specimens

Specimen	Edge stress mean (MPa)	Edge stress st. dev. (MPa)
SP2-1	-23	15
SP2-2	10	7
SP3	-10	-8
SP4	-15	16

equilibrium without edge regions (i.e., the constant compressive stress extends to the flange edges):

$$\sigma_c = \frac{F_T}{A_C} \tag{5.15}$$

where:

$$F_T = 2F_{Tf} + F_{Tw} = 2\left(\frac{1}{2}\eta_{Tf}t_f\sigma_{yf}\right) + \left(2\frac{1}{2}\eta_{Tw}w\sigma_{yw}\right) \tag{5.16}$$

$$A_C = 2A_{Cf} + A_{Cw} = 2\left[b - \left(\frac{\eta_{Tf} + \eta_f}{2}\right)\right]t_f + \left[h - 2\left(\frac{\eta_{Tw} + \eta_w}{2}\right)\right]w \tag{5.17}$$

where η_{Tf} and η_{Tw} are the widths of the tensile region in the flanges and web, respectively, defined as:

$$\eta_{Tf} = \frac{\sigma_{yf}}{\sigma_{yf} + \sigma_c}\eta_f \tag{5.18}$$

$$\eta_{Tw} = \frac{\sigma_{yw}}{\sigma_{yw} + \sigma_c}\eta_w \tag{5.19}$$

Equation 5.15 is modified to Equation 5.20 when edge regions are implemented:

$$\sigma_c = \frac{F_T}{A_C - 4\left(\frac{1}{2}\eta_{fe}t_f\right)} \tag{5.20}$$

where:

η_f, η_w = HSG widths in the flange and web, respectively
η_{fe} = edge region width in the flanges
σ_{yf}, σ_{yw} = yield stress in the flanges and web, respectively
b = flange width
h = web height
t_f = flange thickness
w = web thickness

5.2.1.4 Effect of Flange Width on Flange HSG Region Width

From Figure 5.14, a larger discrepancy between measured and predicted flange compressive stress values (when using plate equilibrium) is noted for SP3 when compared to the rest of the specimens (SP2-1, SP2-2, SP4). SP3 has a nominal flange width of 300 mm, while all the other specimens have a nominal width of 420 mm.

Everything else held constant, the model predicts a significant increase in compressive stress as flange width narrows due to the smaller width of the compression region without a corresponding reduction in the tensile force. Such a trend is not observed in the measured distributions. SP2-1 and SP3 are nominally identical except for flange

width and can be used to examine the effect of flange width on flange parametric compressive stress: values in these two specimens are within one standard deviation of one another (see Figure 5.14). It is noted that Dwight and Moxham's model is derived for an infinitely wide plate and the width of the HSG region is expected to decrease with plate width (Dwight and Moxham 1969). While it is difficult to assess the difference in width of the HSG region between SP2-1 and SP3 directly (due to the use of 30 mm strips around the weld), the lack of such a severe change in compressive stress between the two specimens may be indicative of a reduction in HSG width with decreasing flange width.

Due to the limited range of flange widths investigated in this study, additional data from the literature are examined to assess the trend of HSG width over a wider range of flange widths. An equation is proposed to decrease HSG region width as flange width decreases (see Section 5.2.2.1 for details):

$$\eta_f = \eta \left(1 - \frac{B}{b}\right) \tag{5.21}$$

where η is taken as η_f from Equation 5.6, b is the flange width and B is an empirically determined coefficient. A B value of 53 is found to minimize the square of the errors for parametric compressive stress when considering the specimens in this study. The effect of adding this factor on flange and web parametric compressive stresses is shown in Figures 5.16 and 5.17, respectively. Predictions of parametric compressive stress are now within one standard deviation of the measured values for all four girders, with the exception of the web of SP2-2. Because of the lesser impact of web compressive stress on LTB, however, the model is deemed acceptable.

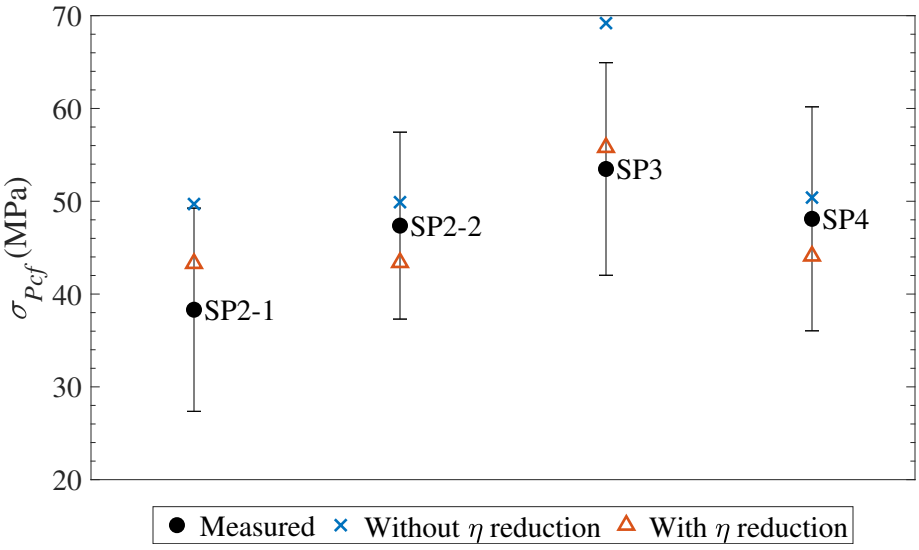

Figure 5.16: Effect of applying reduction factor to flange HSG region width on prediction of flange parametric compressive stress ($B = 53$)

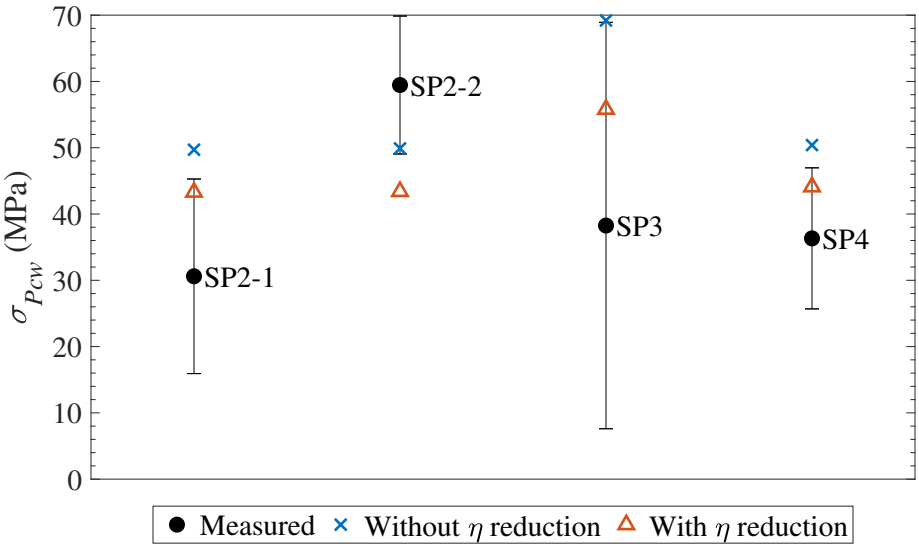

Figure 5.17: Effect of applying reduction factor to flange HSG region width on prediction of web parametric compressive stress ($B = 53$)

5.2.1.5 Measured vs. Nominal Weld Size

The foregoing discussion used nominal fillet weld size (8 mm) for all specimens. Measured sizes, however, are slightly larger than 8 mm (see Table 3.4). The effect of using measured instead of nominal weld size in the model is examined: parametric

compressive stress prediction is compared with the measured stress distribution for both nominal and measured weld sizes in Figure 5.18.

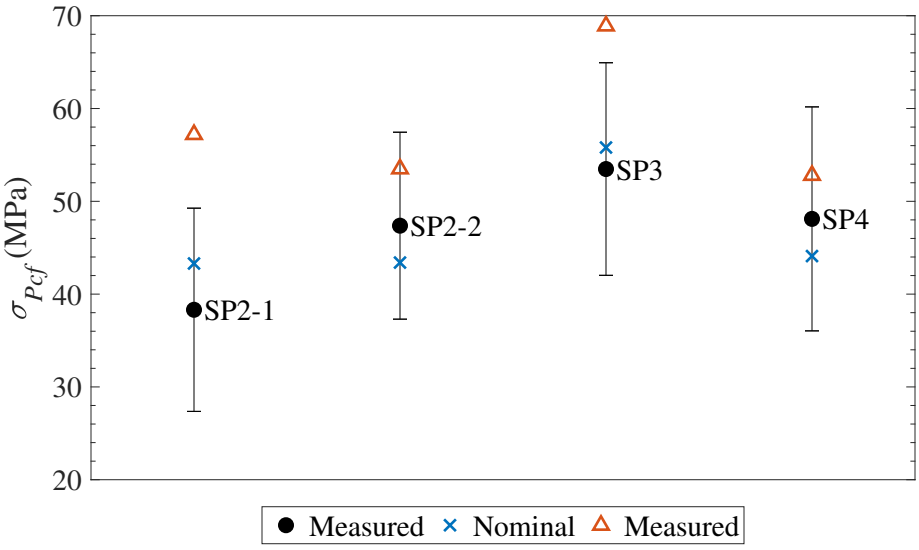

Figure 5.18: Effect of using nominal vs. measured weld size on prediction of flange parametric compressive stress

Compressive stress predictions are worsened by the using the measured weld size. It is therefore decided to continue using the nominal fillet size of 8 mm for the model.

5.2.1.6 Proposed model

Figure 5.19 outlines the proposed model based on the specimens tested in this study.

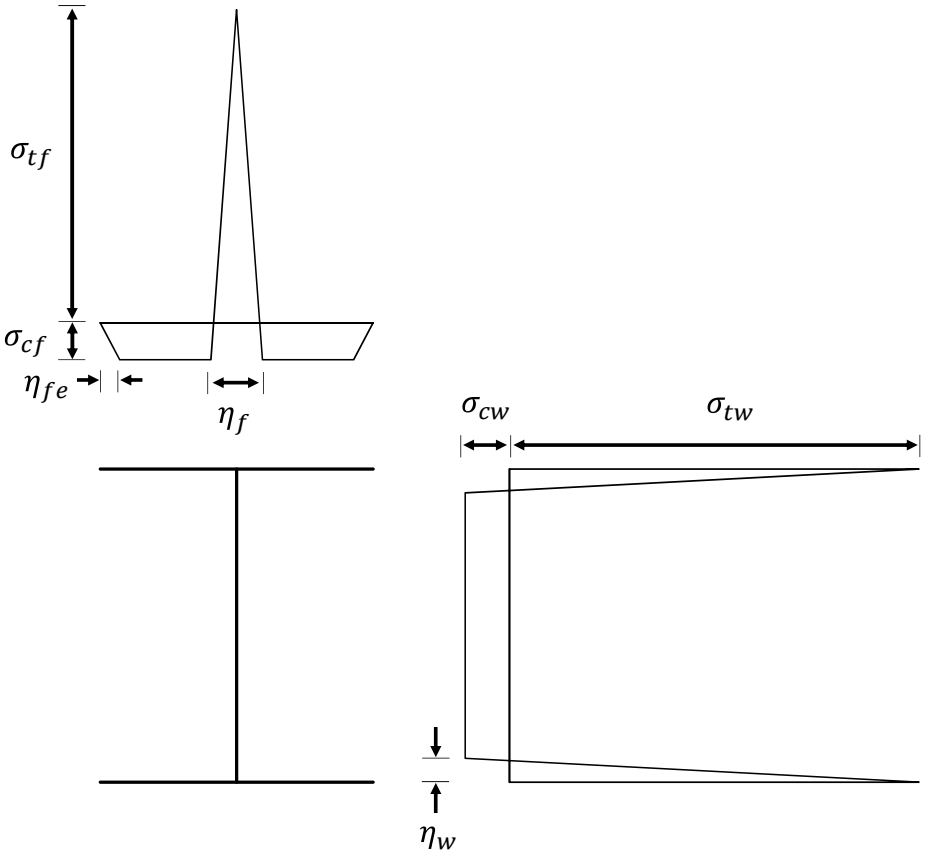

Figure 5.19: Proposed model

where:

$$\sigma_{tf} = \sigma_{yf}$$

$$\sigma_{tw} = \sigma_{yw}$$

$$\sigma_{cf} = \sigma_{cw} = \text{calculated from equilibrium of the section}$$

$$\eta_f = \left(2\frac{CA_w}{\sigma_{yf}\Sigma t} + w\right)\left(1 - \frac{B}{b}\right) \tag{5.22}$$

$$\eta_w = \frac{CA_w}{\sigma_{yw}\Sigma t} \tag{5.23}$$

$$\eta_{fe} = b/14 \tag{5.24}$$

where B is an empirical coefficient equal to 53 (examined further in Section 5.2.2), and C is defined as:

$$C = \frac{128E\alpha}{16 \times 10^{-3}} \tag{5.25}$$

A comparison of the model in Figure 5.19 with the measured distributions is shown in Appendix B.

5.2.2 Comparison with Literature Data

In order to examine the wider applicability of the model to a range of section geometries, a comparison with additional data from the literature is conducted. The following criteria are used to select specimens from the literature:

- Data are less than ten years old
- Section is welded using fillet welds
- Plates are heat-cut

A full list of specimens examined is provided in Appendix A. It should be noted that exact values for the residual stresses in the literature are not reported; distributions used are based on image processing of stress distribution graphs. The model proposed in Section 5.2.1.6 is examined in the subsequent discussion.

5.2.2.1 HSG Region Width

As is observed for the specimens measured in this study, the HSG width tends to be over-predicted as flange width narrows. This problem is particularly acute for specimen H4-18 from the study by Yang et al. (2018), for which the combination of narrow flanges and large weld size results in an over-prediction of flange parametric compressive stress by almost 200% (exceeding the yield stress, see Figure 5.22). From Figure 5.20 it appears the HSG region width is not constant with respect to flange width, but tends to decrease as flanges narrow. Dwight and Moxham predict such a trend: the model was derived for infinitely wide plates and will increasingly over-predict HSG region widths as plate width narrows.

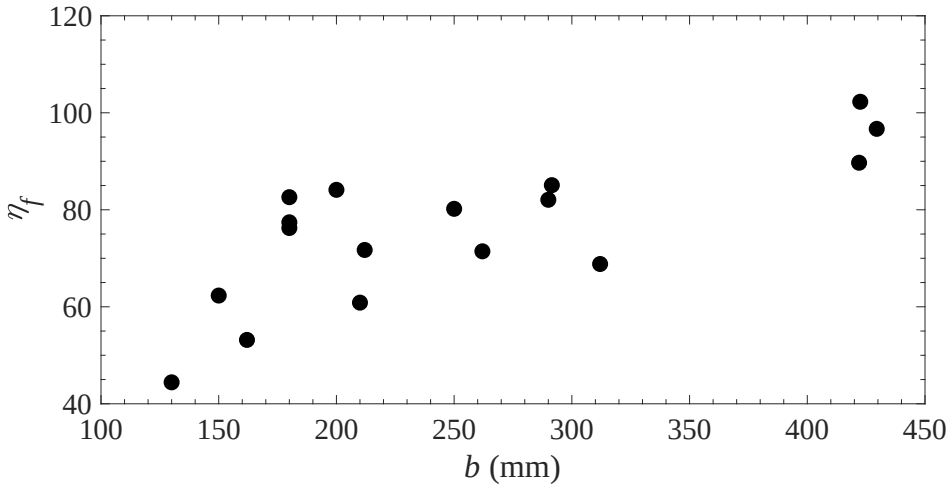

Figure 5.20: Flange parametric HSG width vs. flange width (from measured distributions)(Ban et al. 2013)(Yang et al. 2016)(Yang et al. 2018)

Equation 5.21 reflects the trend observed in Figure 5.20: a sharp increase is seen initially as flanges widen, with values begin to plateau as the flange width increases further. An analysis is done to determine the value of the coefficient B that minimizes the square of the errors for parametric compressive stress in the flanges. An investigation of the full set of specimens considered (including those measured in this study) revealed a B value of 69.

Equation 5.21 is only valid for $b > B$, as the $(1 - \frac{B}{b})$ term will be negative when $b < B$. Sensitivity of compressive stress to η_f increases as flange width decreases; the equation is therefore not recommended for flange widths less than 130 mm, as this is the narrowest flange from the literature examined. Because the value of $(1 - \frac{B}{b})$ approaches unity as b tends to infinity, and because compressive stress sensitivity to η_f decreases for wider flanges, no upper bound for the use of Equation 5.21 is specified for b.

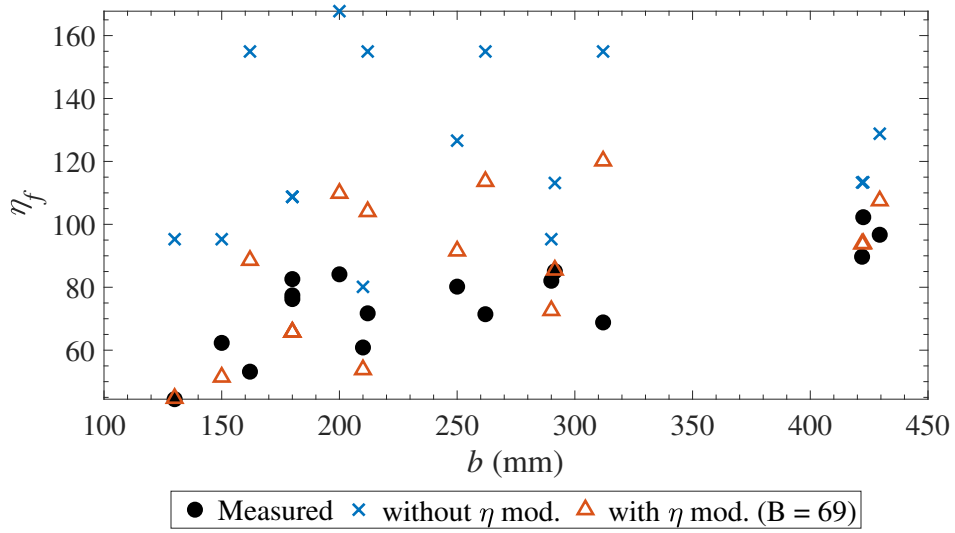

Figure 5.21: Flange parametric HSG region width vs. flange width: effect of η reduction factor ($B = 69$)(Ban et al. 2013)(Yang et al. 2016)(Yang et al. 2018)

Predictions of HSG region width with and without the reduction factor are shown in Figure 5.21. Much better agreement is observed after applying the reduction factor. The effect of the reduction becomes most apparent when examining the flange parametric compressive stress magnitude prediction: the trend of increasingly large over-predictions as flange width decreases is lessened significantly (Figure 5.22).

While reductions in predicted compressive stress may also be achieved by simply lowering the magnitude of the peak tensile stress, implementing such a reduction in HSG region width is deemed a more suitable approach for improving flange compressive stress predictions for several reasons. Over-predictions in compressive stress tend to

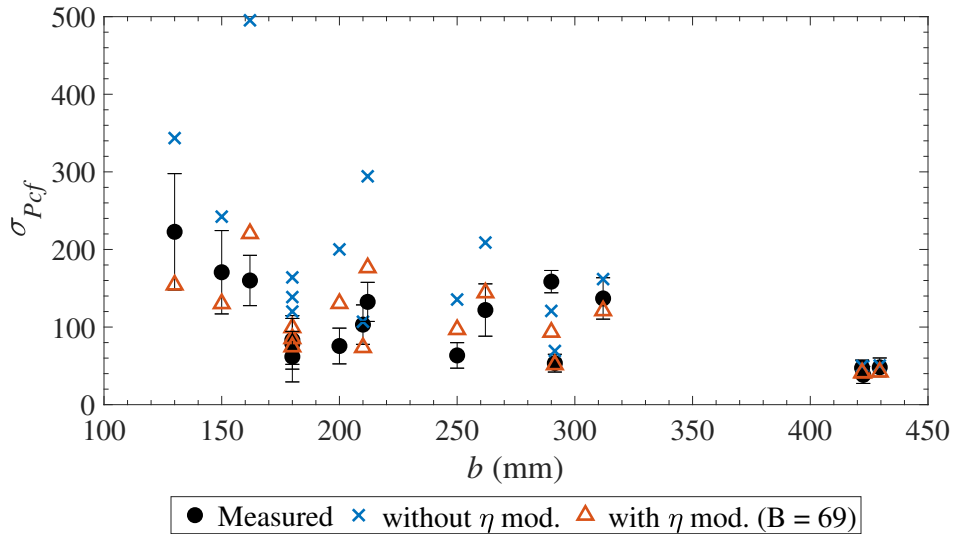

Figure 5.22: Flange parametric compressive stress vs. flange width: effect of η reduction factor ($B = 69$)(Ban et al. 2013)(Yang et al. 2016)(Yang et al. 2018)

be larger for sections with narrower flanges, such that reducing tensile stress (and consequently compressive stress) by a constant fraction would result in under-predictions for sections with wider flanges. Additionally, peak tensile stress at the weld is not measured in the majority of studies due to the inability to access the portion of the flange covered by the fillet welds (where peak tensile stress is expected to occur).

5.2.2.2 Effect of Plate Thickness

It is observed that even with the implementation of the η reduction factor, parametric compressive stress is still over-predicted by up to 75%. The exact reason for this is unclear; however, it is noted that many of the specimens examined possess relatively thin flange plates (10 - 16 mm). Because the focus of this study is on welded girders—which are primarily fabricated from heavier flange plates—preference is given to specimens with thicker flanges (i.e., those measured by Yang et al. (2018)).

For this reason, the optimum value for the coefficient B in Equation 5.21 is reassessed using only specimens with thicker flanges, including flange thicknesses ranging from

25 to 32 mm. The value for B that minimizes error for the parametric compressive stress is found to be 90. The B value found when considering only the specimens measured in this study is 53. The effect of using B values of 53, 69 and 90 on predictions of σ_{Pcf} for the thick-flanged specimens is shown in Figure 5.23.

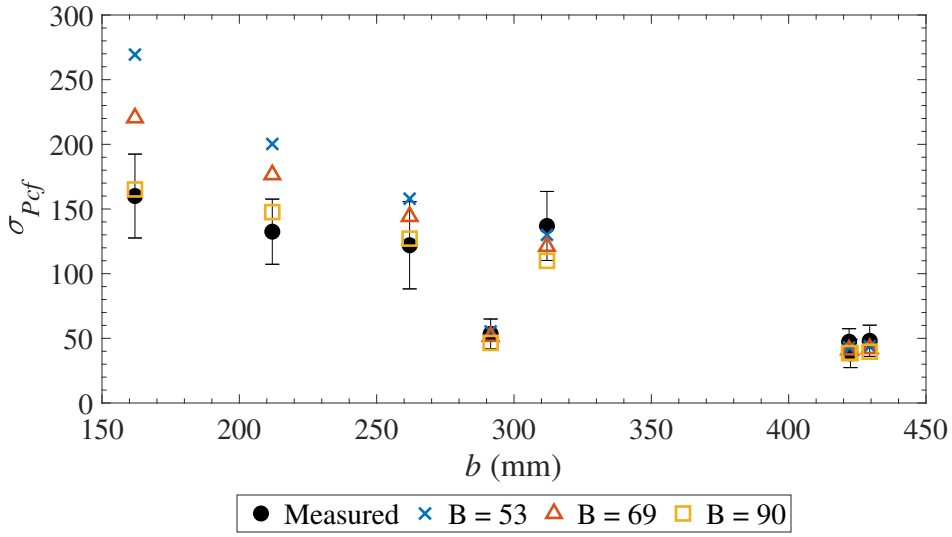

Figure 5.23: Flange parametric compressive stresses vs. flange width for different B values (only specimens with $t_f \geq 25$ mm)(Yang et al. 2018)

It can be seen that while B values of 53 and 69 both significantly over-predict σ_{Pcf} for specimens with narrower flanges, predictions are within one standard deviation when a B value of 90 is used. Because sensitivity of σ_{Pcf} to η_f is much lower for the specimens measured in this study, with wider flanges, than to those measured by Yang et al. (2018), a value of 90 is preferred over 53. Use of a B value of 90 instead of 53 improves predictions of flange parametric compressive stress for the Yang et al. specimens significantly, while only minimally changing predictions for the specimens measured in this study.

5.2.2.3 Edge Regions

Many of the specimens examined in the literature possess much higher tensile residual stresses at the edges of the flanges compared to those examined in the current study. This may be due to the use of narrower strips in the specimens from the literature, enabling smaller regions of peak stress to be detected. For this reason, it is difficult to draw a direct comparison between specimens measured in this study and those in the literature. The edge regions as proposed in Section 5.2.1.3 are therefore retained; this offers a reasonable prediction of region width for the literature specimens, though edge stress magnitude is under-predicted for specimens from the literature.

5.2.2.4 Summary

When applying the model proposed in Section 5.2.1.6 to the selected specimens from the literature, modification of the coefficient B in the HSG region width reduction factor is deemed to be required. Examining specimens with 25 mm thick flanges or greater, including those from the current study, the value of B that minimizes compressive stress errors is found to be 90. Specimens with thinner flanges are not considered, as welded girders typically comprise thicker flange plates. Because the minimum flange width of the specimens examined is 130 mm, use of the HSG region reduction factor for flanges narrower than 130 mm is not recommended without further verification.

5.3 Summary

Proposed Residual Stress Model Because none of the existing residual stress models examined provide sufficiently accurate predictions of stresses in the test specimens, a new model is proposed based on sectioning data from the girders, along with data from several other studies in the literature. The model is based on that proposed by Dwight and Moxham (1969), with the following modifications:

1. The tensile stress peak around the weld is changed to a triangular distribution.
2. Compressive stress magnitude is equal in the flanges and web, and is calculated using equilibrium of the entire section (the original model considers equilibrium of each individual plate).
3. An edge region is introduced, with a triangular stress distribution, to reflect the effect of cutting the flanges with heat.
4. A reduction factor is proposed to reduce the width of the HSG region around the weld as flanges narrow.

Regarding item 4, while a B value of 53 in Equation 5.21 is found to minimize error in the prediction of flange parametric compressive stress for the specimens measured in this study, a value of 90 is recommended. With this adjustment predictions for specimens of Yang et al. (2018) are improved significantly, while only minimally affecting predictions for the specimens in this study.

Comparisons of the proposed model (Figure 5.19) with the measured distributions from this study and those from Yang et al. (2018) are shown in Figures 5.24 to 5.31. Comparisons of the existing models are shown in Appendix B. The proposed model provides a more accurate prediction of residual stresses than the four existing models examined, particularly in the flanges.

The one exception to this is the predicted distribution in the web of specimen H4-18 (Figure 5.31). It should be noted, however, that this specimen has a very shallow web (120 mm). Such sections would typically be produced by rolling, not welding; the inaccuracy of the model for such geometries is thus not a cause for significant concern.

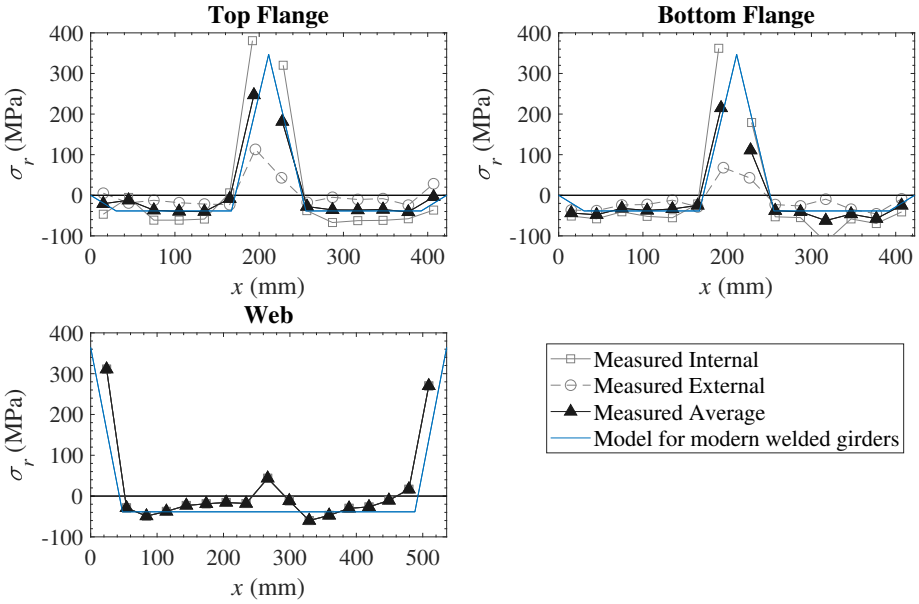

Figure 5.24: Comparison of proposed model ($B = 90$) with measured residual stress distribution for girder SP2-1

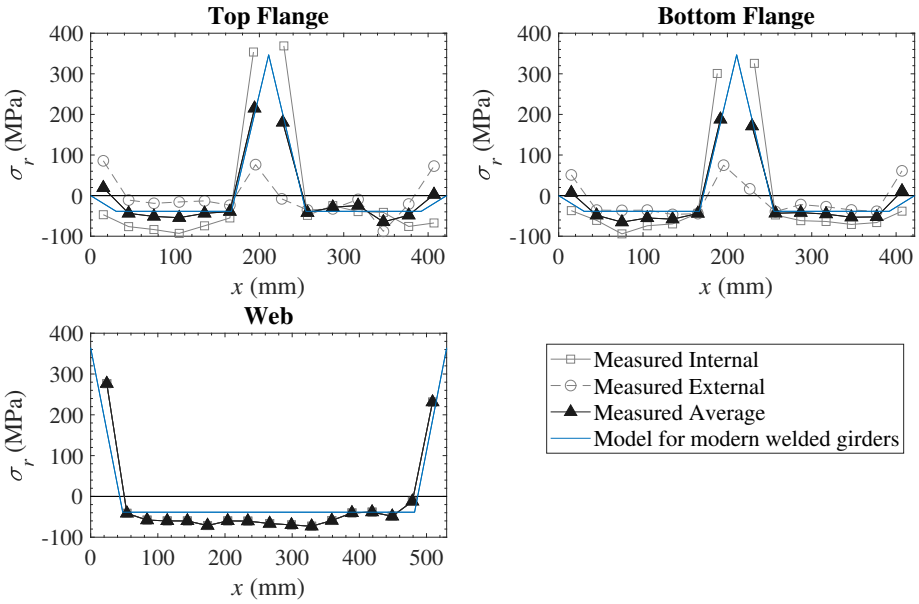

Figure 5.25: Comparison of proposed model($B = 90$) with measured residual stress distribution for girder SP2-2

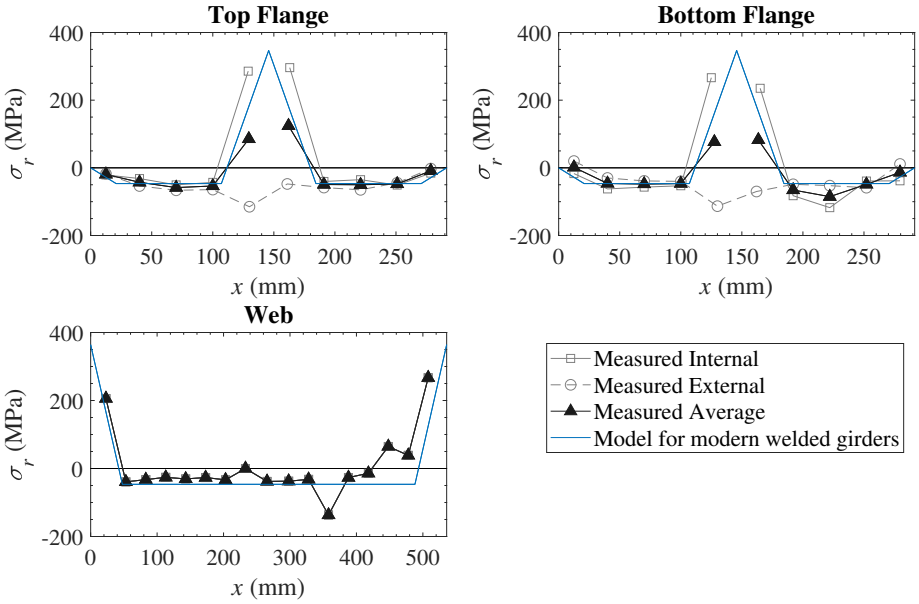

Figure 5.26: Comparison of proposed model ($B = 90$) with measured residual stress distribution for girder SP3

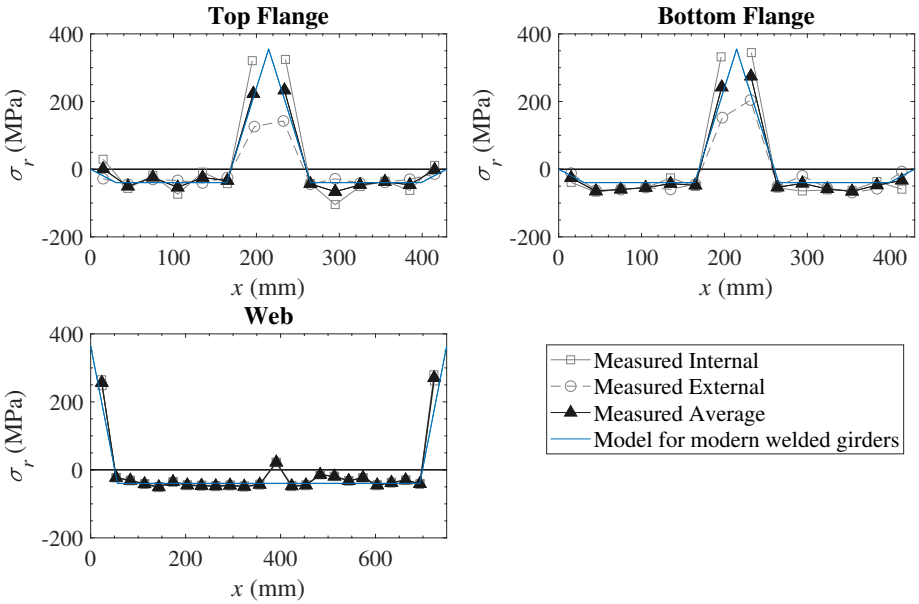

Figure 5.27: Comparison of proposed model ($B = 90$) with measured residual stress distribution for girder SP4

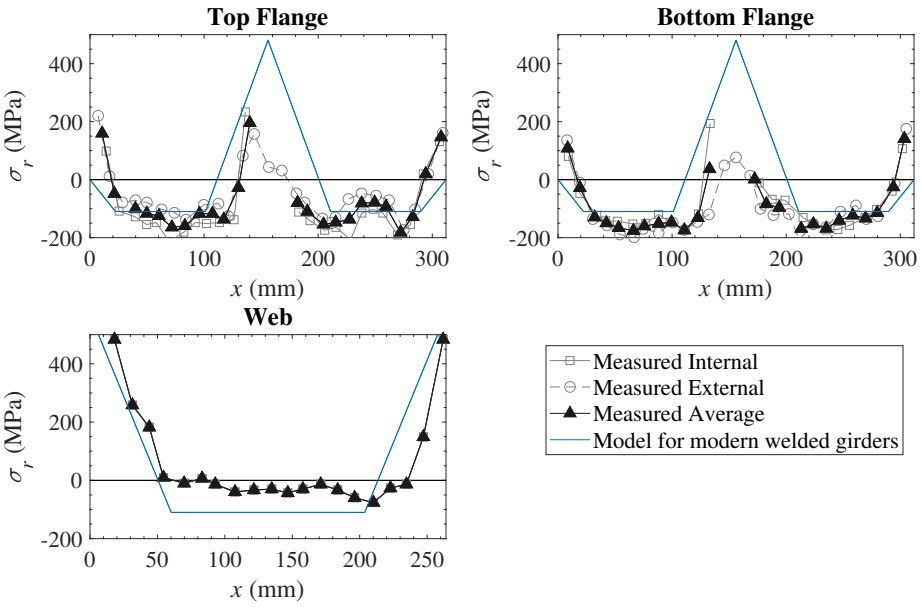

Figure 5.28: Comparison of proposed model ($B = 90$) with measured residual stress distribution for specimen H1-18 (Yang et al. 2018)

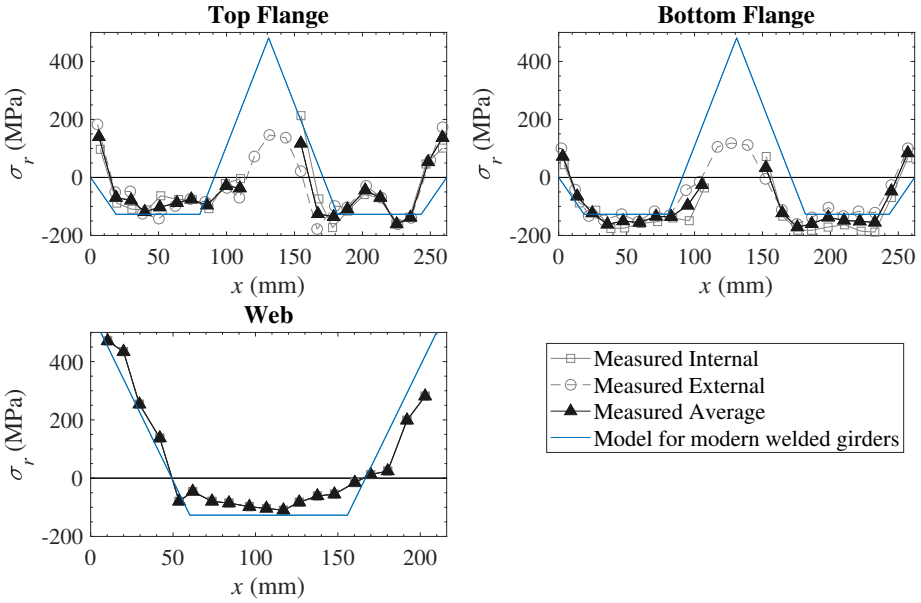

Figure 5.29: Comparison of proposed model ($B = 90$) with measured residual stress distribution for specimen H2-18 (Yang et al. 2018)

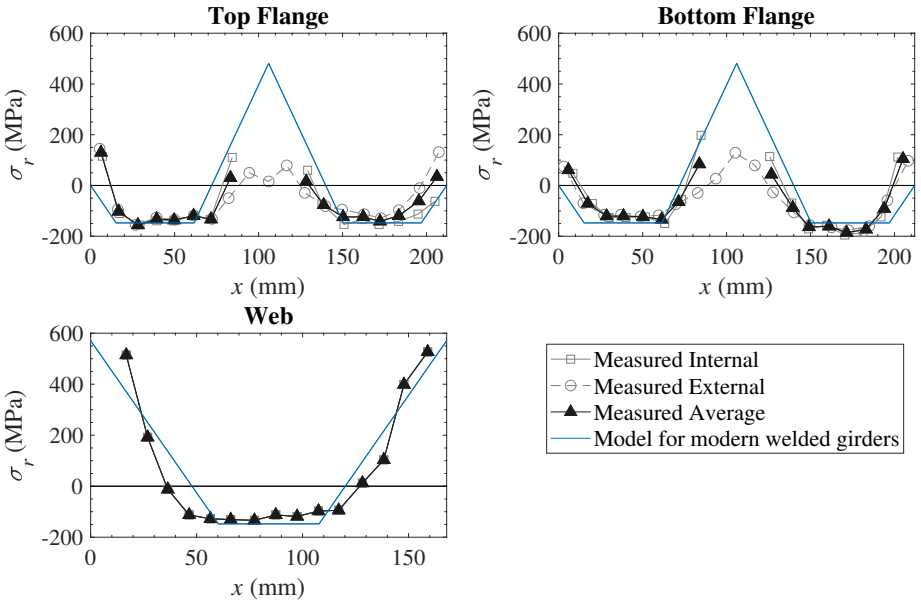

Figure 5.30: Comparison of proposed model ($B = 90$) with measured residual stress distribution for specimen H3-18 (Yang et al. 2018)

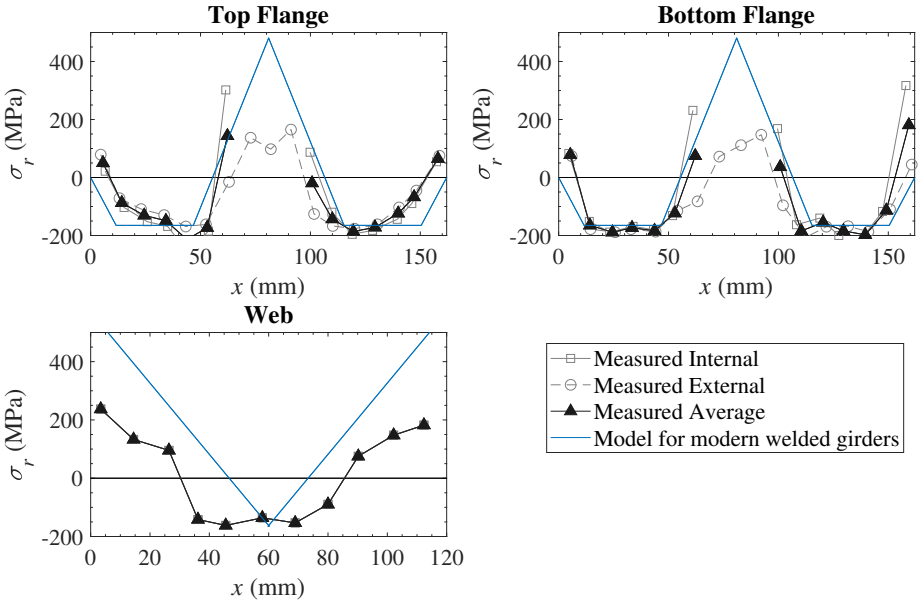

Figure 5.31: Comparison of proposed model ($B = 90$) with measured residual stress distribution for specimen H4-18 (Yang et al. 2018)

Chapter 6

Conclusions and Recommendations

6.1 Conclusions

Residual stress measurements on four reduced-scale welded steel girders were carried out using both the destructive sectioning method and a non-destructive ultrasonic method. Results from the sectioning tests were used to determine whether existing residual stress models accurately represent modern North American welded girders. The following conclusions were made:

- The Chernenko and Kennedy (1991) and Best-fit Prawel (Kim 2010) models both significantly over-predict compressive stress magnitude in the flanges: over-predictions of up to 167% and 69%, respectively, were observed.
- The BSK (2003) and Dwight and Moxham (1969) models over-predict compressive stress magnitude in the flanges, with larger over-predictions observed for narrower flanges. Maximum over-predictions among the tested specimens were 117% and 121% for each model, respectively.

Over-predictions of flange compressive stress are significant because the flange compressive stress has the greatest impact on lateral–torsional buckling (LTB) capacity. These models, therefore, likely under-predict LTB capacity when used in finite-element models. For this reason, a residual stress model is proposed for modern, welded girders, based on that proposed by Dwight and Moxham (1969) with the following modifications that draw from the new data from the current research:

- A triangular tensile distribution is used around the weld region instead of a rectangular one to better approximate the measured distributions near the weld.
- Compressive stresses in the flanges and web are equal and are calculated using equilibrium of the entire section (the original model considers equilibrium of the individual plates).
- Edge regions are introduced in the flanges to account for the effects of heat-cutting of the plate.
- An empirical reduction factor for flange width is applied to the width of the high-stress-gradient (HSG) region around the weld in the flange to capture the tensile zone accurately over a range of flange widths. A value for the empirical coefficient, B, of 53 is recommended.

Comparing the model to other residual stress data from welded I-sections in the literature led to the following additional recommendations:

- The model should only be applied to sections with flanges at least 25 mm thick.
- A B value of 90 is preferred over 53 for use in the reduction factor equation for the HSG region width in the flanges. A value of 90 improves accuracy for the specimens from the literature significantly while only minimally changing

predictions for those in the current research. This value may be refined as additional data become available.

It was also observed that measured residual stresses at the edges of the flanges are much lower than values typically reported in the literature. This may be partly due to the use of 30 mm wide strips over the entire width of the flange, which may not provide sufficient resolution to capture the peak stress at the edges of the flanges. Nevertheless, if higher stresses are present at the edge, they would exist only over a very narrow band.

The following conclusions were drawn from the ultrasonic measurement program:

- Sensitivity of wave velocity to stress (i.e., the acoustoelastic constant) for Grade 350W steel is lower than that observed in the literature for similar materials, and is observed to decrease with plate thickness.
- Zero-stress time-of-flight (TOF) values from the pre-heat-treatment stress calibration tests are more consistent than those from the post-heat-treatment tests among calibration samples due to difficulties in quantifying the effects of the removal of mill scale for the post-heat-treatment tests.
- TOF measurements in steel are sensitive to temperature: the relationship is linear between 23 °C and 30 °C and has a slope of 24 ns/°C. Based on TOF–stress calibration test results, this corresponds to slopes of 73 MPa/°C to 112 MPa/°C, depending on plate thickness. When measuring stress, temperature readings must be taken and used to correct TOF readings.
- A large degree of scatter is observed for ultrasonic stress measurements on the test girders. This is thought to be due in part to variation of the thickness of the couplant layer when the probe is bonded to the specimen and significant slippage of the acrylic wedges occurs within the housing, as evidenced by large

changes in TOF measurements taken on a reference sample before and after each measurement session. Surface texture may also contribute to scatter.

- Tensile stress peaks around the weld region are detected in the flanges and web for the majority of the test girders; however, measured stress magnitudes for the peaks consistently exceed the yield stress.
- Precise measurement of compressive stresses is not possible, as expected stress magnitudes are smaller than that of the scatter observed in the data.

6.2 Recommendations for Future Research

A predictive model for residual stresses in welded girders was proposed in this study. In order to refine the model further, the following items are recommended for further study:

- Investigate further the relationship between compressive stresses in the flanges and web. Parametric compressive stress was observed to be larger in the flanges in the plasma-cut specimens, but larger in the web in the flame-cut specimen.
- Further investigate residual stress distribution and magnitude at the edges of plasma- and flame-cut flanges, using strips narrower than 30 mm.
- Compare predictions of parametric compressive stress and HSG region width for a wider range of flange widths—particularly narrower flanges—in order to refine the B coefficient in the HSG region width reduction factor.

Measurement of residual stresses using ultrasound was investigated. Further work is required to improve system accuracy and precision—the following recommendations for future work are made:

- Additional measures should be taken to minimize relative movement of the transducers and wedges. This will help to reduce errors due to slippage of the acrylic wedges within the housing.

- Variability in TOF–stress curves should be examined. The large variability in zero-stress TOF between samples is of particular interest, as this implies velocity variation among samples equal to or greater than that caused by residual stresses. The decrease in acoustoelastic constant with plate thickness should also be examined.

- Effects of mill scale removal on TOF–stress curves should be examined further to determine if a consistent effect on TOF–stress curves is present.

Bibliography

Ballio, G. (1983). *Theory and design of steel structures*. Chapman and Hall, London.

Ban, H., Shi, G., Bai, Y., Shi, Y., and Wang, Y. (2013). "Residual stress of 460 MPa high strength steel welded I-section: experimental investigation and modeling". *International Journal of Steel Structures*, 13 (4), 691–705.

Belahcene, F. and Lu, J. (2002). "Determination of residual stress using critically refracted longitudinal waves and immersion mode". *Journal of Strain Analysis for Engineering Design*, 37 (1), 13–20.

Bray, D. E. and Tang, W. (2001). "Subsurface stress evaluation in steel plates and bars using the LCR ultrasonic wave". *Nuclear Engineering and Design*, 207 (2), 231–240.

BSK 99 (2003). *Swedish Regulations for Steel Structures*. Boverket, Karlskrona, Sweden.

Chernenko, D. E. and Kennedy, D. J. L. (1991). "An analysis of the performance of welded wide flange columns". *Canadian Journal of Civil Engineering*, 18 (4), 537–555.

Crecraft, D. I. (1967). "The measurement of applied and residual stresses in metals using ultrasonic waves". *Journal of Sound and Vibration*, 5 (1), 173–192.

CSA (2009). *CAN/CSA-S16-09: Limit States Design of Steel Structures*. Canadian Standards Association, Mississauga, Ontario.

CSA (2014). *CAN/CSA-S16-14: Limit States Design of Steel Structures*. Canadian Standards Association, Mississauga, Ontario.

Dux, P. F. and Kitipornchai, S. (1983). "Inelastic beam buckling experiments". *Journal of Constructional Steel Research*, 3 (1), 3–9.

Dwight, J. B. and Moxham, K. E. (1969). "Welded steel plates in compression". *The Structural Engineer*, 47 (2), 49–66.

Egle, D. M. and Bray, D. E. (1976). "Measurement of acoustoelastic and third-order elastic constants for rail steel". *The Journal of the Acoustical Society of America*, 60 (3), 741–744.

Essa, H. S. and Kennedy, D. J. L. (2000). "Proposed provision for the design of steel beam-columns". *Canadian Journal of Civil Engineering*, 27, 610–619.

Fitzpatrick, M. E., Fry, A. T., Holdway, P., Kandil, F. A., Shackleton, J., and Suominen, L. (2006). *Determination of residual stresses by x-ray diffraction*. Tech. rep. 2. National Physical Laboratory.

Fraga, R. S., Santos, A. A., and Andrino, M. H. (2009). "Temperature effect on the measurement of stresses in pipelines using ultrasonic LCR waves". *International Mechanical Engineering Congress and Exposition*, 361–367.

Fukumoto, Y. and Itoh, Y. (1981). "Statistical study of experiments on welded beams". *Journal of the Structural Division, ASCE*, 107 (ST1), 89–103.

Fukumoto, Y., Yoshito, I., and Kubo, M. (1980). "Strength variation of laterally unsupported beams". *Journal of the Structural Division, ASCE*, 109 (ST1), 541–562.

Galambos, T. V. (1963). "Inelastic lateral buckling of beams". *Journal of the Structural Division*, 89 (5), 217–244.

Galambos, T. V. and Ketter, R. L. (1959). "Columns under combined bending and thrust". *Journal of the Engineering Mechanics Division*, 85 (EM2), 135–152.

Greiner, R. and Kaim, P. (2001). *Comparison of LT-buckling design curves with test results*. TC 8 Report 23. European Convention for Constructional Steelwork, Brussels, Belgium.

Hughes, D. and Kelly, J. L. (1953). "Second-order elastic deformation of solids". *Physical Review*, 92 (5), 1145–1149.

Javadi, Y., Azari, K., Ghalehbandi, S. M., and Roy, M. J. (2017). "Comparison between using longitudinal and shear waves in ultrasonic stress measurement to investigate the effect of post-Weld Heat-Treatment on welding residual stresses". *Research in Nondestructive Evaluation*, 28 (2), 101–122.

Javadi, Y., Najafabadi, M. A., and Akhlaghi, M. (2012). "Residual stress evaluation in dissimilar welded joints using finite element simulation and the LCR ultrasonic wave". *Russian Journal of Nondestructive Testing*, 48 (9), 541–552.

Ji, X. L. (2019). "Large-scale lateral–torsional buckling tests of welded girders". MA thesis. University of Alberta.

Kabir, I. and Bhowmick, A. K. (2018). "Lateral torsional buckling of welded wide flange beams". *Canadian Journal of Civil Engineering*, 45 (9), 766–779.

Kalakoutsky, N. (1889). "The study of internal stresses in cast iron and steel".

Kamtekar, A. G. (1974). *An experimental study of welding residual stresses*. Tech. rep. Cambridge University.

Kim, Y. D. (2010). "Behavior and design of metal building frames using general prismatic and web-tapered steel I-section members". PhD thesis. Georgia Institute of Technology.

Luxion, W. W. and Johnston, B. G. (1948). "Plastic behavior of wide-flange beams". *Welding Journal*, 27 (63), 538–554.

MacPhedran, I. and Grondin, G. Y. (2011). "A simple steel beam design curve". *Canadian Journal of Civil Engineering*, 38, 141–153.

Masubuchi, K. (1980). *Analysis of Welded Structures*. Pergamon Press, Oxford.

Murnaghan, F. D. (1937). "Finite deformations of an elastic solid". *American Journal of Mathematics*, 59 (2), 235–260.

Nethercot, D. A. (1974). "Residual stresses and their influence upon the lateral buckling of rolled steel beams". *The Structural Engineer*, 52 (3), 89–96.

Olympus NDT (2011). *Ultrasonic transducers technical notes*.

Pekoz, T., Bjorhovde, R., Errera, S. J., Johnston, B. G., Sherman, D. R., and Tall, L. (1981). "Determination of residual stresses in structural shapes". *Experimental Techniques*, 5 (3), 4–7.

Pereira, P., Grijalba, F. A. F., and Santos, A. A. (2016). "A comparison of the use of critically refracted longitudinal waves and magnetic barkhausen noise for stress measurement in API 5L X70 steel". *Journal of Strain Analysis for Engineering Design*, 51 (8), 563–571.

Prawel, S. P., Morrell, M. L., and Lee, G. C. (1974). "Bending and buckling strength of tapered structural members". *Welding Research Supplement*, 53, 75–84.

Prime, M. B. and Gonzales, A. R. (2000). "The contour method: simple 2-D mapping of residual stresses". *Sixth International Conference on Residual Stresses*, 617–624.

Rez-Gala, C. (1962). "Residual stresses in rolled I-sections". *Proceedings of the Institution of Civil Engineers*, 23 (3), 361–378.

Richter, J. F. (1998). "Flexural capacity of slender web plate girders (Masters thesis)". PhD thesis. The University of Texas at Austin.

Rossini, N. S., Dassisti, M., Benyounis, K. Y., and Olabi, A. G. (2012). "Methods of measuring residual stresses in components". *Materials and Design*, 35, 572–588.

Sadeghi, S., Najafabadi, M. A., Javadi, Y., and Mohammadisefat, M. (2013). "Using ultrasonic waves and finite element method to evaluate through-thickness residual stresses distribution in the friction stir welding of aluminum plates". *Materials and Design*, 52, 870–880.

Santos, A. A., Bray, D. E., and Caetano, S. F. (2004). "Evaluation of the rolling direction effect in the acoustoelastic properties for API 5L X70 steel used in pipelines". *Recent Advances in Nondestructive Evaluation Techniques for Material Science and Industries*. Vol. 484. ASME, 85–90.

Sherman, D. R. (1969). "Residual stress measurement in tubular members". *Journal of the Structural Division, ASCE*, 4, 635–647.

Subramanian, L. and White, D. W. (2017). "Resolving the disconnects between lateral torsional buckling experimental tests, test simulations and design strength equations". *Journal of Constructional Steel Research*, 128, 321–334.

Tebedge, N., Alpsten, G., and Tall, L. (1973). "Residual-stress measurement by the sectioning method". *Experimental Mechanics*, 13 (2), 88–96.

Wong-Chung, A. D. and Kitipornchai, S. (1987). "Partially braced inelastic beam buckling experiments". *Journal of Constructional Steel Research*, 7, 189–211.

Yang, B., Nie, S., Xiong, G., Hu, Y., Bai, J., Zhang, W., and Dai, G. (2016). "Residual stresses in welded I-shaped sections fabricated from Q460GJ structural steel plates". *Journal of Constructional Steel Research*, 122, 261–273.

Yang, B., Xiong, G., Nie, S., Elchalakani, M., and Zhu, Q. (2018). "Experimental and model investigation on residual stresses in Q460GJ thick-walled I-shaped sections". *Journal of Constructional Steel Research*, 145, 489–503.

Young, B. W. (1971). *Residual stresses in hot-rolled sections*. Tech. rep. University of Cambridge.

Yuan, H. X., Wang, Y. Q., Shi, Y. J., and Gardner, L. (2014). "Residual stress distributions in welded stainless steel sections". *Thin-Walled Structures*, 79, 38–51.

Appendix A

Test Specimen Dimensions and Weld Sequence

Testing program girder summary (see Ji (2019))

(Note: only SP2-1, SP2-2, SP3 and SP4 are tested in this study)

No.	Specimen ID	Total Qty	w (mm)	d (mm)	b (mm)	t_f (mm)	d/b
SP1	G6-470-32-2-p	1	12.7	600	470	31.8	1.28
SP2-1	G6-430-32-1-p	2	12.7	600	430	31.8	1.40
SP2-2	G6-430-32-1-f						
SP3	G6-300-32-1-p	1	12.7	600	300	31.8	2.00
SP4	G8-430-25-2-p	1	12.7	800	430	25.4	1.86
SP5	G8-390-32-2-p	1	12.7	800	390	31.8	2.05
SP6	G8-390-25-2-p	1	12.7	800	390	25.4	2.05
SP7-1	G9-360-32-3-p	2	9.53	900	360	31.8	2.50
SP7-2	G9-360-32-3-f						
SP8	G9-360-25-3-f	1	9.53	900	360	25.4	2.50
SP9	G9-430-25-3-f	1	9.53	900	430	25.4	2.09

Girder cross-section dimensions

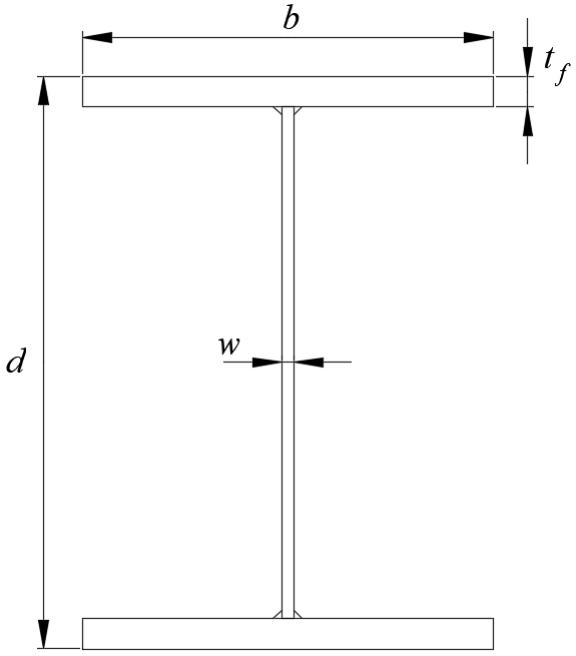

Weld sequences for tested girders

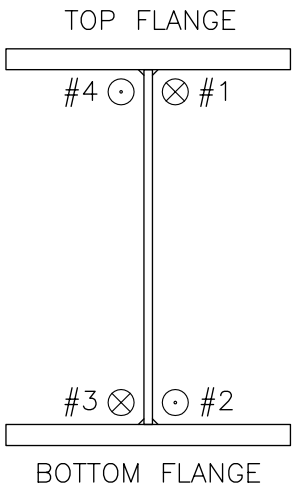

SPECIMEN:	SP2−1A

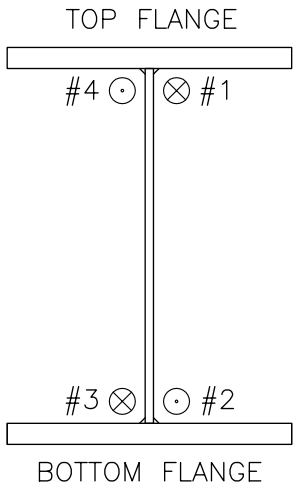

SPECIMEN:	SP2−2A

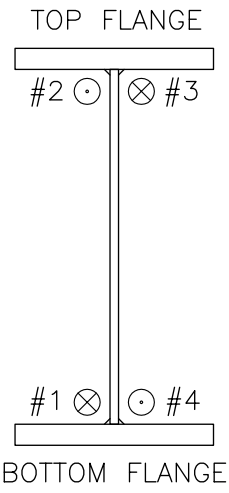

SPECIMEN:	SP3A

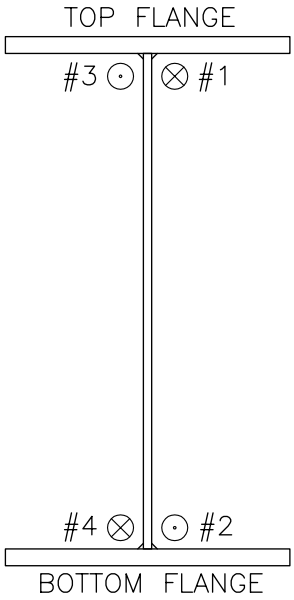

SPECIMEN:	SP4A

Appendix B

Residual Stress Data and Models

Properties of specimens examined from the literature

Note: all specimens listed comprise flame-cut plates

Study	No.	b (mm)	t (mm)	h (mm)	w (mm)	a (mm)	σ_{yf} (MPa)	σ_{yw} (MPa)	E_f (GPa)	E_w (GPa)
Ban et al. (2013)	R11-460	130	10	90	10	6	532	532	210	210
	R12-460	150	10	130	10	6	532	532	210	210
	R13-460	210	14	182	14	6	492	492	210	210
	R14-460	290	10	130	10	6	532	532	210	210
Yang et al. (2016)	H1-16	180	10	270	8	6	499	539	211	212
	H2-16	180	10	360	8	6	499	539	211	212
	H3-16	180	10	450	8	6	499	539	211	212
	H7-16	200	10	420	10	8	499	499	211	212
	H8-16	250	16	432	10	8	519	499	211	212
Yang et al. (2018)	H1-18	312	25	264	12	10	481	571	211	212
	H2-18	262	25	216	12	10	481	571	211	212
	H3-18	212	25	168	12	10	481	571	211	212
	H4-18	162	25	120	12	10	481	571	211	212

Comparison of residual stress models with measured distributions

Chernenko and Kennedy Model

Specimen: SP2-1

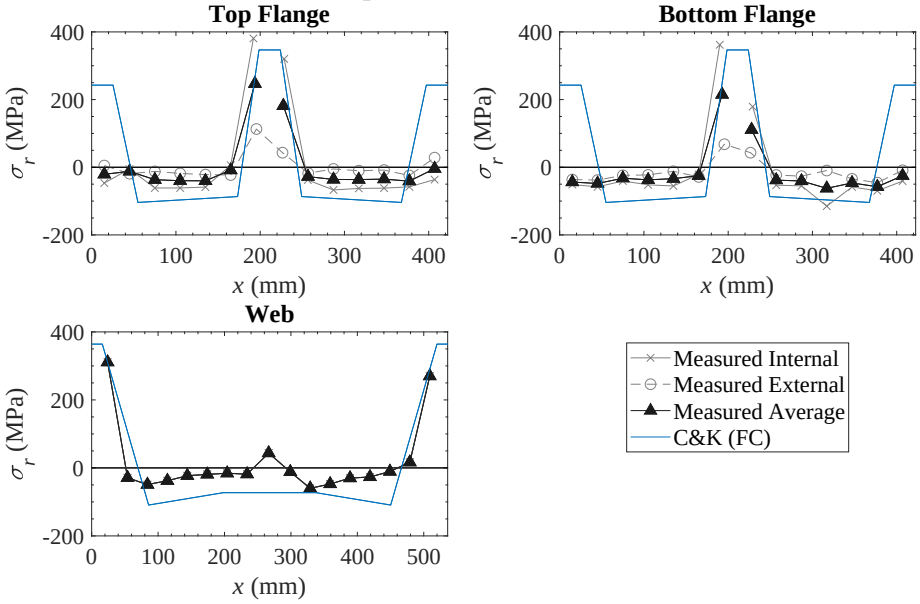

Specimen: SP2-2

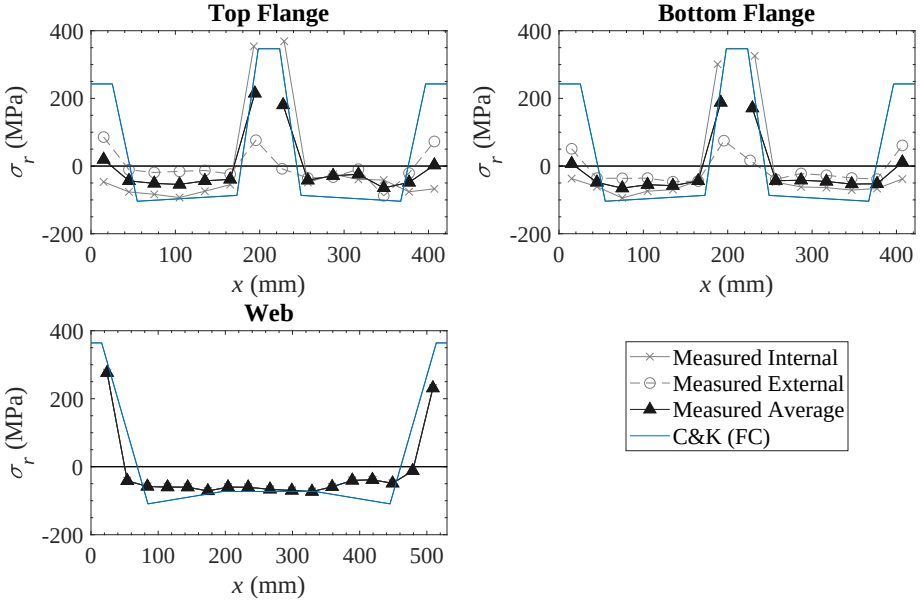

Specimen: SP3

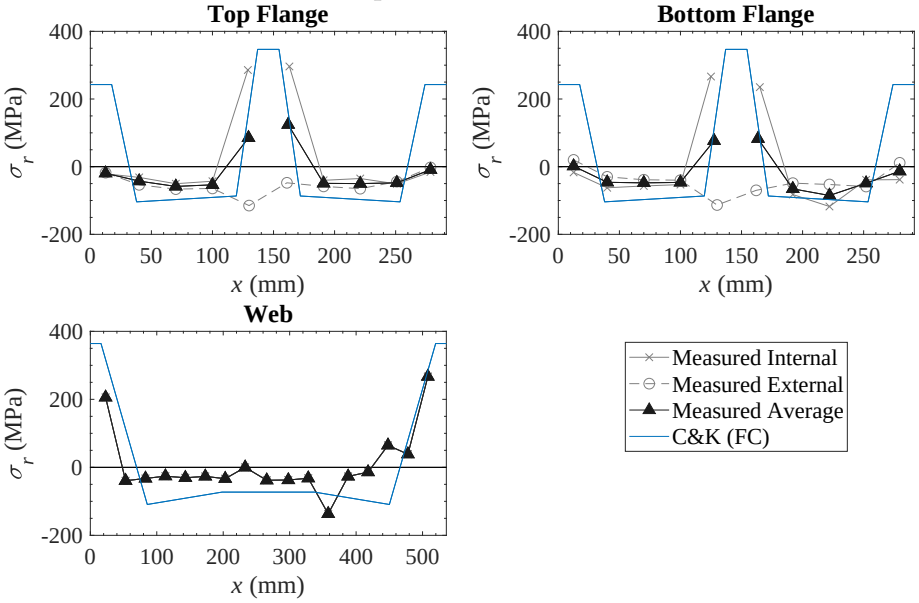

Specimen: SP4

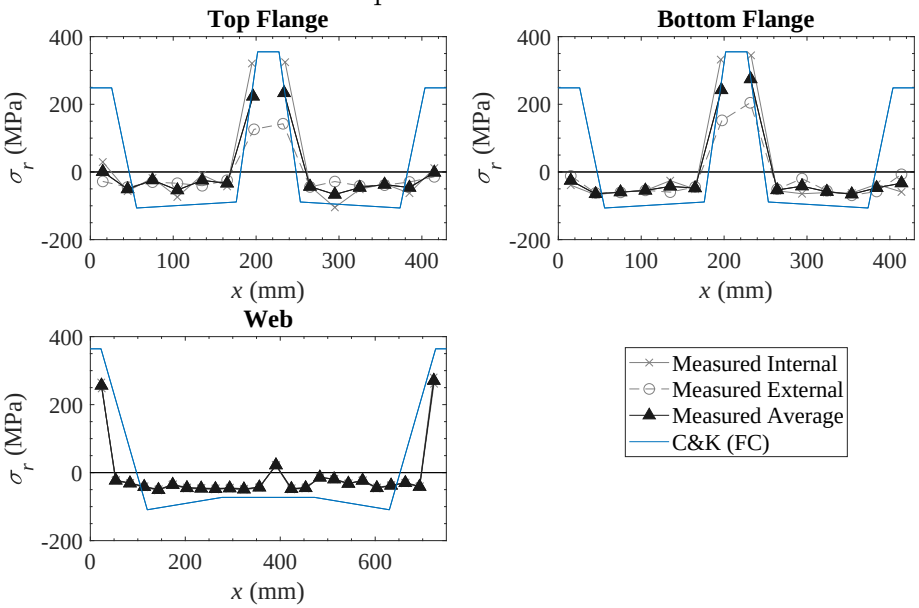

Specimen: SP2-1

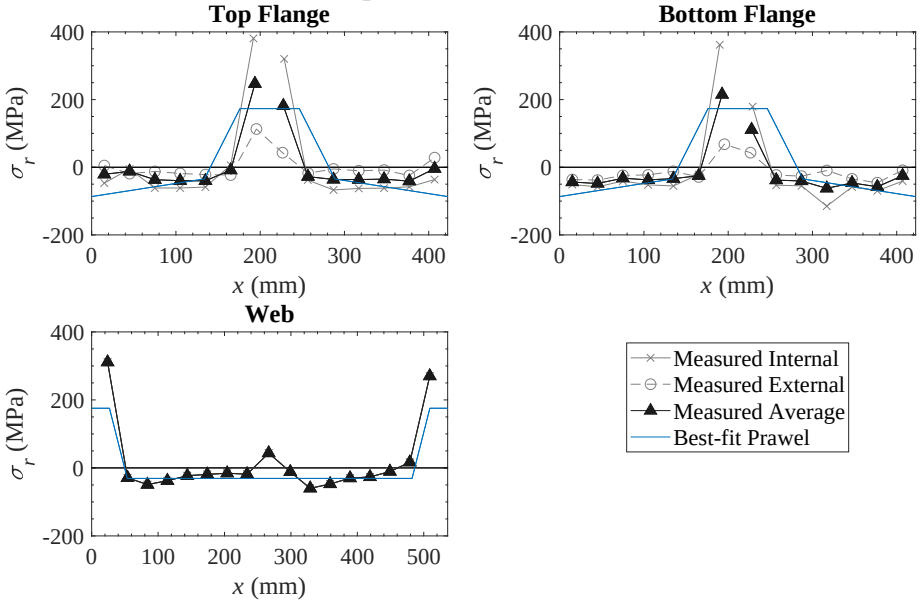

Specimen: SP2-2

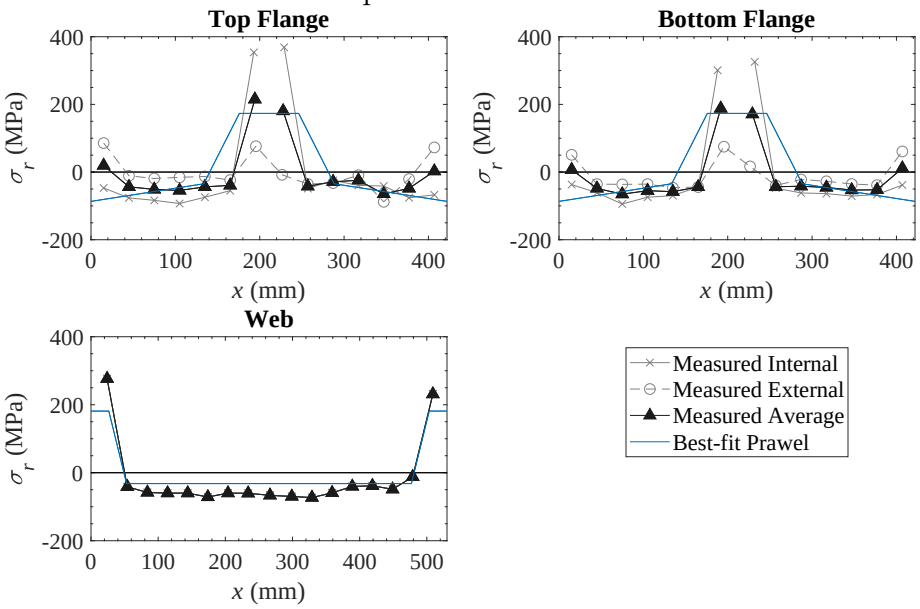

Specimen: SP3

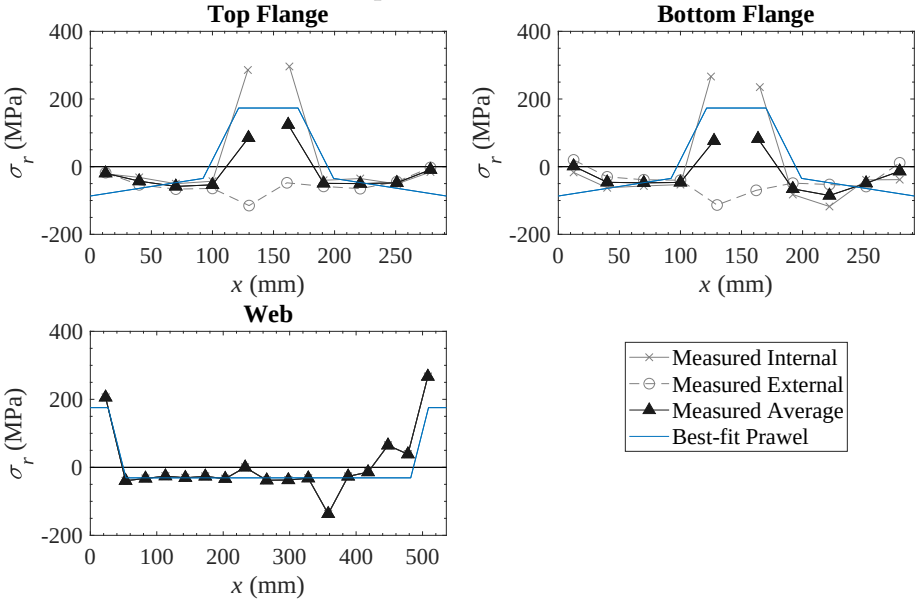

Specimen: SP4

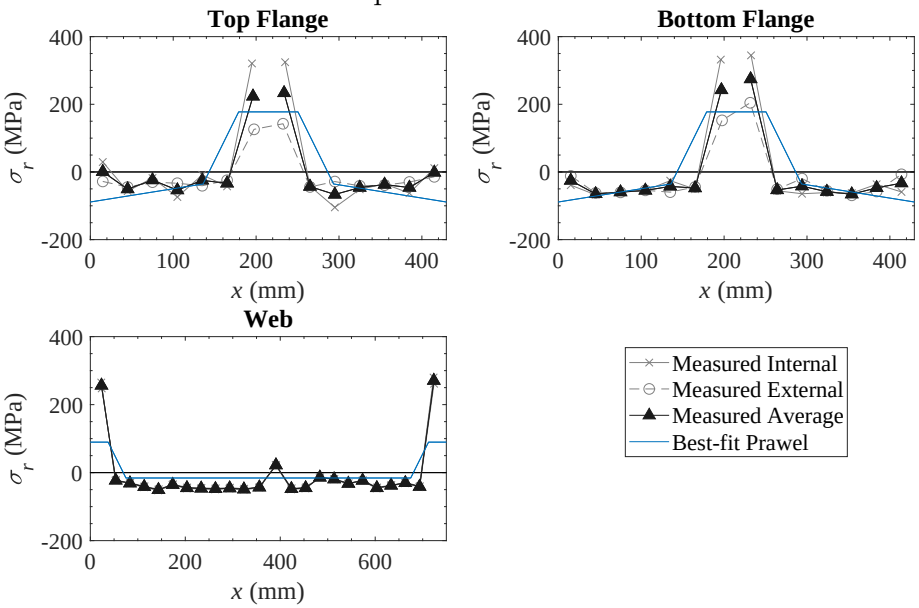

Specimen: SP2-1

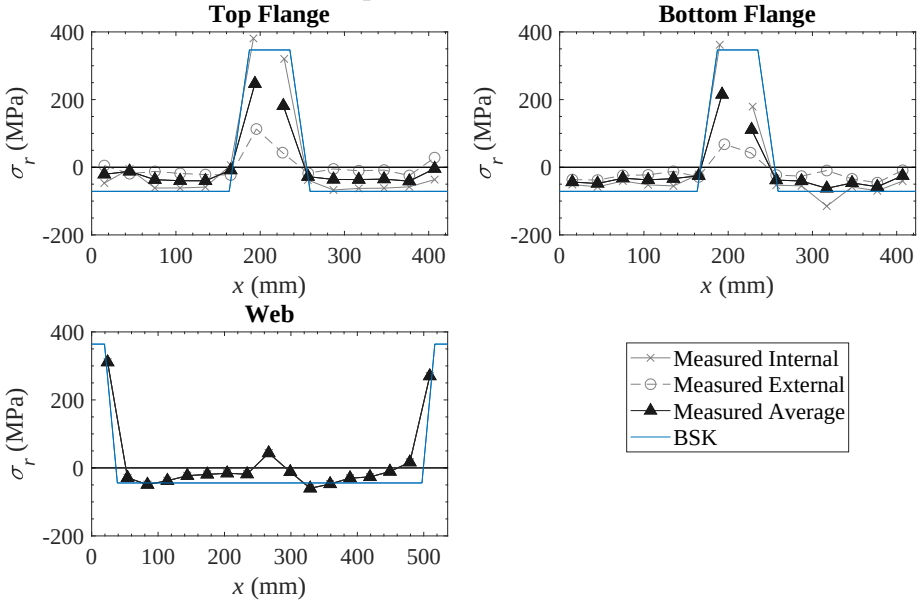

Specimen: SP2-2

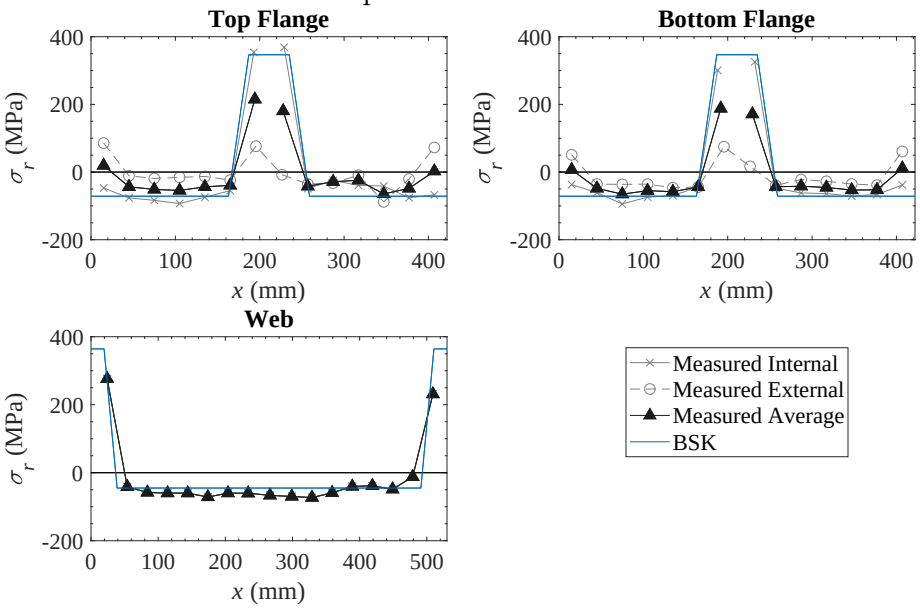

Specimen: SP3

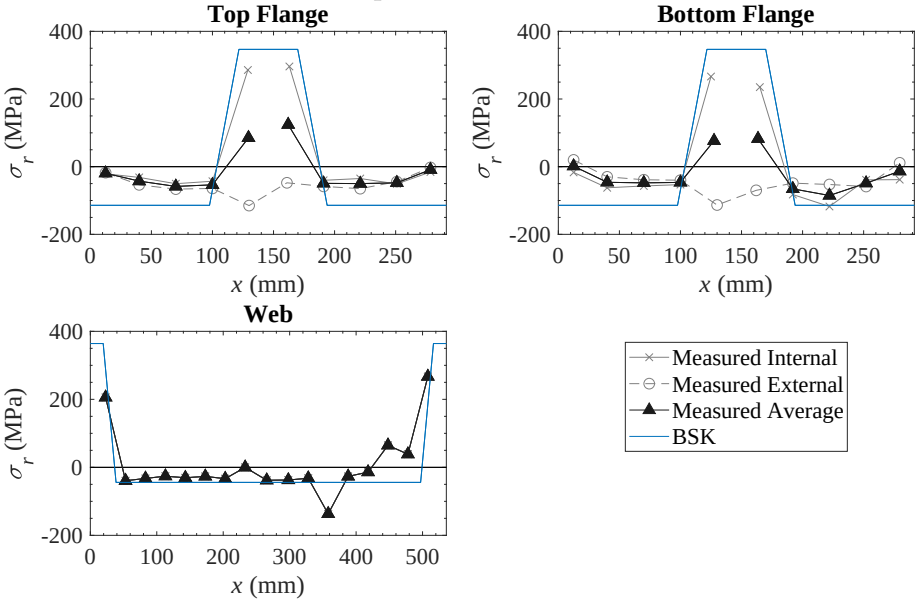

Specimen: SP4

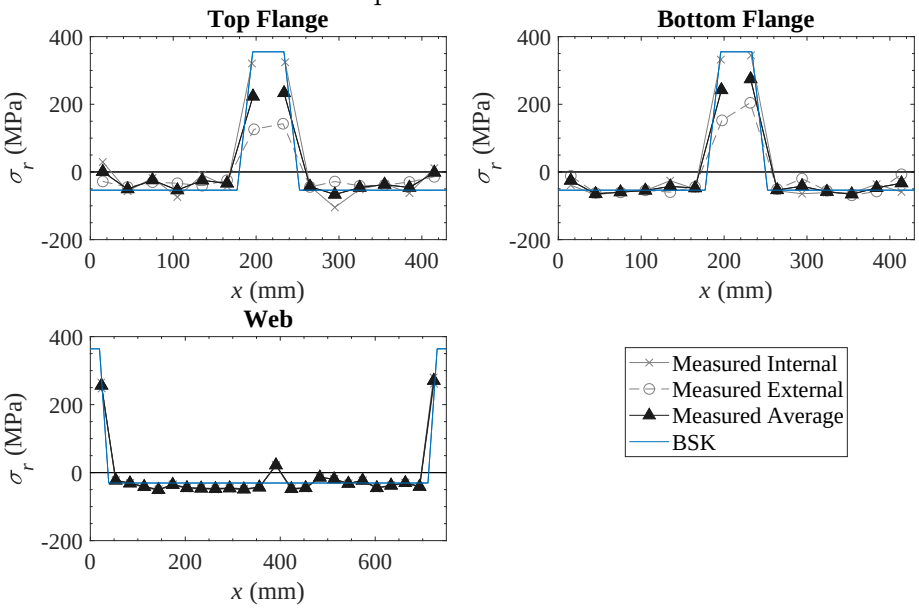

Specimen: SP2-1

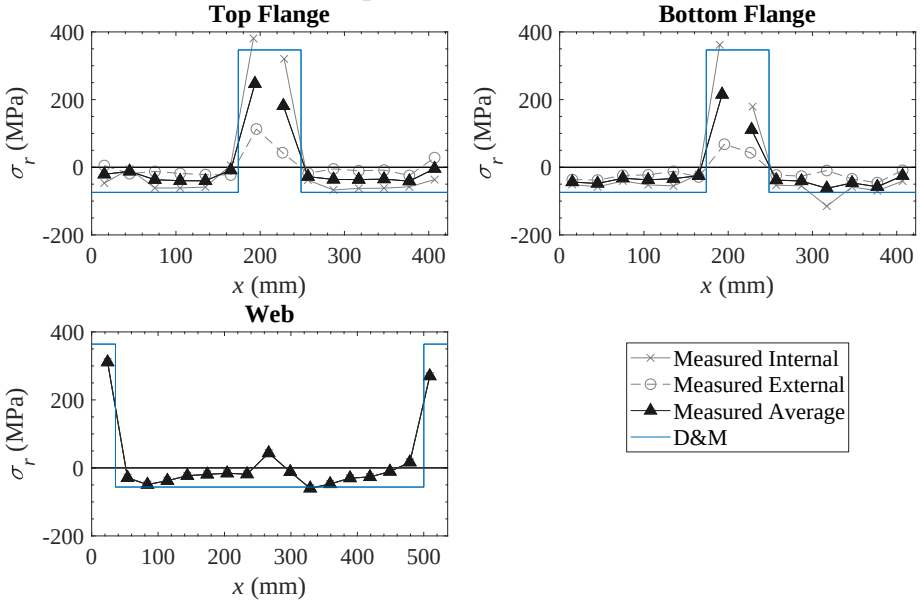

Specimen: SP2-2

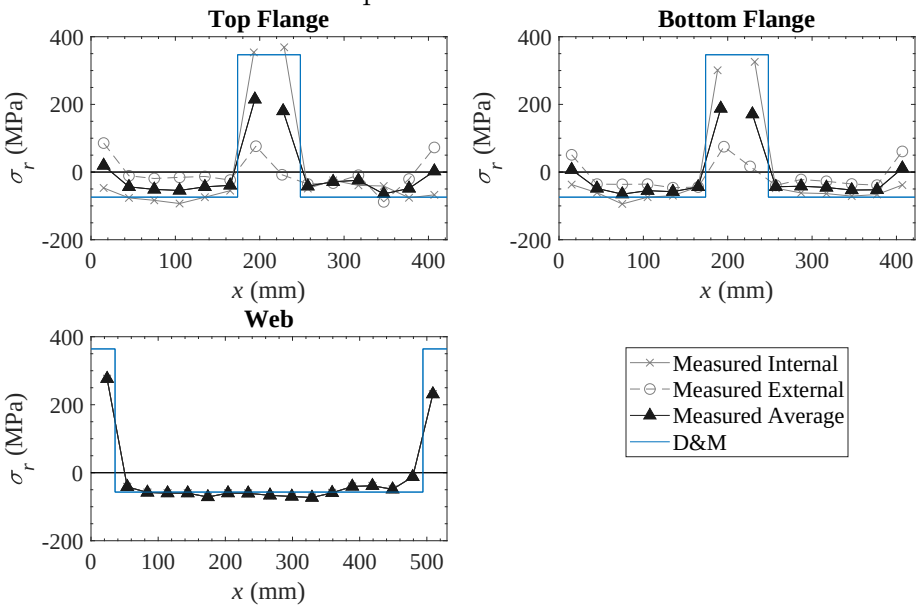

Specimen: SP3

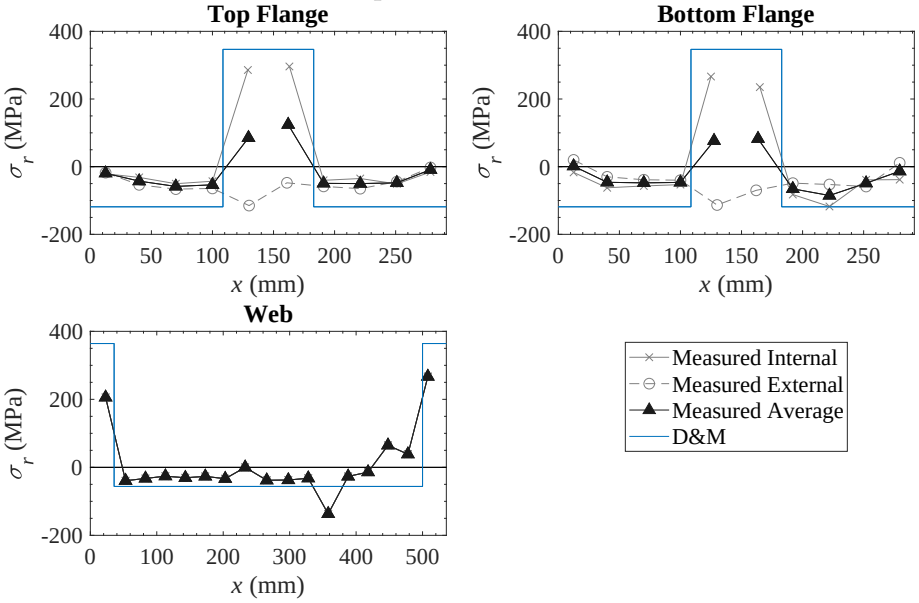

Specimen: SP4

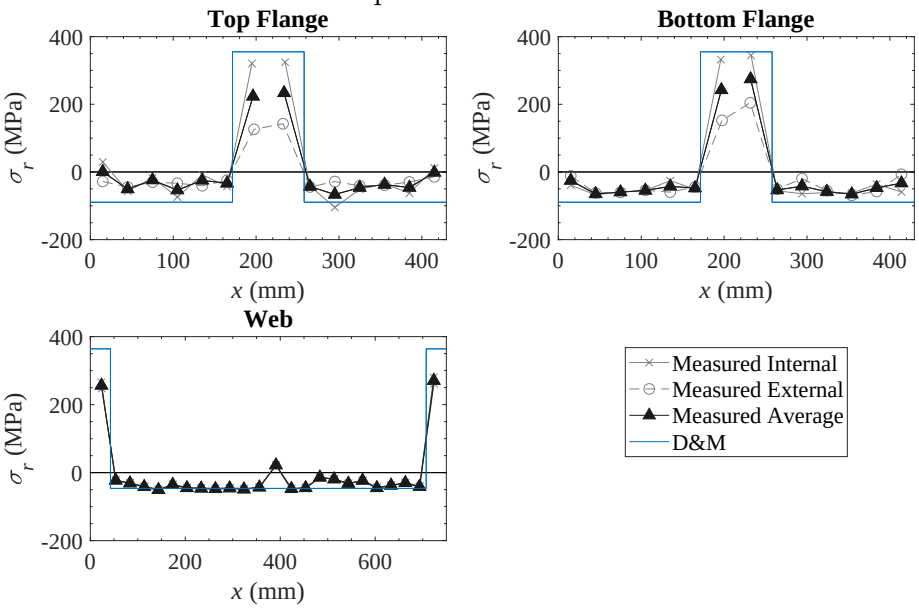

Specimen: SP2-1

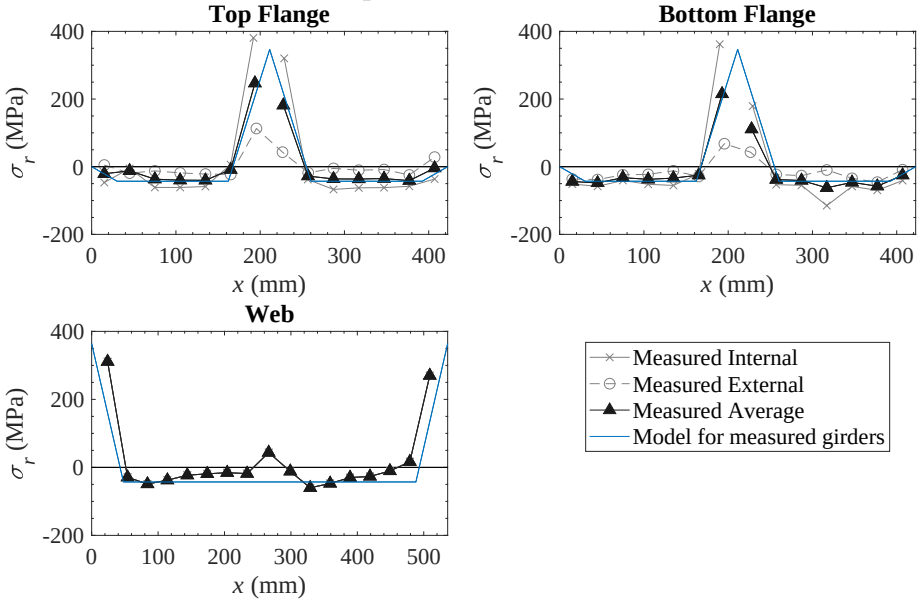

Specimen: SP2-2

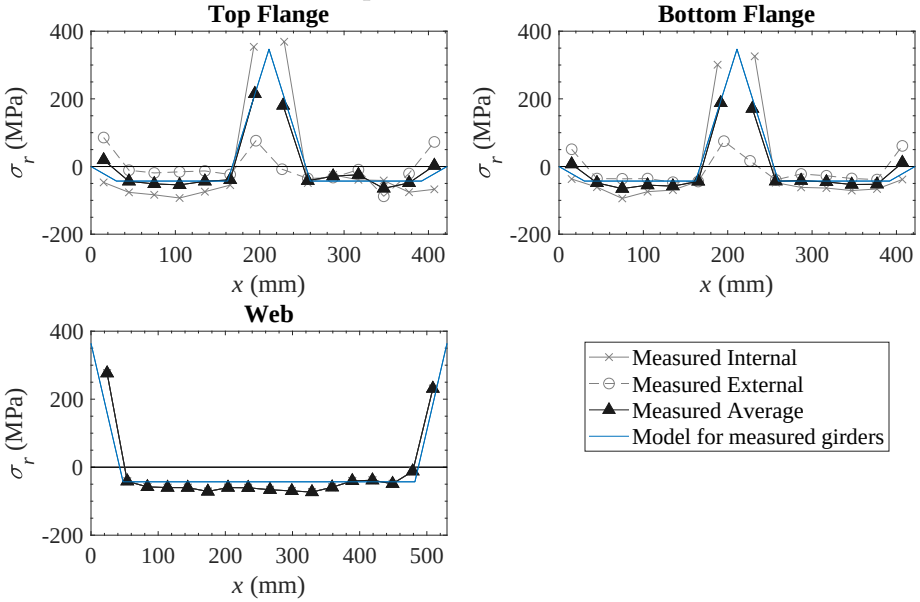

Specimen: SP3

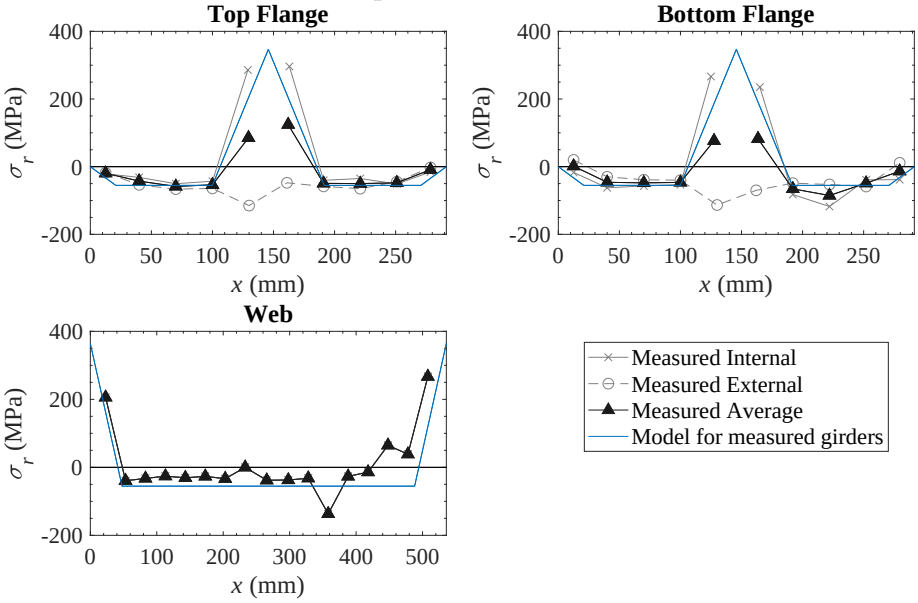

Specimen: SP4

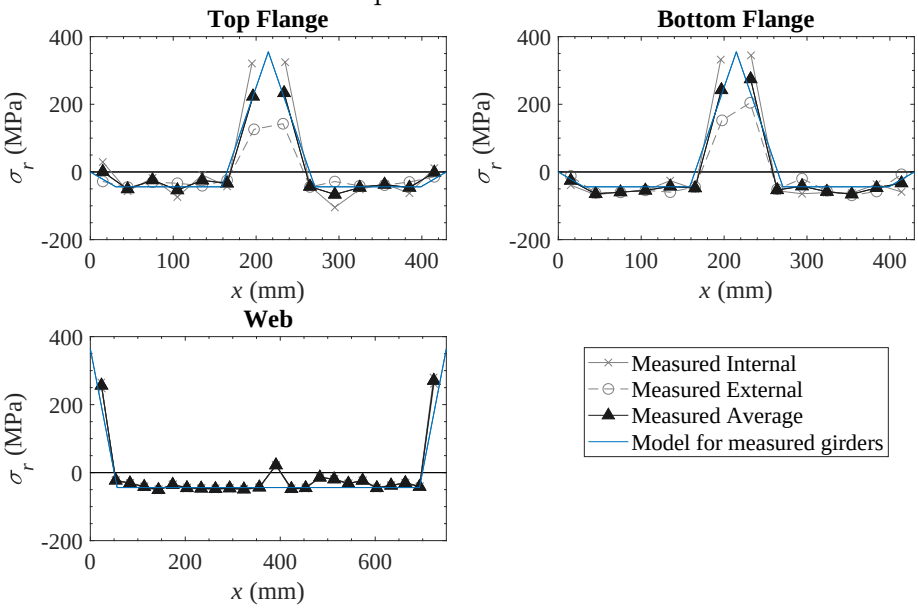

Appendix C

Ultrasonic Stress Calibration Test Plots

TEST ID:	UTC32-1 (PREHT)

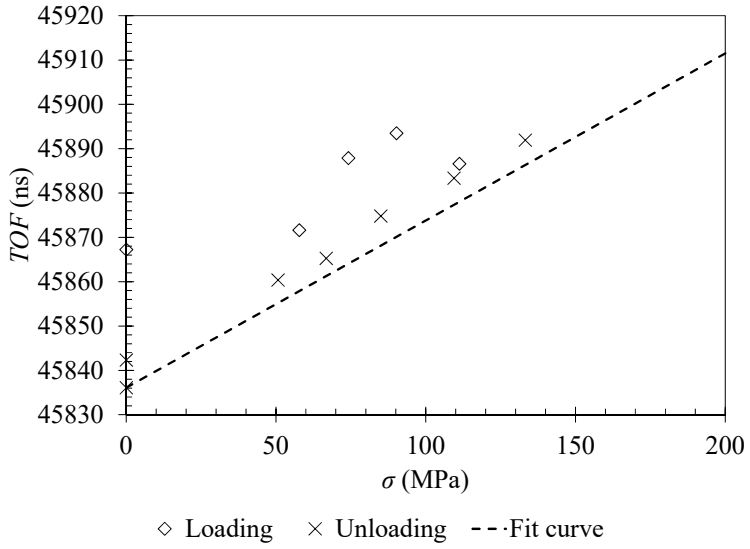

Specimen cross-section dimensions	
Width	102 mm
Thickness	32.0 mm
Area	3273 mm^2

Fit curve parameters	
$\Delta TOF/\Delta\sigma$	0.377 ns/MPa
TOF_0	45836 ns

TEST ID:	UTC32-1 (PREHT)

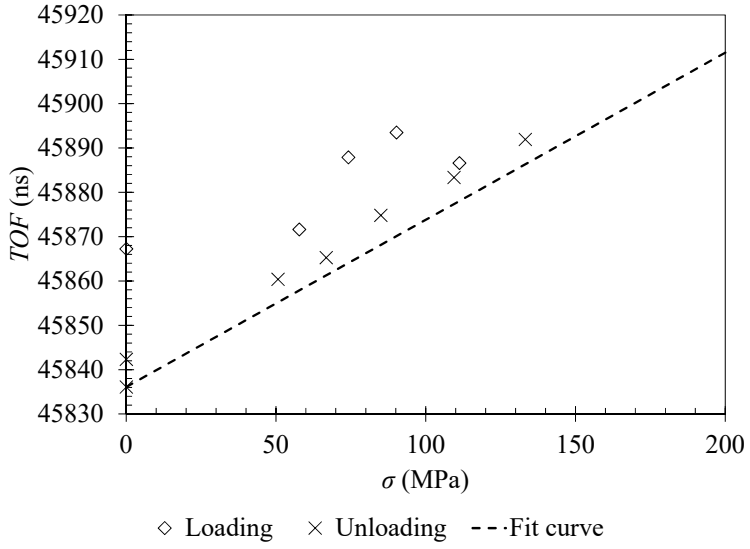

Specimen cross-section dimensions	
Width	102 mm
Thickness	32.0 mm
Area	3273 mm^2

Fit curve parameters	
$\Delta TOF/\Delta\sigma$	0.377 ns/MPa
TOF_0	45836 ns

TEST ID:	UTC25-1 (PREHT)

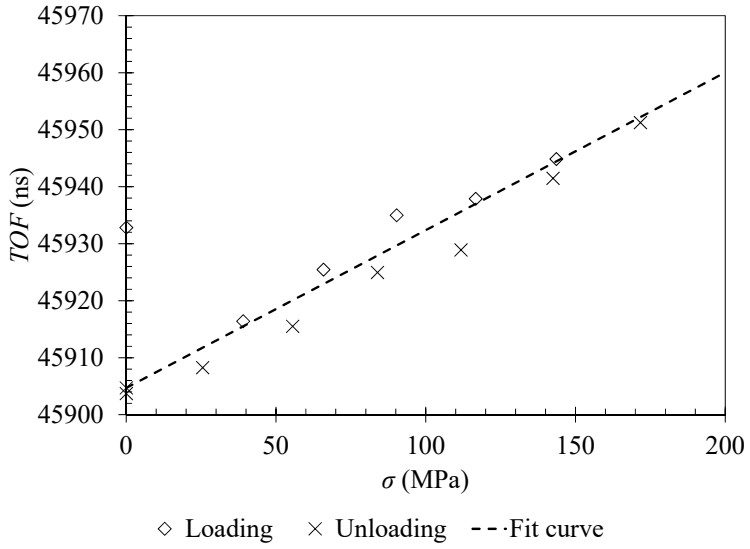

Specimen cross-section dimensions	
Width	102 mm
Thickness	25.2 mm
Area	2563 mm^2

Fit curve parameters	
$\Delta TOF/\Delta\sigma$	0.277 ns/MPa
TOF_0	45905 ns

TEST ID:	UTC25-2 (PREHT)

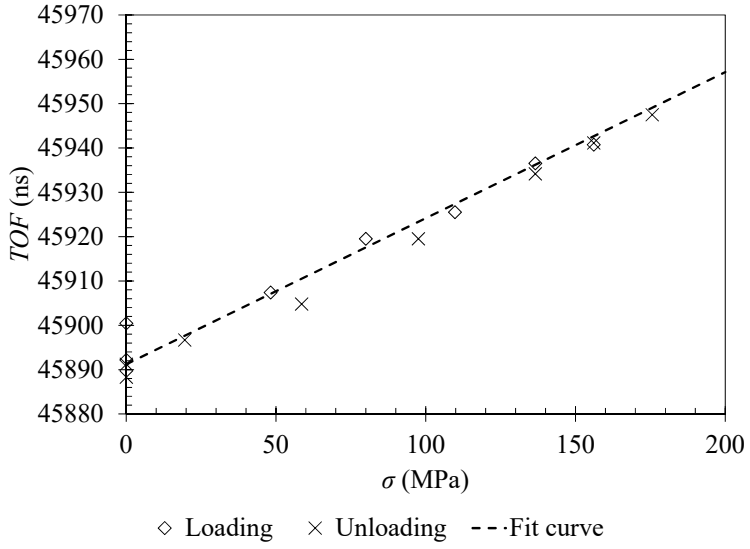

Specimen cross-section dimensions	
Width	102 mm
Thickness	25.2 mm
Area	2563 mm^2

Fit curve parameters	
$\Delta TOF/\Delta\sigma$	0.330 ns/MPa
TOF_0	45891 ns

TEST ID:	UTC13-1 (PREHT)

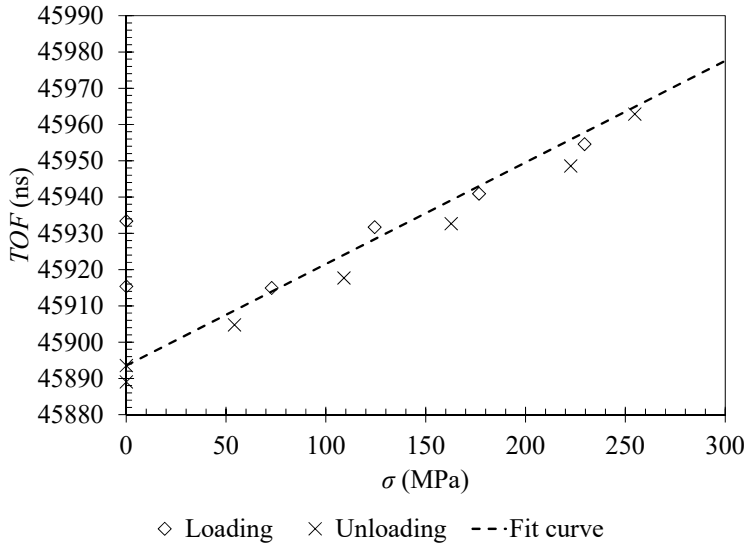

Specimen cross-section dimensions	
Width	102 mm
Thickness	13.0 mm
Area	1326 mm^2

Fit curve parameters	
$\Delta TOF/\Delta\sigma$	0.280 ns/MPa
TOF_0	45894 ns

TEST ID:	UTC13-2 (PREHT)

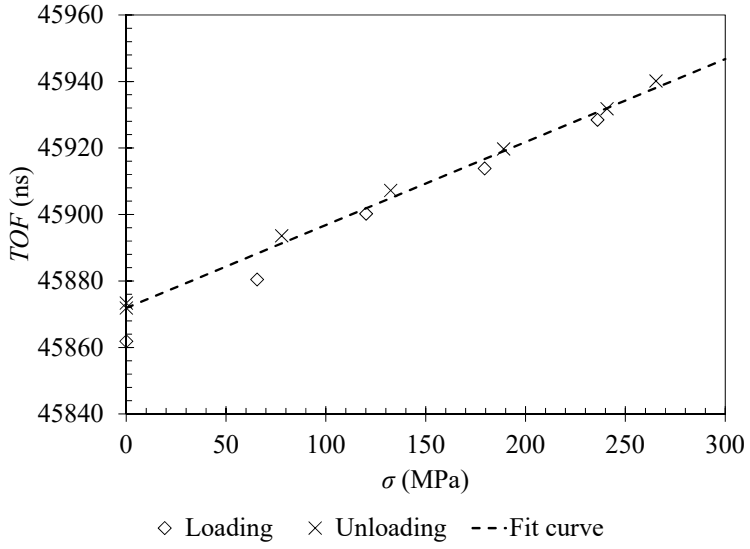

Specimen cross-section dimensions	
Width	102 mm
Thickness	13.0 mm
Area	1326 mm^2

Fit curve parameters	
$\Delta TOF/\Delta\sigma$	0.250 ns/MPa
TOF_0	45872 ns

TEST ID:	UTC10-1 (PREHT)

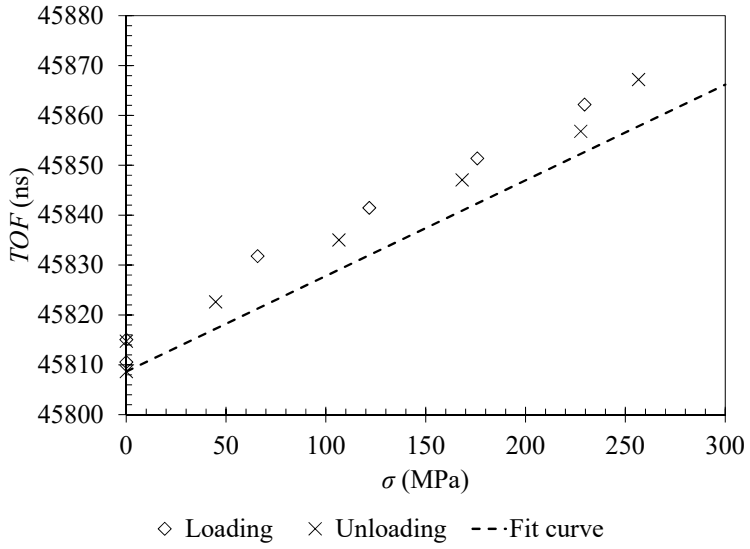

Specimen cross-section dimensions	
Width	102 mm
Thickness	10.1 mm
Area	1022 mm^2

Fit curve parameters	
$\Delta TOF/\Delta\sigma$	0.192 ns/MPa
TOF_0	45809 ns

TEST ID:	UTC10-2 (PREHT)

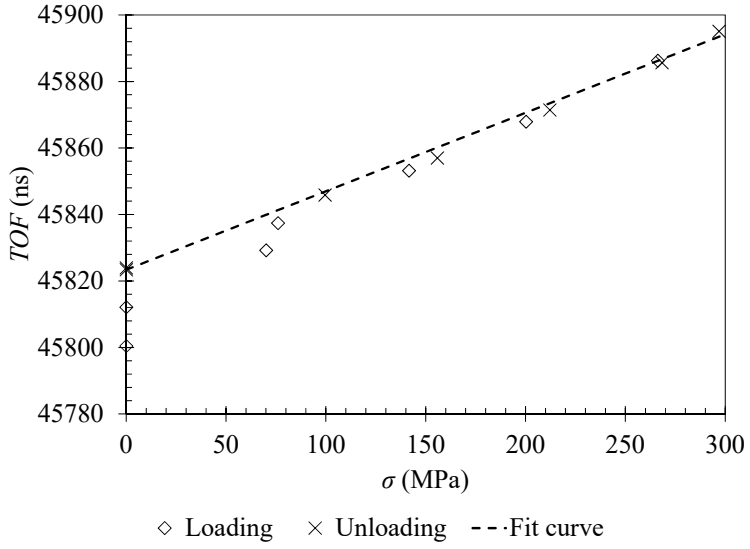

Specimen cross-section dimensions	
Width	102 mm
Thickness	10.1 mm
Area	1022 mm^2

Fit curve parameters	
$\Delta TOF/\Delta\sigma$	0.236 ns/MPa
TOF_0	45823 ns

TEST ID:	UTC32 (POSTHT)

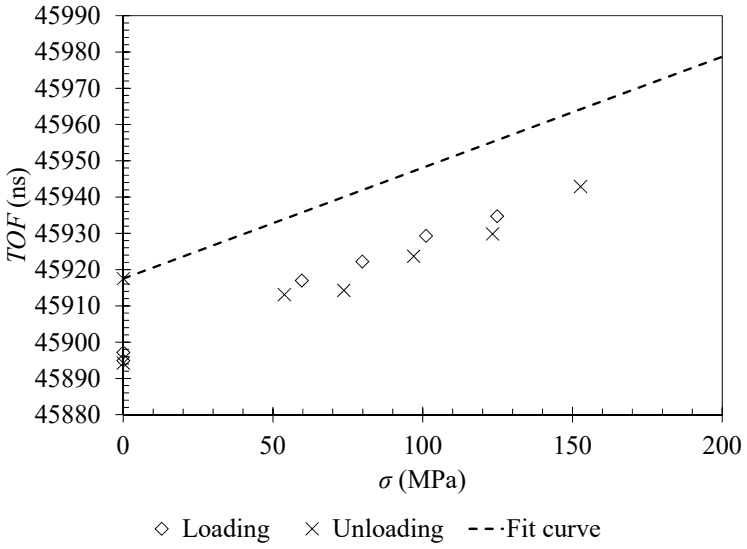

Specimen cross-section dimensions	
Width	102 mm
Thickness	32.0 mm
Area	3273 mm^2

Fit curve parameters	
$\Delta TOF/\Delta\sigma$	0.306 ns/MPa
TOF_0	45917 ns

TEST ID:	UTC25 (POSTHT)

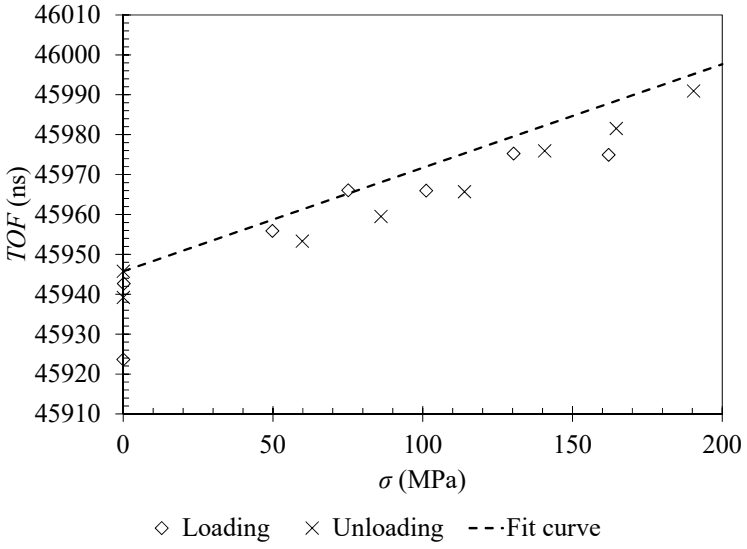

Specimen cross-section dimensions	
Width	102 mm
Thickness	25.2 mm
Area	2563 mm^2

Fit curve parameters	
$\Delta TOF/\Delta\sigma$	0.260 ns/MPa
TOF_0	45946 ns

TEST ID:	UTC13 (POSTHT)

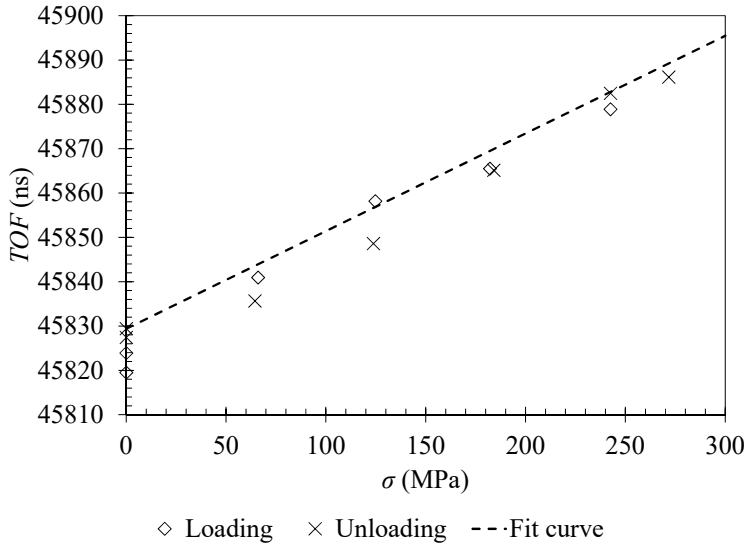

Specimen cross-section dimensions	
Width	102 mm
Thickness	13.0 mm
Area	1326 mm^2

Fit curve parameters	
$\Delta TOF/\Delta\sigma$	0.220 ns/MPa
TOF_0	45829 ns

TEST ID:	UTC10 (POSTHT)

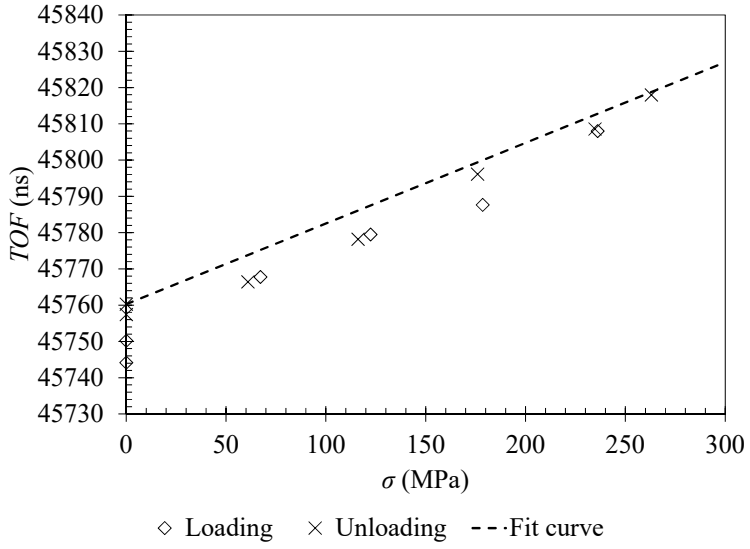

Specimen cross-section dimensions	
Width	102 mm
Thickness	10.1 mm
Area	1022 mm^2

Fit curve parameters	
$\Delta TOF/\Delta\sigma$	0.222 ns/MPa
TOF_0	45760 ns